METAL-ORGANIC FRAMEWORKS (MOFS) BASED NANO-MATERIALS IN THE APPLICATIONS AS SENSORS AND CATALYSTS

A Dissertation

by

JIALUO LI

Submitted to the Office of Graduate and Professional Studies of
Texas A&M University
in partial fulfillment of the requirements for the degree of

DOCTOR OF PHILOSOPHY

Chair of Committee,	Hong-Cai Zhou
Committee Members,	Xiaofeng Qian
	Matthew Sheldon
	Michael Nippe
Head of Department,	Simon W. North

December 2020

Major Subject: Chemistry

ABSTRACT

This work begins with an introduction into the development of MOFs, particularly nano-sized MOFs and MOFs based metal nano-particles. The reported synthetic strategies as well as their application in bio-related and catalyst field are discussed and perspectives on the promising future direction of this field are also presented.

First research demonstrates that “turn-on” fluorescent sensors can be assembled by combining a fluorophore and a recognition moiety within a complex cavity of a multicomponent MOF. The selective binding of CN^- to recognition moieties inhibited the energy transfer between the two moieties, resulting in a fluorescence “turn on” effect. The optimized MOF-sensor had a CN^- detection limit of 0.05 μM, which is much lower than traditional CN^- molecular fluorescent sensors (~0.2 μM).

Second research demonstrates that aggregation caused quenching of perylenes can be minimalized by molecular incorporation into metal-organic frameworks (MOFs). The average distance between perylene moieties was tuned by changing the linker ratios, thus controlling the fluorescence intensity, emission wavelength, and quantum yield. Taking advantage of the tunable fluorescence, inherent porosity, and high chemical stability of the parent MOF, utilization of the framework was able to be applied as a fluorescent sensor for oxygen detection in the gas phase. Ultimately, this work showed fast response times and good recyclability of the material.

Third research demonstrates that the utility of a coordination cage as a nanoparticle container to encapsulate ruthenium nanoparticles and tune their crystalline structures.

Using this method, a rare fcc crystalline structure was able to be formed. This nanoparticle-cage composite exhibited record-high catalytic activity toward ammonia borane dehydrogenation. In addition, it provided a strategy for the encapsulation of metal nanocrystals within a soluble molecular cage, forming homogeneous catalysts with unprecedented activity.

The main purpose of the works presented is to (1) explore the application of MOFs in the field of fluorescence sensors; (2) establish synthetic strategies for nano-sized MOFs; and (3) improve the catalytically performance of PCC supported metal nanoparticles. Building up on this work and the rapid development by others in this field, promising applications of MOFs in fluorescence sensors, bio-sensing, and clean energy generation are anticipated.

DEDICATION

This thesis is dedicated to Deliang Li and Jing Zhou.

ACKNOWLEDGEMENTS

First and foremost, I would like to thank you my committee chair, Prof. Hong-Cai Zhou for his guidance, encouragement and patience through my entire graduate study. He not only gave me precious suggestions on my research, but also provided me with a stage to be a leader in the group and to set a good example of being a professional researcher. I could not have imagined having a better advisor and mentor for my graduate study.

In addition to my supervisor, I would like to show my greatest gratitude to my committee members: Prof. Xiaofeng Qian, Prof. Matthew Sheldon, and Prof. Michael Nippe. I would like to thank them not only for their insightful suggestions and guidance, but also for the hard questions and critical analysis of my work which helped to incent me to widen my research view and form various perspectives about scientific though.

I am also grateful to my colleagues, friends, and the department faculty and staff for helping me out every time I encountered difficulties and making my time at Texas A&M University a great experience. They are Dr. Shuai Yuan, Dr. Sai Che, Dr. Xizhen Lian, Dr. Hao Li, Dr. Kecheng Wang, Dr. Jiandong Pang, Dr. Peng Zhang, Dr. Jingbo Liu, Dr. Zac Perry, Dr. Yingmu Zhang, Dr. Xinyu Yang, Dr. Yanyan Huang, Dr. Qi Wang, Dr. Stephen A Fordham, Dr. Yue Song, Xiaozhou Ji, Mei Dong, Haomiao Xie, Xuemei Yang, Yuchen Qiao, Jeremy Willman, Greg Day, Elizabeth Joseph, Christina Lollar, Mallory Smith, Sayan Benerjee, Melih Baci, Liang Feng, Hannah Drake, Angelo Kirchon, Zhifeng Xiao, Wenmiao Chen, Peiyu Cai, Tianhao Yan, Josh Powell, Kunyu Wang, Fan Chen,

Julie A Zecher, Dr. Soon-Mi Lim, Sandy Horton, Valerie McLaughlin, Dr. Simon North, Gregory Wylie, Howard Williams, and Vladimir Bakhmoutov.

I appreciate the help from my collaborators, including Prof. Kui Tan, Lan Huang, Prof. Tahir Cagin, and Prof. Wen-she Liu. Special acknowledgement goes to Prof. Wen-she Liu and his group. Their support on cell-related experiment was essential to my graduate research.

Last but not least, I would like to thank my parents for their love and selfless support throughout my life. Thank you both for giving me strength to pursue my dreams.

CONTRIBUTORS AND FUNDING SOURCES

Contributors

This work was supervised by a thesis committee consisting of Professor Hong-Cai Zhou (chair of committee), Professor Matthew Sheldon, and Professor Michael Nippe of the Department of Chemistry, and Professor Xiaofeng Qian of the Department of Materials Science and Engineering.

The crystal data and structure refinements depicted in Chapter II, III and IV were conducted by Dr. Shuai Yuan, Dr. Jiandong Pang, Dr. Yu Fang, Professor Bao Li, and Zhifeng Xiao. The simulation results depicted for Chapter III was provided by Lan Huang and Professor Tahir Cagin. The porous coordination cage in Chapter IV were provided by Dr. Yu Fang and Zhifeng Xiao.

All other work described in the dissertation was completed by the student independently.

Funding Sources

This work was supported in part by the National Energy Technology Laboratory, funded under the U.S. Department of Energy Office of Fossil Energy under award #DE-FE0026825 (Porous Polymer Network Membranes with Porous Molecular Additives for Post-Combustion CO2 Capture), Center for Gas Separations, an Energy Frontier Research Center funded by the U.S. Department of Energy, Office of Science, Basic Energy Sciences under Award # DESC0001015 (CO2 separations and initial MOP studies and the Robert A. Welch Foundation through a Welch Endowed Chair to H.J.Z. (A-0030).

NOMENCLATURE

AB	Ammonia Borane
ACQ	Aggregation Caused Quenching
BDC	1,4-benzenedicarboxylate
BET	Brunauer–Emmett–Teller
BPDC	biphenyl-4,4’-dicarboxylate
BTC	1,3,5-benzenetricarboxylate
CBs	Conduction Bands
COF	Covalent Organic Framework
DMF	N,N-dimethylformamide
DMSO	Dimethyl Sulfoxide
DRIFTS	Diffuse Reflectance Infrared Fourier Transform Spectroscopy
EDS/EDX	Energy Dispersive X-ray Spectroscopy
FCC	Face Centered Cubic
HSAB	Hard/Soft Acid/Base Theory
LED	Light Emitting Diode
LUMO	Lowest Unoccupied Molecular Orbital
MIL	Matériaux Institut Lavoisier
MOF	Metal Organic Framework
MS	Mass Spectroscopy
NDC	2,6-naphthalene dicarboxylate

NMR	Nuclear Magnetic Resonance
NP	Nanoparticle
PCC	Porous Coordination Cage
PL	Photon Luminescence
POP	Porous Organic Polymer
PXRD	Powder X-Ray Diffraction
SBU	Secondary Building Unit
SCXRD	Single Crystal X-ray Diffraction
SEM	Scanning Electron Microscopy
TEM	Transmission Electron Microscopy
TGA	Thermogravimetric Analysis
THF	Tetrahydrofuran
TOF	Turnover Frequency
UiO	University of Oslo
UV-Vis	Ultraviolet Visible Spectroscopy
XPS	X-ray Photoelectron Spectroscopy
ZIF	Zeolitic Imidazolate Framework

TABLE OF CONTENTS

Page

LIST OF FIGURES

LIST OF TABLES

Page

CHAPTER I

INTRODUCTION

1.1 Introduction of Metal-organic Frameworks (MOFs)

As an emerging class of crystalline porous materials, metal–organic frameworks (MOFs) possess fascinating structures. Due to their structural and functional tunability as well as their ever-expanding application scope, MOFs have become one of the most fascinating classes of materials for both scientists and engineers. Research into MOFs, which are also known as porous coordination polymers (PCPs) or porous coordination networks (PCNs), is mainly driven by the diverse applications of the frameworks, including gas sorption and separation,[1-2] luminescence,[3] catalysis,[4-5] and etc.[6-8] MOFs can be treated as coordination compounds assembled by metal ions and organic linkers generating intrinsically porous structures with cavities (cages, pores, or channels). The modular nature of MOFs is derived from the rational combination of various metal nodes and organic linkers. Together, these impart adjustable porosity, tunable functionality, and a designable topology.[9] One of the representative examples of this is the construction of MTV-MOFs (multivariate MOFs) by Yaghi *et al*. In this work, up to eight linear linkers with the same length but with distinctly different functional groups were introduced into one parent framework.[10] The availability of diverse building blocks comprised of metals and organic linkers make it possible to construct MOFs with tunable pore sizes, shapes, and environments.[11] As a result, MOFs represent a feasible platform for post-synthetic modifications.[12] A toolbox for post-synthetic modifications including: linker-exchange,[13-21] linker-installation,[22-24] linker-deprotection,[25-27] linker-labilization,[28] and metalation[29-32] has been developed. Furthermore, the mixed-linker strategy provides more opportunities to construct multifunctional MOFs.[33-34]

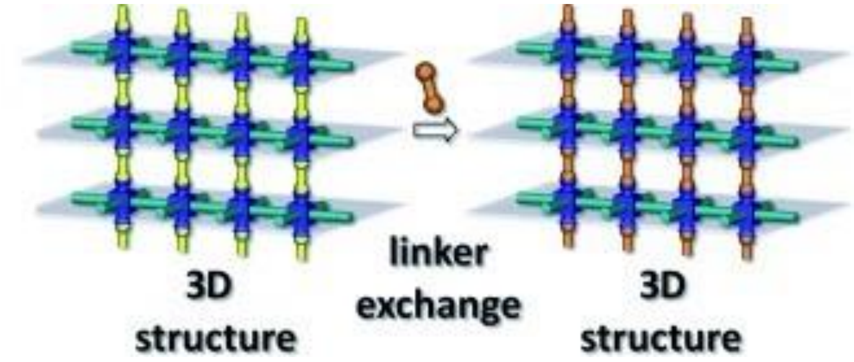

Figure I-1. Demonstration of linker-exchange. Reproduced with permission form *Angew. Chem. Int. Ed.*, **53**, 4530-4540.[18] Copyright 2014 Wiley.

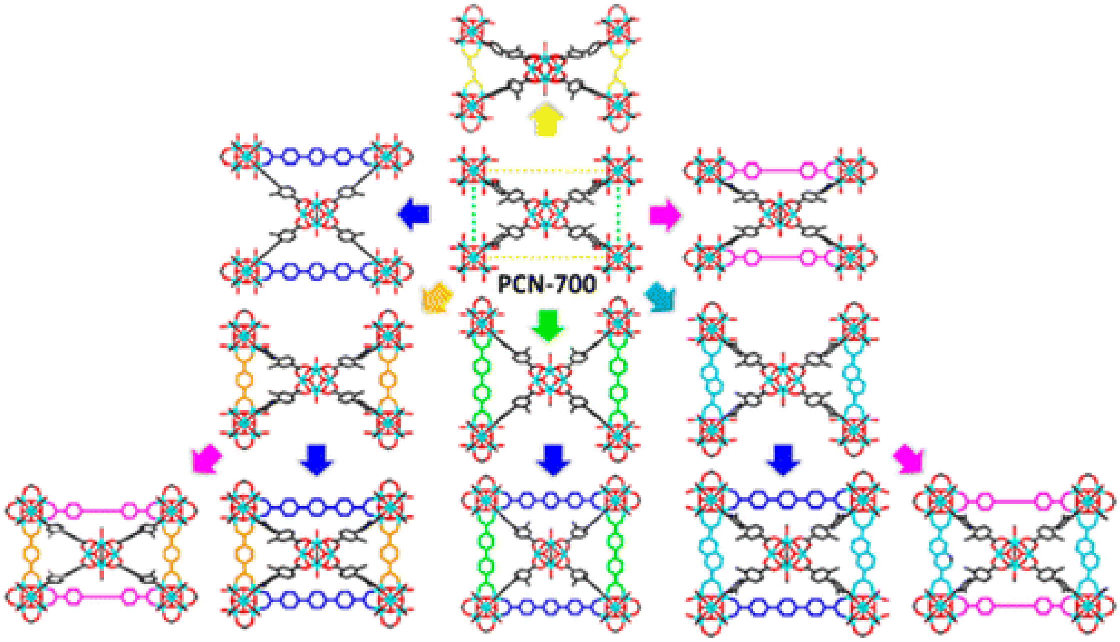

Figure I-2. Demonstration of linker-installation. Reproduced with permission form *J. Am. Chem. Soc.*, 2016, **138**, 28, 8912-8919.[22] Copyright 2016 American Chemical Society.

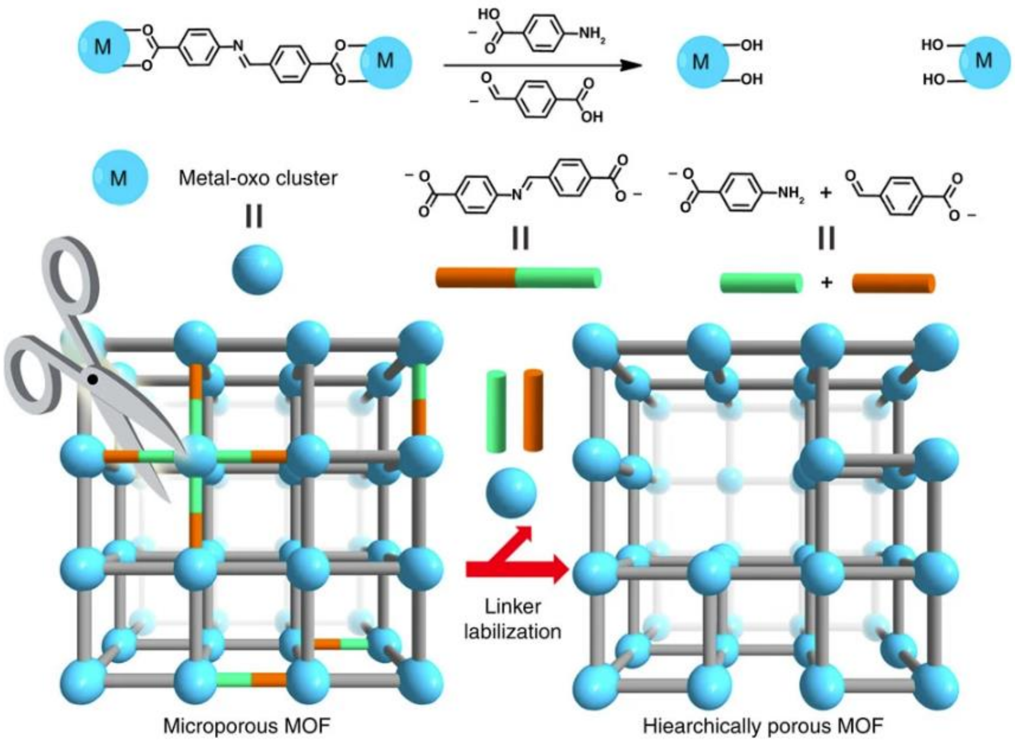

Figure I-3. Demonstration of linker- labilization. Reproduced with permission form *Nat. Commun.*, **8**, 15356.[28] Copyright 2017 Nature.

The structural diversity and tunability of MOFs enable all MOF components, such as nodes, linkers and pores, to be modified with various catalytic sites into a single material.[35-36] Generally speaking, MOFs as catalysts possess the following advantages over traditional porous materials (such as zeolites, clays, or mesoporous silica): (i) uniformly dispersed catalytically active sites on the pore surfaces at the molecular level, (ii) tunable hydrophilic and hydrophobic pore environments that are suitable for the recognition and transportation of reactants and products, and (iii) a collaborative microenvironment that is favorable for synergistic catalysis.[9]

Many early MOFs were made from divalent metals, such as Zn^{2+} or Cu^{2+} and were shown to have exceptional porosity. They held great promise for a wide variety of applications in many fields.[37] However, the weak stability of these early MOFs under harsh working conditions remained a problem. A classic example of an early MOF is MOF - 5.[38] This framework was considered to be a prominent milestone in MOF research. However, this framework gradually decomposes upon exposure to moisture in air, limiting its usability in practical settings. The utilization of MOFs for a desired application requires that their framework integrity be guaranteed in order to maintain their intended framework functionality and characteristics. As most industrial processes entail the presence of water or moisture, framework stability toward aqueous acid/base or coordinating anions are often required. As a result, the instability of many MOFs in water or other harsh conditions has considerably limited their further application and commercialization. Therefore, fundamental studies into the chemical stability of MOFs has received more and more attention over the last five years. Researchers have started to address the stability of MOFs in different environments, focused on understanding the possible decomposition pathways for the materials under operational conditions, and are attempting to develop more stable framework structures as a result.[39-41]

The stability of MOFs can be affected by multiple factors, including the operating environment, metal ion identity, organic ligand functionality, metal–ligand coordination geometry, hydrophobicity of the pore surface, etc.[39, 42-43] Studies on the stability of MOFs have allowed us to rationalize the effect of some factors and judiciously design stable framework structures as a result. The relatively labile coordination bonds that support the framework structures are believed to be responsible for the limited stability of the MOF scaffold.[44] Thus a stable MOF structure should have well matched coordination bonds according to hard/soft acid/base theory (HSAB) to survive attack of guest molecules or possess steric hindrance to prevent the intrusion of guests to the metal nodes.

The metal–ligand bond strength determines the thermodynamic stability of MOFs under many operating environments. Therefore, the stability of MOFs can be roughly predicted by examining the strength of the bonds that form the framework. It is known that the metal–ligand bond strengths with a given ligand are positively correlated to charges of the metal cations and are negatively correlated to the ionic radius. The effects of charge and radius can be combined into the concept of charge density. When the ligands and the coordination environment remain the same, high-valent metal ions with high charge densities can form stronger coordination bonds and thus a more stable framework. This trend is in line with Pearson's hard/soft acid/base (HSAB) principle and corroborated by many observations in MOF research.[40] The carboxylate based ligands can be regarded as hard bases, which form stable MOFs with high-valent metal ions, such as Ti^{4+}, Zr^{4+}, Al^{3+}, Fe^{3+}, and Cr^{3+}, which can be regarded as hard acids. Early work on high-valent metal based MOFs was established by Férey *et al.* who developed the Al^{3+}, Fe^{3+}, and Cr^{3+} based MIL series (MIL stands for Material Institut Lavoisier) including well-known MIL-53,[45] MIL-100,[46] and MIL-101. The Zr^{4+} based MOFs were first synthesized in 2008 and have attracted considerable attention due to their remarkable stability in water and acidic conditions.[47]

According to the HSAB principle, stable MOFs can also be assembled by soft azolate ligands (such as imidazolates, pyrazolates, triazolates, and tetrazolates) and soft divalent metal ions (such as Zn^{2+}, Cu^{2+}, Ni^{2+}, Mn^{2+}, and Ag^{+}). The most representative examples of this type of coordination are the zeolitic imidazolate frameworks (ZIFs) which are constructed by Zn^{2+} and imidazolate linkers.[48] In addition, Long and co-workers have developed triazole and pyrazolate-based MOFs which are known to exhibit good stability in alkaline environments.[49-50]

In addition to the influence of bond strength on the framework thermodynamic stability, the stability of MOFs can also be affected by kinetic factors. A simple consideration of the bond strength of MOFs based on thermodynamics could result in inaccurate predictions that contradict experimental results. For example, UiO-66, UiO-67, and UiO-68 (UiO stands for University of Oslo) are isostructural MOFs that have the same $[Zr_6(\mu_3\text{-}O)_4(\mu_3\text{-}OH)_4(COO)_{12}]$ cluster but different linker lengths.[47] Based on a thermodynamic argument, these frameworks might be expected to show similar stability according to their bond strengths. However, experimental results show a decreased stability of the framework with an increase in linker length. This inconstancy can be rationalized by noting how the rigidity of linkers affects the kinetic stability. Dense and rigid structures formed by highly connected metal-oxo clusters and rigid organic linkers are usually more stable. This is in line with the good stability of high-valence metal clusters which tend to have higher coordination numbers and thus more rigid framework structures. Additionally, by specially designing hydrophobic surfaces or interfaces, water and other guest molecules can be excluded from approaching metal ions. For example, Omary *et al.* developed a series of fluorinated MOFs (FMOFs) with remarkable water stability as a result of super-hydrophobicity.[51] In addition, several publications have shown that postsynthetic treatment of labile MOFs with hydrophobic coatings can generate water-stable MOF composites.[52-58]

With increased attention towards MOF stability and an improved understanding of the fundamental factors that affect the structural stability of these scaffolds, studies on stable MOFs have flourished in the last few years. The ever-increasing number of stable MOFs has significantly expanded the application of this class of materials. Recent advances in MOFs have focused on new applications such as catalysis, biomedicine, and chemical sensing.[39] An example of this is in the use of MOFs as photocatalysts for catalytic water splitting and CO_2 reduction. This application requires the framework to be stable in aqueous solutions containing acid, base, or coordinating anions.[59-60] In the following parts, some stable MOFs will be introduced based on their different applications, such as fluorescence sensors, bio-related applications and metal nano-particles composites.

1.2 Properties and Potential Applications

1.2.1 Metal-organic Frameworks as Fluorescence Chemical Sensors

Because of the unique tunability and porosity of Metal-Organic Frameworks, numerous of fluorescent species have been incorporated into MOF to achieve fluorescent scaffolds through encapsulation, linker installation, or pendent group modification. Based on the fluorescent source, most fluorescent MOF can be divided into followed three categories: MOF with fluorescent metals, with fluorescent backbone and with fluorescent molecules adsorbed inside the pore or on the surface of MOF.[61] In this section, only MOF with fluorescent backbone will be introduced, due to its close relationship to chapter II and III.

Due to their rigidity, various π-conjugated organic molecules have been chosen as MOF linkers. Most of them have rigid backbones and are functionalized with multi carboxylate groups or heterocyclic groups to form coordination bonds between metal and organic linkers. Under most circumstances, the fluorescence emission of the organic ligands in the scaffold is similar to their emission in solution. However, other fluorescence properties such as lifetime and emission wavelength peak are often shifted. This can be attributed to a reduction of the non-radiative decay rate caused by stabilization of the linkers incorporated into a MOF. When serving as a backbone unit in the MOF, the distance between the molecules are much closer than they are in free solution. This proximity enables charge transfer between the linkers to occur, resulting in the shift of the emission spectrum[3]

One example of an emission spectrum shift was reported by Zhang *et al.* In their work, they synthesized a $[Zn_3(\mu_5\text{-}PTC)_2(\mu_2\text{-}H_2O)_2]_n$ (H_3PTC= pyridine-2,4,6-tricarboxylatic acid) MOF with a strong blue fluorescence.[62] As compared to the weak fluorescence intensity of free H_3PTC at 415 nm, excited under 338 nm, the MOF demonstrated a strong red-shifted emission at 467 nm. This may be attributed to an increased rigidity of the PTC bound in the scaffold and a decrease of the intra-ligand HOMO–LUMO energy gap distance.

Another example comes from Qiu *et al.* In their work, they synthesized two multifunctional microporous MOFs: $Zn_3(BTC)_2(DMF)_3(H2O)$ and $Cd_4(BTC)_3(DMF)_2$, (H_3BTC=1,3,5-benzenetricarboxylic acid).[63] Free BTC ligands were determined to have emission peaks at 370 nm under an excitation of 334 nm. However, the coordinated MOFs showed a red shift in the emission peak at 410 nm (Zn MOF) and 405 nm (Cd MOF). This was determined to be caused by the change in the identity of the metal ions and the coordination environment which interfere with the energy of $\pi^* \rightarrow n$ transitions.

Most of the researches utilizing fluorescent MOFs as different kind of sensors instead of only demonstrating the differences in fluorescent properties compared with free ligands. Dinca et al. introduced a method called matrix coordination-induced emission effect (MCIE) which is complementary to the aggregation-induced emission (AIE) effect.[64] In their study, $Zn_2(TCPE)(H_2O)_2$ and $Cd_2(TCPE)(H_2O)_2$ (H_4TCPE=Tetrakis(4-carboxyphenyl)ethylene) were synthesized. The key fluorescent part of TCPE is the TPE (tetraphenylethylene) part of the molecule. The fast rotation of the phenyl rings and the partial twisting of the C=C bond of TCPE quenches its fluorescence in dilute solutions. When TCPE aggregates, the short intermolecular interactions reduce the rotation of the phenyl groups and show a green fluorescence. (Figure I-4) A Zn-MOF was tested as a molecular sensor in this study and it was demonstrated to respond differently under exposure to different analytes: a blue shift from 467nm to 457nm was observed after exposure to ethylenediamine, while a red shifts of 6nm and 10 nm occurred upon exposure to cyclohexanone and acetaldehyde, respectively. The same group also summarized the strategies to improve the fluoresce properties of MCIE MOFs.[65] These strategies included:

(1) Designing MOFs where AIE-type chromophores are well separated spatially. This is necessary to avoid aggregation in the empty material and to ensure porosity for the analyte adsorption; (2) maintaining the flexibility in the TPE core to ensure that low-energy vibrational modes are not eliminated in the empty material. This could be implemented, for instance, by leaving two dangling/unsubstituted phenyl rings which should maintain dynamics in the fast flipping regime; and (3) minimizing ligand conjugation to reduce the contribution of an electronic component to the ring-flipping barrier. This could be achieved, for instance, by enforcing a perpendicular orientation between the ethylene core and the metal-binding functional groups, by using acetylene spacers to 'insulate' the phenyl ring from orientation-inducing conjugation, or by using non-conjugating ligating groups.

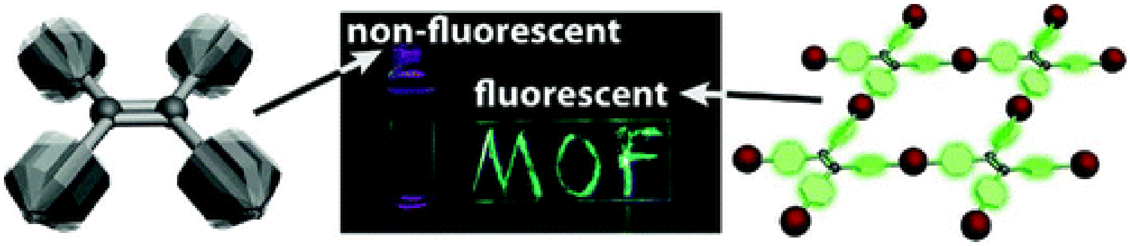

Figure I-4. Turn-On Fluorescence of TCPE by Coordination in a Rigid MOF Matrix (MCIE). Reproduced with permission form *J. Am. Chem. Soc.* 2011, 133, 50, 20126-20129.[64] Copyright 2011 American Chemical Society.

Gu *et al.* first reported a luminescent MOF for chemical sensing of dissolved oxygen (DO).[66] In their work, a sample of 1 μm^3 cubic PCN-224(Pt) MOF particles were synthesized via solvalthermal methods by mixing $ZrOCl_2 \cdot 8H_2O$ and TCPP(Pt) (Pt(II) meso-Tetra (4-carboxyphenyl) porphine). The sensitivity of the oxygen probe was evaluated by the luminescent quenching percentage in the saturated N_2 and O_2 solutions

$((I_{N_2} - I_{O_2})/I_{N_2}$, where I_{N_2} and I_{O_2} denote the phosphorescent intensities of the sensor in saturated nitrogen and oxygen solutions, respectively). As demonstrated in Figure I-5, phosphorescent intensity of the PCN-224(Pt) suspension gradually decreases with an increase of the DO level. Furthermore, the phosphorescence quenching process could be described by linear equation. PCN-224(Pt) was shown to have a sensitivity of around 88% after the testing temperature and excitation wavelengths were optimized. PCN-224(Pt) also showed similar performance as a DO electrode in real-time monitoring of DO in enzyme-catalytic process.

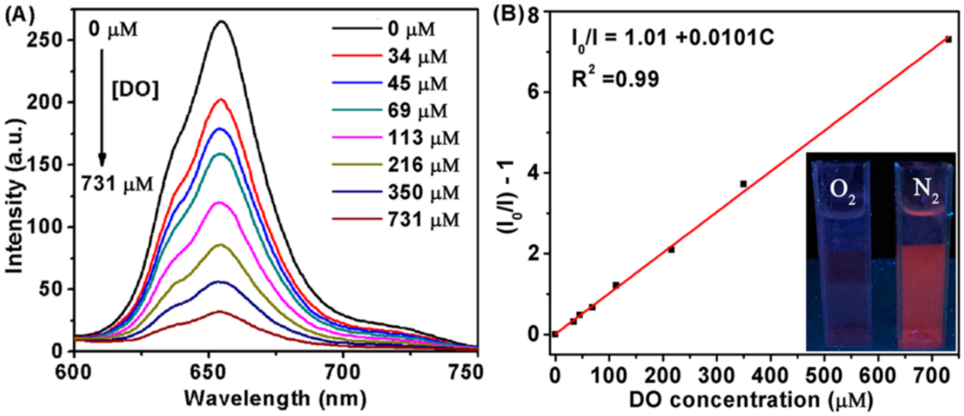

Figure I-5. (A) Evolvement of the phosphorescent spectra of the PCN-224(Pt) (50 mg L^{-1}) suspension with DO level increasing. (B) The corresponding Stern−Volmer plot of the phosphorescent intensity of the PCN-224(Pt) suspension as a function of DO concentration. The inset: the digital pictures of the PCN-224(Pt) suspension in N_2-saturated and O_2-saturated aqueous solutions illuminated by a hand-held UV lamp with an irradiation wavelength of 365 nm. Reproduced with permission form *Chem. Mater.* 2016, *28*, 8, 2652-2658.[66] Copyright 2016 American Chemical Society.

Maji et al. synthesized a 3D functional metal−organic framework, $[K_8(PTC)_2(H_2O)_{1.5}]\cdot 4H_2O$, which was formed through the self-assembly of chromophoric linker perylenetetracarboxylate (PTC) and K^I.[67] In the solid state, PTC prefers to form sandwich-type H-aggregates, which exhibit a sufficiently quenched fluorescence due to delocalized excitons or excimer formation. However, the crystal structure showed that the MOF had a 3D pillared-layer framework, where perylene cores are arranged in an unusual end-to-end off-slipped and zigzag arrangement directed by K^I-carboxylate bonding. Due to this unique structure, the MOF was shown to have a significantly red shifted red emission at 655 nm under excitation at 485 nm as compared to the green emission of the monomer at 480 nm.

Kaskel *et al.* reported a fluorescent MOF based on UiO-66 ($Zr_6O_4(OH)_4(BDC)_6$, BDC=benzene-1,4-dicarboxylate) able to detect toxic gases: NO, NO_2, and Br_2.[68] These gases were chosen because of their ability to act as strong oxidizers. Through post-synthetic modification of the framework, dihydro-1,2,4,5-tetrazine-3,6-dicarboxylate (DHTZ) ligands were demonstrated to be able to replace a fraction of the BDC ligands within the structure of UiO-66. The BDC:DHTZ ratio of the resulting UiO-66(dhtz) was determined to be 5:1. The DHTZ unit was chosen because it can be easily oxidized to 1,2,4,5-tetrazine (tz), and for the fact that this oxidation results in a clear red shift from yellow to pink as a result of increased blue-green light absorbance. This oxidation could be fully reversed by suspending UiO-66(tz) in an aqueous solution with the reducing agent sodium dithionite. PXRD and gas adsorption measurements of the sample demonstrated that the structure's crystallinity and porosity was not affected by the post-synthetic ligand replacement, oxidative sensing, or reductive regeneration.

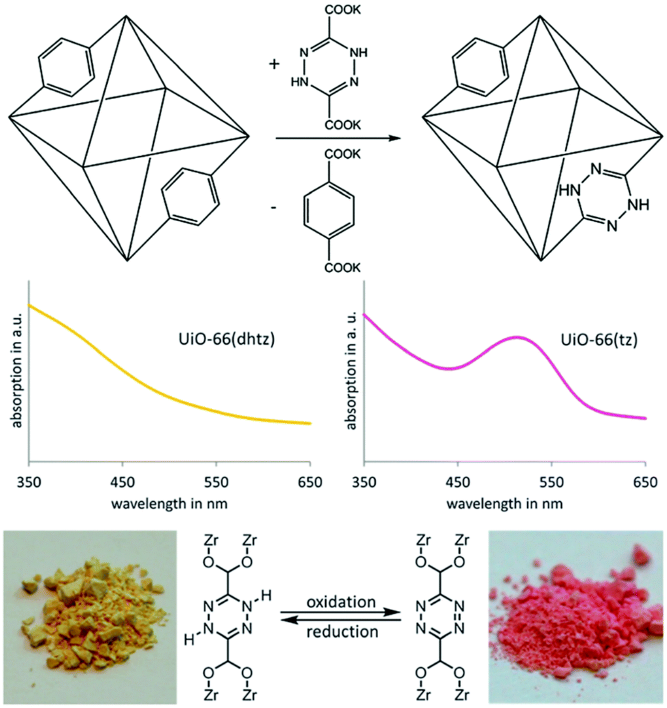

Figure I-6. (top) Postsynthetic ligand replacement of BDC with DHTZ to give UiO-66(dhtz). (bottom) The fully-reversible oxidation of UiO-66(dhtz) to UiO-66(tz) in the presence of NO, NO_2, or Br_2 gases. Reproduced permission from ***Chem. Commun.***, 2015, **51**, 2280-2282.[68] Copyright 2015 Royal Society of Chemistry.

1.2.2 Bio-related Applications of Metal-organic Frameworks

A unique class of hybrid materials that has demonstrated a wide range of functionalities, Metal-Organic Frameworks (MOFs) have been explored as an alternative solution for various applications. MOFs are well known for their extensive porosity and highly tunable pore sizes and shapes,[69] making them highly sought after for gas storage and separation applications,[70] where size exclusion plays a significant role. However, there has been an increasing interest in expanding the role of MOFs beyond gas storage through functional design and tuning into, for example, biomedical applications. This section will focus on recent advances in MOF applications in the biomedical field. These studies take advantage of the high tunability of MOFs, particularly the incorporation of functional groups or molecules within the scaffold.

In the existing literature, there are four main methods for developing a bio-MOF composite; surface attachment, covalent linkage, pore encapsulation, and co-precipitation.[71] This section will focus on three of these methods: surface attachment, covalent linkage and pore encapsulation, as these are methods these are essential for the development of surface modified MOFs.

1.2.2.1 Surface Attachment for the Synthesis MOF-bio Composite Materials

There are two main type of enzyme-MOF composites that have been explored in the last few years. A common approach is the immobilization of enzymes within the porous structure of the MOF. Using the MOF as a protective scaffold, the enzymes are provided with an additional degree of stability for use in non-conventional environments. Additionally, it has also been noted that the immobilization of enzymes in MOFs result in an increased enzymatic activity when compared to the free enzyme. This is directly related to the compatibility between the pore and enzyme. This interaction often results in more readily available active sites.

The second method, which will be presented in this section is the surface attachment of enzymes to MOF crystals. While this method might not provide as many improvements to the overall chemical stability, it is the most straightforward method for immobilizing enzymes in MOFs. With this method, enzymes are bound to the surface of MOF microcrystals via weak non-covalent intermolecular interactions, such as electrostatic interactions, π-π stacking, and hydrophobic interactions. Thus, due to the ease of chemical attachment, a wide variety of enzymes can be immobilized on the surface of a broad range of MOFs via the surface attachment method.

The very first example of enzyme-immobilization utilizing MOFs was achieved through utilizing the surface attachment approach. In their work, Balkus *et al.* tested and compared the catalytic activities of microperoxidase-11 (MP-11) immobilized on five mesoporous benzene silicas (MBSs) and a Cu-MOF ([Cu(bpdc)(dabco)], bpdc = biphenyl-4,4'-dicarboxylate, dabco = 1,4-diazabicyclo[2.2.2]-octane).[72] the MP-11 enzyme catalyzes the oxidation of dye molecules, such as Amplex UltraRed and Methylene Blue in the presence of H_2O_2. This is a reaction that can be monitored by UV-Vis. The performance of MP-11 was measured in a phosphate buffer solution. When immobilized on the MBSs, the percent conversion of Amplex UltraRed was only one-third that of free MP-11. Contrasting this, the enzyme-MOF complex, MP-11@Cu-MOF, showed a 10-fold increase in conversion over the free enzyme when catalyzing Methylene Blue oxidation. It is worth noting that the amount of immobilized MP-11 in the Cu-MOF was 30 μmol/g, while the maximum loading of the five MBSs was only 20 μmol/g. The loading difference between the MBSs and MOF can be attributed to the larger surface area and more polar nature of the Cu-MOF. The surface area decreased after enzyme immobilization was nearly 100% for the MBS samples while it was only 67% for the Cu-MOF, even though the Cu-MOF had a higher loading. The catalytic differences of the enzyme-support material could have been a direct result of the accessible surface area. A larger surface area allows for the improved mass transfer during the reaction, thus enhancing the reaction rate. This work demonstrated the improved performance of MOFs over MBSs for enzyme immobilization, leading to the development of MOF-enzyme composites as a field of study.

Building off of this early work, Legrand *et al.* used a MIL (MIL: Matériaux Institut Lavoisier) series of MOFs and platinum nanoparticles to immobilize glucose oxidase (GOx) onto the MOF surface via surface attachment. This composite material was used as a bioelectrode.[73] The authors synthesized several mesoporous metal (III) (Metal = Fe^{3+}, Cr^{3+}, Al^{3+}) MOFs with high surface areas and biocompatibility in the study. To prepare the bioelectrode, the authors used a step by step electrodeposition method. Firstly, the carbon ink electrode (CIE) surface was decorated with Pt NPs by electrodeposition. Then, solutions of MOFs and GOx were successively deposited on the surface of the Pt NP–CIE which permitting the formation of layers of MOF and GOx. Finally, the electrode was coated with a protective layer of a cross linked porous polymer, glutaraldehyde, as well as bovine serum albumin solution. This method of surface attachment of enzymes resulted a stable composite material. The IR and SEM studies (Figure I-7) demonstrated that both the enzyme morphology and the structure of the enzyme remains unchanged after the surface attachment of the enzymes in the MOF matrix. The authors have used these electrodes as glucose amperometric biosensors with high sensitivity and low response time.

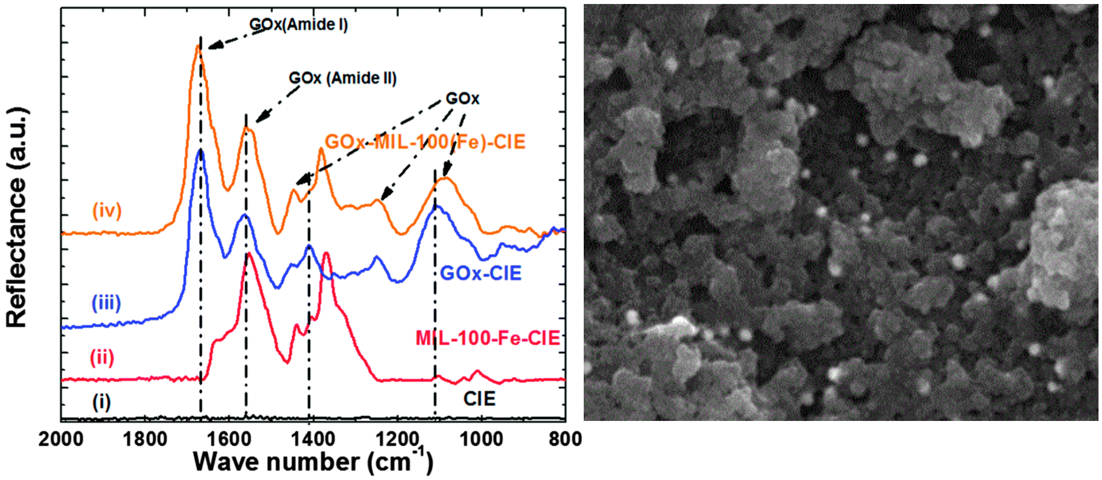

Figure I-7. FT-IR spectra of (i) CIE, (ii) MIL-100(Fe)–CIE, (iii) GOx–CIE and (iv) GOx–MIL-100(Fe)–CIE (all spectra are baseline-corrected). SEM image of GOx–MIL-100(Fe)–CIE. Scale bar 1 µm. Reproduced with permission from *J. Mater. Chem. B.*, 2015, *3*, 8983-8992.[73] Copyright 2015 Royal Society of Chemistry.

Another example comes from Liu *et al.*[74] who immobilized bacillus subtilis lipase (BSL2) on a hierarchically porous HKUST-1 ([$Cu_3(BTC)_2$], BTC = 1,3,5-benzenetricarboxylate) scaffold. A previously reported non-ionic surfactant was used to modified BSL2 as a homogenizer. The BSL2–surfactant complexes were further immobilized in HKUST-1 by immersion in an isooctane solution for 8 hours under stirring at 25 °C. The performance of the immobilized BSL2 was tested by an esterification reaction between benzyl alcohol and lauric acid. The reaction was monitored through gas chromatography every 20 minutes to calculate enzymatic activity and a conversion percentage. The immobilized BSL2 showed significantly better enzymatic activity as compared to the free enzyme in dry isooctane. The initial rate of the immobilized BSL2 was nearly 17 times higher than that of free BSL2, which can be contributed to that BSL2 was sufficiently dispersed in the mesopores of HKUST-1 particles avoiding the aggregation of free enzyme. In addition, the reusability of BSL2@HKUST-1 was shown to be excellent with only a small drop in conversion after 10 cycles.

Another example comes from Huang *et al.*[75] who explored four microporous MOFs: UiO-66 ([$Zr_6O_4(OH)_4(BDC)_6$], BDC = 1,4-benzenedicarboxylate), UiO-66-NH_2 ([$Zr_6O_4(OH)_4(NH_2\text{-bdc})_6$], NH_2-bdc = 2-amino-1,4-benzenedicarboxylate), MIL-53 ([Al(OH)(BDC)]), and carbonized MIL-53 for enzyme surface attachment in MOFs. In their study, porcine pancreatic lipase (PPL), an enzyme with dimensions of 4.6 × 2.6 × 1.1 nm^3, was physically adsorbed onto the freshly prepared MOFs through surface attachment, generating a series of PPL@MOFs. Several characterization techniques, including FTIR, PXRD, and SEM, were used to confirm the successful attachment of PPL onto the MOFs and that the crystallinity of MOF matrices was retained. The PPL@MOF bioreactor was used to catalyze a Michael addition reaction between 4-hydroxycoumarin and benzylideneacetone to yield warfarin. Warfarin is a common anticoagulant used in medical practices. The catalytic activity of the PPL@MOF bioreactor was determined by capillary electrophoresis. The activity of the PPL immobilized in the UiO-66-NH_2(Zr), MIL-53(Al), and carbonized MIL-53(Al) scaffolds was well maintained even in the fifth usage cycle. Additionally, after storage for 35 days at 4 °C, the PPL@MOF series showed no significant drops in catalytic activity, indicating the reasonable storage stability of this surface-bound enzyme.

As MOF-enzyme composites are formed with weak interactions for surface attachments, enzyme leaching is one of the main challenges for this material. This problem ultimately limits the reusability of the composites long term. To circumvent this problem, Huang *et al.* designed a novel trypsin–FITC@MOF bioreactor with high protein digestive efficacy.[76] In this case, a green fluorophore, fluorescein isothiocyanate (FITC), was conjugated to trypsin to act as an anchor, facilitating enzyme immobilization. The conjugation of FITC on trypsin was assisted by microwave treatment for 2 min, and then was immobilized on an aluminum MOF, CYCU-4 ([Al(OH)(sdc)], sdc = 4,4-stilbenedicarboxylate), with 30 min of vortex mixing. CYCU-4 features a structure with both micropores and mesopores that are suitable for accommodating the FITC molecule conjugated to trypsin. Digestion of bovine serum albumin (BSA) proteins under ultrasonication, a typical method of catalytic analysis of trypsin, was used to study the enzymatic activity of trypsin–FITC@CYCU-4. With the proteolytic fragments of the BSA protein determined by nano LC-MS followed by Mascot database searching, trypsin–FITC@CYCU-4 obtained 47 matched peptides and 72% sequence coverage which was comparable to the performance of free trypsin–FITC and was much better than that of other studied MOFs including MIL-101(Cr) ($[Cr_3F(H_2O)_2O(BDC)_3]$), MIL-53(Al), DUT-5(Al) ([Al(OH)(bpdc)]), DUT-4(Al) ([Al(OH)(NDC)], NDC = 2,6-naphthalene dicarboxylate), *etc.* It is worth noting that the preparation of trypsin-FITC@CYCU-4 was fast and did not require any surface modification on the MOFs, thus eliminating the production of volatile organic waste. The Huang group further extended this dye-assisted enzyme immobilization by synthesizing trypsin immobilized CYCU-4(Al), UiO-66(Zr), MIL-100(Cr) and MIL-101(Cr) MOFs using a multipoint immobilization method.[77] In this study, a smaller dye molecule, 4-chloro-7-nitrobenzofurazan (NBD), was used instead of FITC as in the previous report. The size of NBD is compatible with the pore size of many microporous MOFs. Since at least 3 or 4 NBD molecules are able to bind to a single molecule of trypsin, multipoint immobilization of the dye-tagged enzyme was utilized. The proteolytic efficiency of immobilized trypsin was measured based on BSA digestion, and the peptide sequence coverage was determined from the peaks obtained in nano LC-MS and identified by the Mascot database. Trypsin@UiO-66 and trypsin@CYCU-4 demonstrated the highest BSA digestion efficiency of 69–71%. This could be attributed to their pore sizes of the MOF as they are compatible with the size of the NBD molecules.

Another work by Ma *et al.* used zeolitic imidazolate framework surface (ZIFs) as a matrix to allow for co-immobilization of methylene green (MG) and glucose dehydrogenase (GDH) in order to fabricate an integrated biosensor.[78] In this report, the MG/ZIF composite was synthesized followed by coating with GDH. This resulted in a sensor with high glucose sensitivity ranging from 0.1–2 mM. In the testing process, 5 different ZIFs were used: ZIF-7 ($[Zn(bIm)_2$, bIm = benzimidazole]), ZIF-8 ($[Zn(mIm)_2]$, mIm = 2-methylimidazole), ZIF-67 ($[Co(mIm)_2]$), ZIF-68 ($[Zn(bIm)(nIm)]$, nIm = 2-nitroimidazole), and ZIF-70 ($[Zn(Im)_{1.13}(nIm)_{0.87}]$, Im = imidazole). ZIF-70 was found to have the best performance in the desired range. Tests of the ZIFs with MG and GDH were performed separately and it was shown that ZIF-70 had the best combined adsorption of both moieties. The combined effects of MG as an electrocatalyst and GDH as a detector for continuous measurements resulted in a sensitive biosensing system that systematically adsorbed the two species onto the ZIF framework.

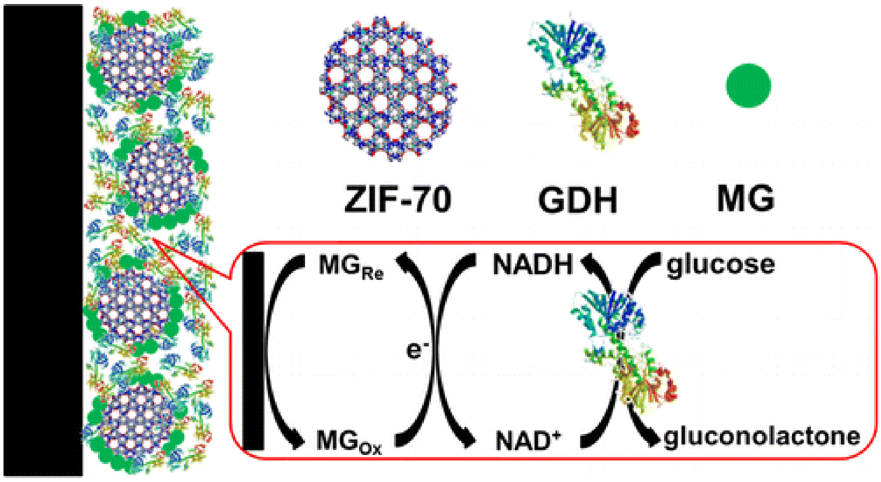

Figure I-8. Schematic Representation of catalysis done by MOF enzyme composite. Reproduced with permission from *Anal. Chem.*, 2013, *85*, 7550-7557 2013.[78] Copyright American Chemical Society.

A report by Zhou *et al.* also recently reported an enzyme MOF nanoreactor where super oxide dismutase enzyme and catalase were both encapsulated inside PCN-333 nanoparticles in a stepwise fashion.[79] PCN-333 is a MOF combrised of trimeric clusters and TATB ligands. This scaffold is synthesized through self-assemble and generates supertetrahedra structures (highlighted in red dashed circle) in Figure I-9. The supertetrahedra are linked in a vertex-sharing manner.The MOF surface was modified with a green fluorophore via ligand metathesis. Several characterization techniques like PXRD and TEM were used to confirm the MOF crystallinity. The water-soluble tetrazolium (WST) and horseradish peroxidase (HRP)-Amplex Red assays were performed. The surface attached fluorophore was shown to be helpful for tracking the MOF-enzyme nanoreactor inside the cells via several fluorescent assays.

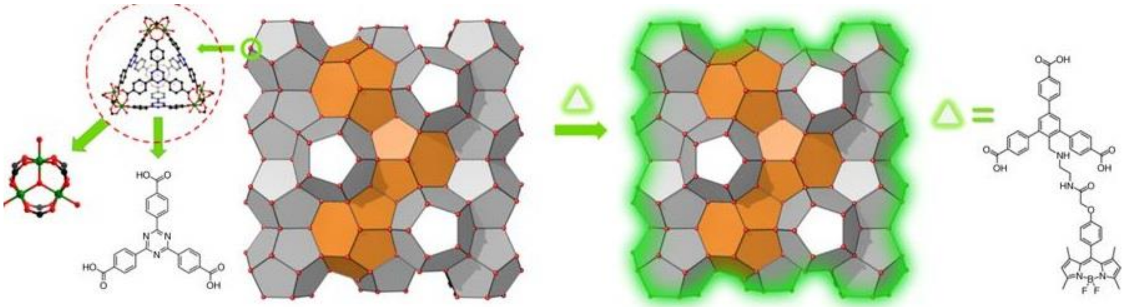

Figure I-9. Schematic representation of PCN-333 stucture and modification of surface with green fluroscent probe. Reproduced with permission from *Nat. Commun.*, 2017, *8*, 2075.[79] Copyright 2017 Nature.

1.2.2.2 Covalent Modification of MOF for Biomedical Applications

As compared to the weak intermolecular interactions used in non-covalent modifications, covalent linkages have much stronger interactions. Covalent bonds between MOFs and enzymes are generally considered to be irreversible, thus the composites can retain connectivity even after several catalytic cycles. There are two common methods employed in the formation of covalent bonds between MOF crystals and enzymes. The first is by employing free amino and carboxyl groups on either the enzyme, or the MOF. These functional groups can then be coupled through a peptide bond by using a variety of activating reagents.[80] Another method for composite formation is through the utilization of glutaraldehyde as a cross-linker to form imines with the amino groups from the enzyme and the MOF surface. Here a discussion of these methods is presented in detail.

An example of the first method was demonstrated by Park *et al.* where they synthesized serials of MOFs with different topologies and covalently conjugated proteins onto the surface of the MOFs.[81] In this study, a 1D-MOF was prepared from $In(NO_3)_3$ and

1,4-phenylenediacetic acid (H_2pda). Additionally, a 2D-MOF $[Zn(bpydc)(H_2O)\cdot(H_2O)]_n$ was prepared form 2,2’-bipyridine 5,5’-dicarboxylate (bpydc) and an IRMOF-3 was chosen as a 3D-MOF. The 1D-MOF was the only MOF that could be activated by 1-ethyl-3-(3-dimethylaminopropyl) carbodiimide (EDC) in aqueous media. The other MOFs in the study were activated by dicyclohexyl carbodiimide (DCC) in dichloromethane. This difference in activation was presumably due to the pda of the 1D MOF as aliphatic carboxylates are more reactive than the aromatic ones used in the 2D and 3D MOFs. After activation, these MOFs were incubated with enhanced green fluorescent protein (EGFP) in a PBS buffer solution. Although the IRMOF-3 sample was not stable in water, a 1h incubation was shown not damage the structure. A series of PXRD spectra revealed that all the MOFs maintained their crystallinity after the 1h incubation. It should be noted that both the 1D and 3D MOFs began to lose structural integrity after longer incubation times while the 2D MOF remained unchanged. A serials of confocal laser scanning microscope (CLSM) images taken on different focal planes demonstrated that the green emissions from the EGFP were on the surface of crystals. The amounts of EGFP loading onto the 1D, 2D, and 3D MOFs were determined to be 0.048, 0.052, and 0.064 mg/g respectively. The functional protein, Candida antarctica lipase B (CAL-B), was also covalently conjugated onto the surface of the MOFs. Protein loading onto the 1D, 2D, and 3D MOFs were 0.12, 0.17, and 0.18 mg/g respectively. The transesterification of (±)-1-phenylethanol was chosen as a model reaction and the enantioselectivity of the free CAL-B and immobilized CAL-B were measured. The immobilized CAL-B showed a several hundred fold increase in activity in the MOF composite samples, especially for the 3D-

MOF-CAL-B. The 3D MOF composite demonstrated a 1000-fold incrase while maintaining similar enantioselectivity as compared to free CAL-B. The enhanced performance could be attributed to the confined spaces in the MOF scaffold. This ensured that the enzyme active center was protected and a stable pH was maintained via neutralizing by-products utilizing the amino groups on the scaffold of IRMOF-3. A dual protein-conjugated 3D MOF for fluorescence and transesterification activity (38 μmol·min^{-1}·mg^{-1}) was successfully synthesized.

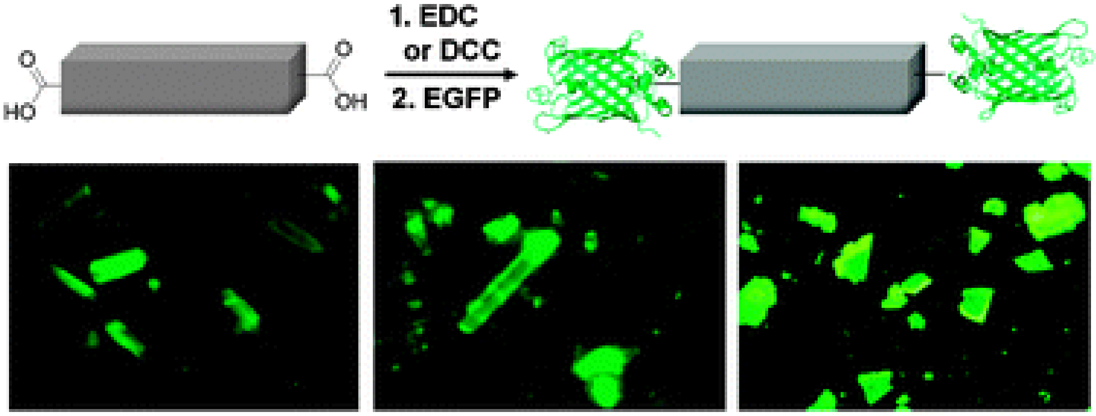

Figure I-10. Schematic representation of the bioconjugation of the 1D-polymer, $[(Et_2NH_2)(In(pda)_2)]_n$, with EGFP. Fluorescence microscopic images of EGFP coated MOFs. (a) 1D + EGFP. (b) 2D + EGFP. (c) 3D + EGFP. An Olympus WIB filter set (λ_{ex} = 460–490 nm; λ_{em} > 515 nm) was used for recording the fluorescence. Reproduced with permission from ***Chem. Commun.***, 2011,**47**, 2904-2906.[81] Copyright 2011 Royal Society of chemistry.

In another study, Lin *et al.* immobilized trypsin onto serials of MOFs for proteomic analysis.[82] MIL-101(Cr), MIL-88B(Cr), and MIL-88B-NH_2(Cr) were synthesized and activated by DCC. After activation, each MOF was modified through covalently bonding a trypsin guest molecule. The PXRD pattern of the MOF series revealed that the MOFs maintained their crystallinity after enzyme attachment and SEM images showed that the surface become more rough, indicating a successful surface attachment of trypsin. The Bovine serum albumin (BSA) protein was chosen as model protein to test the activity of the MOF composites for proteomic analysis. The amino acid sequence coverage and matched peptides were measured by nanoLC-MS2 (liquid chromatography–mass spectrometry) and standard protein searching (Mascot database). An new digestion procedure involving 2 min ultrasonication was conducted and resulted in higher amino acid sequence coverage (72 %) and matched peptides (46) compared by conventional 18 h digestion(60 %, 34). Surprisingly, MIL-101(Cr)-trypsin and MIL-88B(Cr)-trypsin only have half sequence coverage and matched peptides while MIL-88B-NH_2(Cr)-trypsin have better performance than free trypsin. The role of the amine group in the MOF scaffold in the digestion was further studied. Unactivated MIL-88B-NH_2(Cr)-trypsin showed no peptide signal during analysis, indicating that the amine group could facilitate the reaction between trypsin and BSA. The amine group was shown to increase the hydrophilicity and bio-compatibility of the MOF and reduce the non-specific adsorption of BSA. A much lower sequence coverage and matching of the peptides for the amorphous mixture of chromium chloride and NH_2-1,4-BDC with unpurified MIL-88B-NH_2(Cr) demonstrated that the crystallinity of the scaffold also plays an important role in digestion.

An example of a second method for the crosslinking type enzyme incorporation into a MOF was demonstrated by Lou *et al.* via immobilizing Soybean Epoxide Hydrolase (SEH) on UiO-66-NH_2 via glutaraldehyde (GA). They utilized this composite material for the asymmetric hydrolysis of 1,2-eposyoctane.[83] The SEH was mixed with UiO-66-NH_2 in phosphate buffer saline (PBS) and coprecipitated by 100% saturated ammonium sulfate solution at 4 °C, followed by a crosslink step via stirring with GA. The resulting SEH@UiO-66-NH_2 composite manifested high SHE loading at 87.3 mg/g. To avoid the possible degradation of the MOFs in the presence of water, a deep eutectic solvent (DES) were chosen for reaction. Both UiO-66-NH_2 and SEH@UiO-66-NH_2 maintained their original crystallinity as seen by the PXRD pattern after treatment with four kinds of DES: Uera, ChCl:Glycerol, ChCl:Xylitol, and ChCl:Ethylene glycol (ChCl: Choline Chloride). The composite materials were also shown to maintain 97.5% of the initial activity of the material even after they were stored at 4 °C for 4 weeks. This demonstrated the great structural stability of the composite. The pH and temperature of the assay were also optimized. The optimal pH for SEH@UiO-66-NH_2 was determined to be 7.0. This pH was 0.5 higher than that of UiO-66-NH_2 which may have been caused by the change of microenvironment during the GA crosslink step. This also matches with the 5 °C higher optimized temperature of SEH@UiO-66-NH_2 than UiO-66-NH_2. The kinetic behavior of SEH@UiO-66-NH_2 and of free SHE followed the Michaelis−Menten model. Due to the change of structure around the active site mentioned above, the apparent V_{max} of SEH@UiO-66-NH_2 was only half that of free SHE. However, the K_m of SEH@UiO-66-NH_2 was one third that of free SHE, implying that the active site has higher affinity to the substrate, leading to overall higher catalytic efficiency (V_{max}/K_m) as 8.0×10^{-3} min^{-1}. Meanwhile, the e.e. value of (R)-1,2-octanediol was also shown to increase form 78.7% (free SEH) to 81.2% (SEH@UiO-66-NH_2) for the same reason.

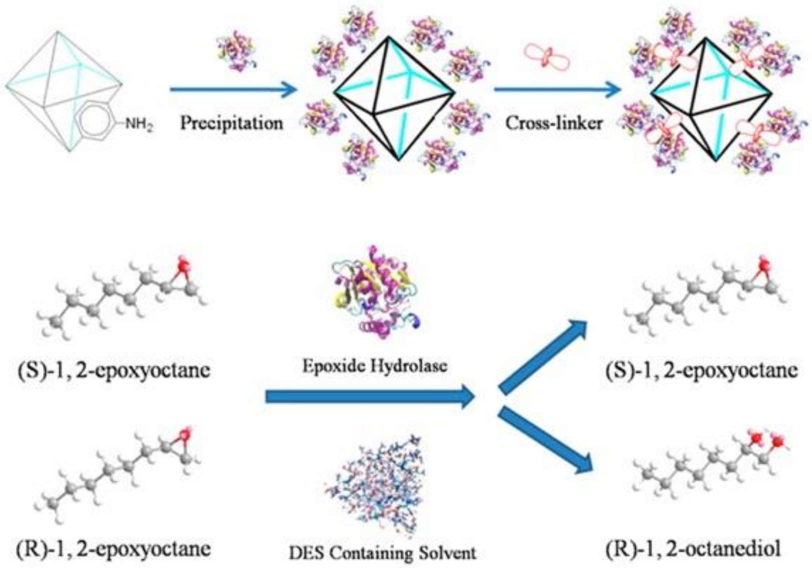

Figure I-11. Schematic Representation of Enzyme attachement to the surface of MOF. Reproduced with permission from *ACS Sustainable Chem. Eng. 2016, 4, 3586-3595.*[83] Copyright 2016 American Chemical Society.

In an example by Liu *et al.*, they synthesized a hemin-MOF (H@M) enzyme mimic composite via surface adsorption for a two-step glucose detection.[84] In this work, MIL-101(Al)-NH_2 and MIL-101(Cr)-NH_2 were synthesized and mixed with hemin in DMF for 12h to form the composites. The analysis of the material by PXRD revealed that after Hemin loading, both of the MOFs transformed into the MIL-53-NH_2 structure. Additionally, both the Fe and Al signals in the energy dispersion spectrum (EDS) along with decrease of BET surface area and new bands associated with hemin at 1604 cm^{-1} (C=N stretching) and 1135 cm^{-1} (C-N stretching) on FT-IR spectra indicate the successful loading of hemin on surface. The catalytic oxidation of chromogenic substrate, TMB, was conducted to demonstrate a peroxidase-like activity of the H@M. In contrast to the deep blue color produced by H@M-TMB-H_2O_2, no color change was observed in the TMB-

H_2O_2. Additionally, the hemin-TMB-H_2O_2 produce negligible color. Chromogenic substrates OPD and ABTS also had similar results, confirming that the peroxidase-like activity existed for H@M. The effects of the pH, temperature, H_2O_2, and TMB concentrations on the system were able to be investigated through UV spectroscopy at an absorption of 642nm. H@M and hemin have a similar optimal pH, around 5.0, while the optimal temperature of H@M was 50 °C. This temperature was 10 °C higher than that of free hemin, indicating an improved thermal stability for the hemin enzyme after immobilization. The reaction followed the Michaelis−Menten model and H@M was shown to have a relatively small K_m, indicating a higher affinity for TMB as opposed to H@M. As a result, a two steps glucose detector was designed. In the detector, glucose was first catalyzed by GOx to form glucose acid in a pH 7.0 buffer solution, producing H_2O_2. Then, TMB was oxidized by the H_2O_2 in presence of H@M at a pH 5.0, displaying a blue color. This method had a linear response for the glucose in the range of 1.0×10^{-5} mol/L to 3.0×10^{-4} mol/L and had a high selectivity towards glucose among fructose, lactose, and maltose.

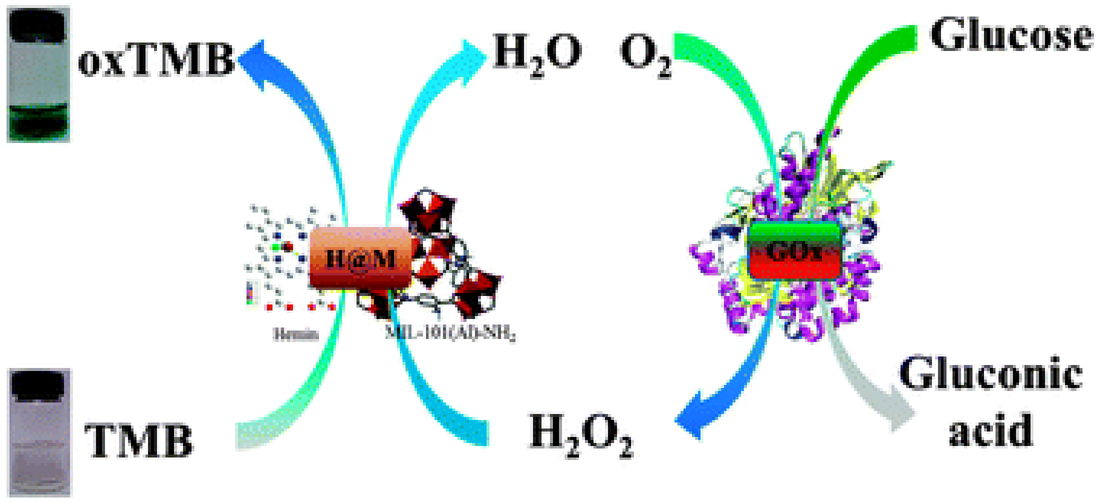

Figure I-12. Schematic illustration of colorimetric determination of glucose using glucose oxidase (GOx) and H@M hybrid material-catalyzed reactions. Reproduced with permission from *Catalysis Science & Technology* 2013, *3*, 2761-2768.[84] Copyright 2013 Royal Society of chemistry.

1.2.3 Metal-organic Frameworks Assisted Synthesis of Metal Nanoparticles

Another MOF based hybrid material is MOF-metal nanoparticles (NPs) composites, which can be used as catalysts. MOFs are a good platform for metal-based catalyst due to their intrinsic metal centers, highly ordered porous structure, uniform pore sizes and environments, high surface areas, and functional organic linkers. The metal nodes of a MOF, such as Cr,[85] Mn,[86] Zr,[87] or Cu,[88-89] can be generated to have open metal sites which can be tuned to become free active sites after thermal removal of coordination solvents or ligands. Theses open metal sites can serve as excellent Lewis acid catalysts.[90] On the other hand, the ligands of the MOF structure can become great metal binding sites by themselves or they can become metal coordination sites after post synthetic modification.[91-92] In this portion, literatures about introducing pre-synthesized NPs into MOFs will not be discussed.[93]

When *in situ* NPs are formed, the synthesis usually occurs in a solution phase. For their synthesis in a MOF, the MOF can be immersed in a solution of the metal salts followed by a reduction via reducing agents, such as $NaBH_4$. During the syntheses, in many cases, the NPs will not only form inside the pores of MOF, but also become attached on the surface of MOF. This may contribute to a resulting limited mass transportation inside of a MOF. The reducing agent will contact with surface metal salts first and flow of mass transportation will bring the NPs on to the surface of MOF.[94] These NPs@MOF materials have been widely applied as catalyst for different reactions, such as ethylene photo-degradation to CO_2 and H_2O,[95] secondary alcohol oxidation,[96] nitrobenzene hydrogenation,[97] generation of H_2 from ammonia borane,[98-100] hydrazine,[101-104]or formic acid,[105-109] and tandem reductive imination of nitroarenes with carbonyl compounds,[110] and etc[90, 111-112]. In this part, emphasis will be put on generation of H_2 from inorganic hydrides.

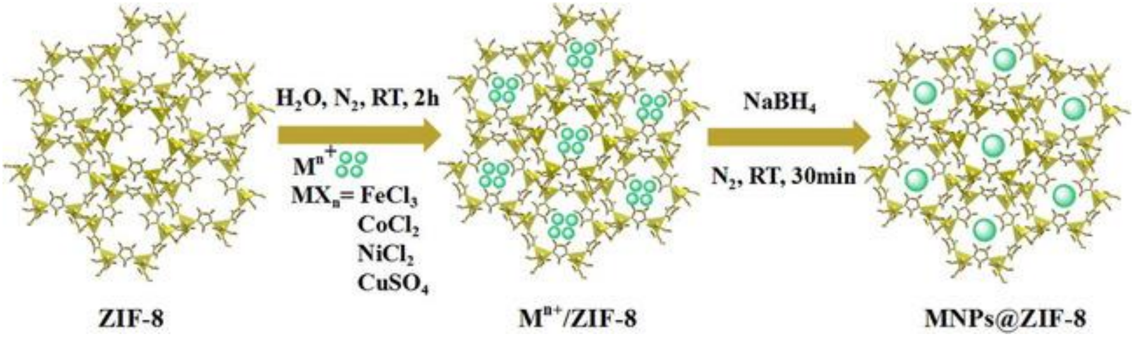

Figure I-13. Synthesis of the nanomaterials NPs@ZIF‐8. Reproduced with permission from *ChemCatChem*, **11**, 1643-1649.[113] Copyright 2019 European Chemical Societies Publishing.

Another example comes from Astruc *et al.* who reported a series of nearly monodispersed alloyed bimetallic NPs@ZIF-8. [114] The catalysts in this study were shown to be much more efficient for H_2 generation than either Ni or Pt NPs alone. The optimized catalyst Ni_2Pt@ZiF-8 achieved a TOF of 600 mol H_2 mol_{catal}^{-1} min^{-1} and 2222 mol H_2 mol_{Pt}^{-1} min^{-1} under ambient conditions. The ZIF-8 support was shown to be a better support for Ni and Pt NPs than graphene oxide, activated carbon, or SBA-15.

Simmilarly to the work conducted by Astruc *et al.*, Liu *et al.* reported the synthesis of SiO_2-encompassed Co@N-doped porous carbon assemblies as a new type of recyclable catalyst for NH_3BH_3 hydrolysis.[115] The catalyst was generated through the calcination of ZIF-67@SiO_2 microtubes at high temperatures under a N_2 atmosphere. It was found that the surface layer of SiO_2 was essential for the production of well-dispersed Co NPs. This was achieved as the surface layer served as an additional surface for Co NPs synthesis. In addition, the SiO_2 layer provided a highly ordered arrangement of Co@N-doped porous carbons within the catalysts. This served to increase the mass transfer of ammonia borane throughout the catalysts. The optimized catalysts were obtained via calcination of the material at 800 ℃ and showed great catalytic performance: a high hydrogen generation rate of 8.4 mol min^{-1} mol_{Co}^{-1}, relatively low activation energy of 36.1 kJ mol^{-1}, and remarkable reusability for at least 10 cycles. In a following study by Kegnæs *et al.* a ZIF-67 structure was utilized as a sacrificial support to prepare N-doped carbon supported Co nanoparticles for NH_3BH_3 hydrolysis.[116] It has been demonstrated that the size of the Co NPs and the structural features of the carbon supports had a large effect on the catalytic activity. The highest catalytic activity was obtained for ZIF-67/8 which had a molar ratio of Co/Zn = 1, which was pyrolysis at 900 ℃. Zn were remove via evaporation at the same time. At room temperature, this catalyst resulted in a TOF of 7.6 mol H_2 mol_{Co}^{-1} min^{-1} and an apparent activation energy of $E_a = 44.9$ kJ mol^{-1}. The turnover frequency was further increased to 12.7 min^{-1} in 0.1 M NaOH. The maximum TOF of 90.1 min^{-1} was achieved with CoNCs@PCC-2a by Zhou *et al.*,[117] which was an excellent result for non-noble metal catalysts.

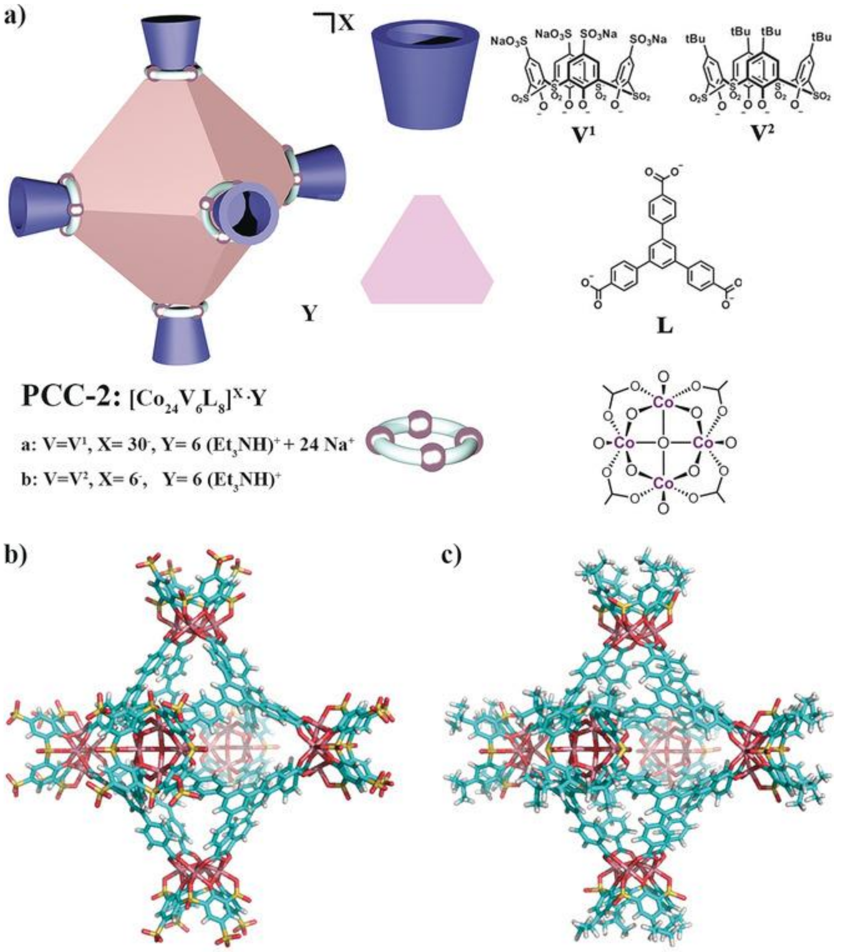

Figure I-14. a) Cartoon of octahedron cage PCC-2 and the cage components, b) crystal structure of PCC-2, and c) crystal structure of PCC-2b. Reproduced with permission from *Angew. Chem. Int. Ed.*, **57**, 5283-5287.[117] Copyright 2018 Wiley.

In another study by Xu *et al.*, a successfully immobilized ultrafine Pt NPs was encapsulated within the pores of MIL-101. This was achieved without aggregation of the

Pt nanoparticles on the external surfaces of framework via a "double solvents" method.[118] The double solvent method was achieved though he suspension of activated MIL-101 in n-hexane which acted as a hydrophobic solvent followed by the dropwise addition of an aqueous $H_2PtCl_6 \cdot 6H_2O$ solution. The samples were further dried and treated in a stream of H_2/He to achieve Pt@MIL-101. The resulting Pt@ MIL-101 composites were shown to possess high catalytic activity in all three phases: liquid-phase ammonia borane hydrolysis (10000 L H_2 mol_{Pt}^{-1} min^{-1}), solid-phase ammonia borane thermal dehydrogenation, and gas-phase CO oxidation.

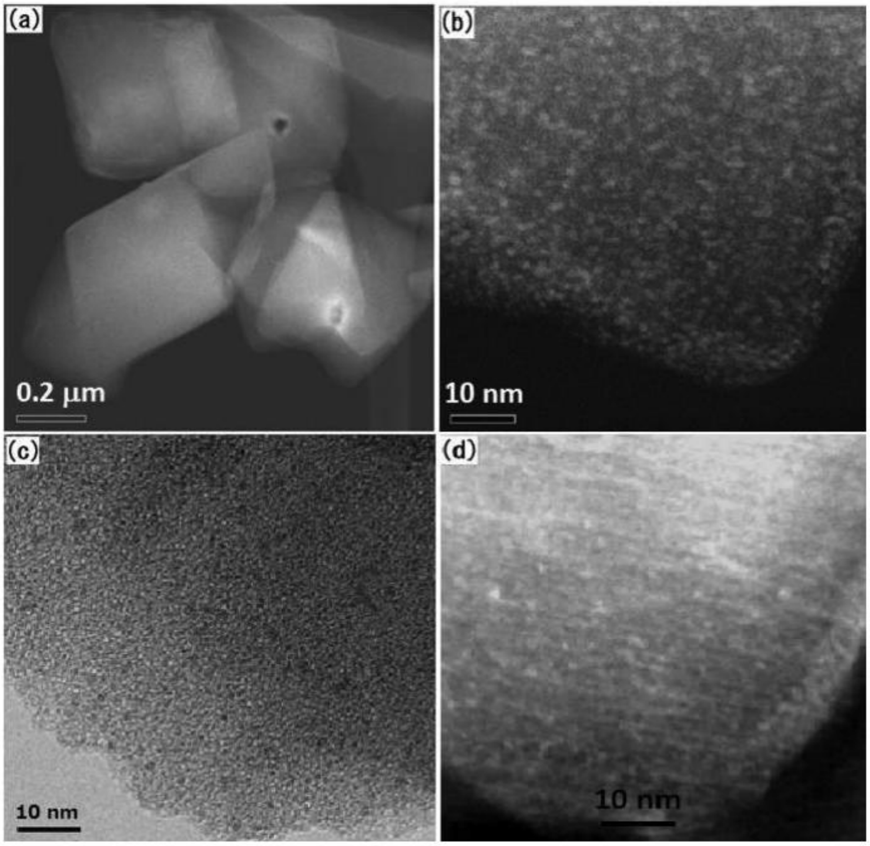

Figure I-15. (a, b) HAADF-STEM, (c) TEM images and (d) reconstructed slice by tomography of 2 wt % Pt@MIL-101. Reproduced with permission from *J. Am. Chem. Soc.*, 2012, **134**, 34, 13926-13929.[118] Copyright 2012 American Chemistry Society.

CHAPTER II

STEPWISE ASSEMBLY OF "TURN-ON" FLUORESCENT SENSORS IN MULTICOMPONENT METAL–ORGANIC FRAMEWORKS FOR IN VITRO CYANIDE DETECTION[*]

2.1 Introduction

The controlled synthesis of multicomponent MOFs allows for the precise placement of multiple corporative functional groups within a framework, leading to emergent synergistic effects. Herein, we demonstrate that "turn-on" fluorescent sensors can be assembled by combining a fluorophore and a recognition moiety within a complex cavity of a multicomponent MOF. An anthracene-based fluorescent linker and a hemicyanine-containing CN^- responsive linker were sequentially installed into the lattice of PCN-700. The selective binding of CN^- to hemicyanine inhibited the energy transfer between the two moieties, resulting in a fluorescence "turn on" effect. Taking advantage of the high tunability of the MOF platform, the ratio between anthracene and the hemicyanine moiety could be fine-tuned in order to maximize the sensitivity of the overall

---

[*] Reprinted with permission from "Stepwise Assembly of Turn-on Fluorescence Sensors in Multicomponent Metal–Organic Frameworks for in Vitro Cyanide Detection." Li, J.; Yuan, S.; Qin, J.-S.; Pang, J.; Zhang, P.; Zhang, Y.; Huang, Y.; Drake, H. F.; Liu, W. R.; Zhou, H.-C. *Angew. Chem. Int. Ed.* doi.org/10.1002/anie.202000702 Copyright 2020 John Wiley and Sons.

framework. The optimized MOF-sensor had a CN^- detection limit of 0.05 μM, which is much lower than traditional CN^- molecular fluorescent sensors (~0.2 μM).

2.2 Background

Metal-organic frameworks (MOFs), a highly crystalline, class of hybrid inorganic-organic materials, has attracted considerable attention in recent years for applications spanning gas storage, gas separation, catalysis, energy harvesting, biomedicine, and chemical sensing.[38, 119-123] These materials are particularly attractive as they contain high inherent porosity, designable structures and tunable physicochemical properties. As a result, MOFs stands out as one of the ideal platforms for the design of chemical sensors.[61] For example, luminescent MOFs have been extensively explored as sensors for metal cations, anions, and organic species.[3] Generally, the analytes interact with the MOF-sensors through host-guest interactions or through energy transfer. The energy level of the lowest unoccupied molecular orbitals (LUMOs) for most analytes generally fall below the LUMOs or conduction bands (CBs) of most MOF materials. Thus, the electron transfer in luminescent MOFs occurs from the MOFs to the guest molecule. As a result, most MOF-based sensors are 'turn-off' type systems, where the fluorescence of the MOF is quenched by the analyte via photoinduced electron or energy transfer.[124] This 'turn-off' fluorescence sensing mechanism ultimately limits the sensitivity of the MOF for chemical sensing. Moreover, molecules with similar electronic properties can exert comparable quenching effects, making it difficult to have high selectivity for a particular analyte. To improve both the sensitivity and selectivity of MOF materials for chemical sensing applications, detections based on a ‘luminescence turn-on’ mechanisms are highly desired.

Molecular ‘turn-on’ sensors can be designed by combining a fluorophore with a recognition moiety.[125-126] Initially, the electron or energy transfer occurs between the fluorophore and the recognition moiety, rendering the molecule non-fluorescent. The analyte triggers an electronic or conformational change of the recognition moiety, altering the intramolecular energy transfer efficiency and resulting in “turn on” florescence type detection. Typically, aromatic molecules with high fluorescence quantum yields (such as anthracene, pyrene, boron dipyrromethene, etc.) are adopted as the fluorophore. The recognition moiety can be judiciously designed to selectively react with a targeted analyte. Cyanide is a well-known toxic substance for human by absorption through skin, lungs, and GI track. It can bind the active site of cytochrome oxidase and inhibit oxygen utilization. Hence, it is important to develop CN^- sensors to ensure physiological safeguard.[127] For CN^- sensors, the sensor-analyte recognition moieties can undergo nucleophilic addition,[128-130] benzil rearrangement,[131] or coordination with metal cations.[132-133] The fluorophore and recognition moiety are usually assembled through covalent bonds in organic synthesis. For instance, a molecular CN^- sensor composed of a CN^- responsive phenylboronic acid moiety and a dimethylamino-styryl-pyridinium-based fluorophore have been reported.[129] In this system, the boronic acid ($R-B(OH)_2$) is able to bind cyanide, forming an electron rich complex ($R-B-(CN)_3$), ultimately restricting non-radiative relaxation pathways and resulting in fluorescence emission enhancement.

However, several limitations exist for the successful design of highly efficient molecular fluorescent 'turn-on' sensors. Many organic fluorophores with large conjugated π-systems are insoluble in water, although aqueous solution is preferred for detection and bioimaging due to the constraints of in vitro applications in cells. Besides, the ratio between fluorophore and recognition moiety is usually fixed in an organic molecule, potentially limiting the sensitivity. Higher sensitivity can be achieved by optimizing the ratio between the fluorophore and recognition moiety. Additionally, chemically combining the fluorophore and recognition moiety into a single molecule often requires judicious design and tedious organic synthesis.

To address these limitations, we propose that MOFs can be a suitable platform for the design of fluorescent 'turn-on' sensors. Instead of connecting fluorophore and recognition groups with covalent bonds, we have demonstrated the feasibility of integrating two moieties by coordination bonds within a MOF generating a multicomponent framework. Recent developments of multicomponent MOFs have demonstrated that multiple functional groups can be engineered into a tuned proximity within the periodic lattice of a MOF.[134-141] The close distance and periodic arrangement of a fluorophore and recognition moiety allows for efficient energy transfer between the two components.[142-144] In addition, the concentration of the fluorophore and recognition moiety can be readily tuned by introducing inert ligand with same length, maximizing the sensitivity. Furthermore, the porous framework structure of the parent scaffold facilitates diffusion of the analyte through the structure. By utilizing a water stable parent MOF[9, 145], the resultant multicomponent MOF product can be readily utilized in aqueous solution;

allowing for a diversification of potential applications as compared to its single molecule equivalent.

Herein, we report a “turn-on” fluorescent sensor generated through the combination of an anthracene-based fluorophore and a hemicyanine-based CN^- responsive moiety in a multi-component MOF (Figure II-1). A stable MOF with coordinatively unsaturated Zr-sites, namely PCN-700, was selected as a matrix in order to generate a multifunctional MOF.[22] The coordinatively unsaturated sites within PCN-700 form two types of pockets, each accommodating only one of two organic linkers, each with different lengths. Two linkers with suitable lengths were designed accordingly, each bearing an anthracene group and a hemicyanine moiety. Sequential installation of the two linkers into the respective pockets in the PCN-700 parent framework was realized through post synthetic modifications. The mild postsynthetic reaction conditions utilized not only ensured the stability of the framework, but also protected chemically labile hemicyanine ligands from decomposition. Hemicyanine tends to decompose in solvothermal conditions required for MOF synthesis. The high tunability of the MOF platform allowed for the control of material composition. The ratio between the anthracene and hemicyanine moieties were tuned to maximize the sensitivity. Additionally, the size of the MOF crystals was reduced to the nanometer scale (500 nm), allowing the in vitro CN^- detection.

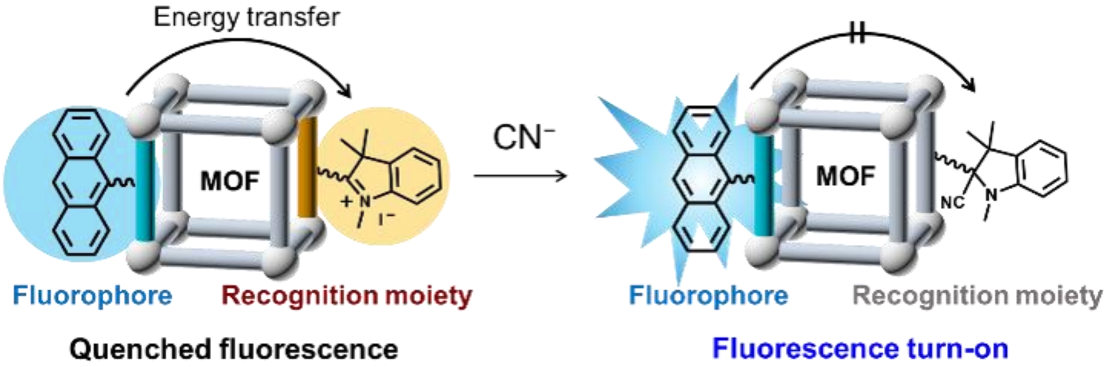

Figure II-1. Schematic representation for the design of a “turn-on” fluorescent sensor in multi-component MOFs by integrating a fluorophore and a recognition moiety. Reprinted with permission from *Angew. Chem. Int. Ed.* doi.org/10.1002/anie.202000702.

2.3 Results and Discussion

The design of a “turn-on” fluorescent sensor was inspired by reported molecular sensors based on the intramolecular charge transfer (ICT) mechanism.[146-149] However, instead of covalently linking the anthracene-fluorophore and hemicyanine, two moieties were connected to Zr clusters separately by coordination bonds within the MOF. It has been demonstrated that efficient ligand to ligand charge transfer exists within mixed-linker MOFs.[142-143] Therefore, we expect that the florescence of the anthracene moieties could be quenched by the hemicyanine linkers within a MOF scaffold. To realize our design, PCN-700 was selected as a platform for this application (Figure II-2a), because of its high chemical stability and capability of accommodating two different linkers post synthetically. A linker bearing anthracene fluorophores was designed, namely L1. Meanwhile, a linker with hemicyanine moiety was synthesized, denoted as L2Hcy. Previous researches have demonstrated that two linkers with lengths similar to L1 and L2Hcy can be simultaneously installed into PCN-700 by insertion into the unsaturated Zr-sites.[22, 139, 150] In this work, however, it was discovered that the two linkers could not be installed simultaneously. This was potentially due to the bulkiness of both linkers. The incorporation of one linker (such as L2Hcy) reduces the pore size of PCN-700 (Figure II-2b) and inhibits the installation of another linker.

In order to successfully synthesize the desired MOF, a stepwise synthetic route was designed. First, L1 was inserted into the large pocket of PCN-700 by reacting the as-synthesized crystals of PCN-700 with L1 in a solution of DMF (Figure II-2c). Subsequently, a hemicyanine precursor with aldehyde functional groups (L2CHO) was installed into PCN-700. Because of the relatively small size of the aldehyde functional groups, L2CHO was successfully inserted into the small pocket, forming PCN-700-L1-L2CHO (Figure II-2d). Finally, a condensation reaction between 1,2,3,3-tetramethyl-3H-indolium iodide and PCN-700-L1-L2CHO was performed, giving rise to the desired product, namely PCN-700-L1-L2Hcy (Figure II-2e). It should be noted that the one pot synthesis of PCN-700-L1-L2Hcy was not successful due to the lability of the hemicyanine moiety. It is hypothesized that this linker may undergo nucleophilic addition or I^- counter ion exchange during the solvothermal synthesis of MOFs.

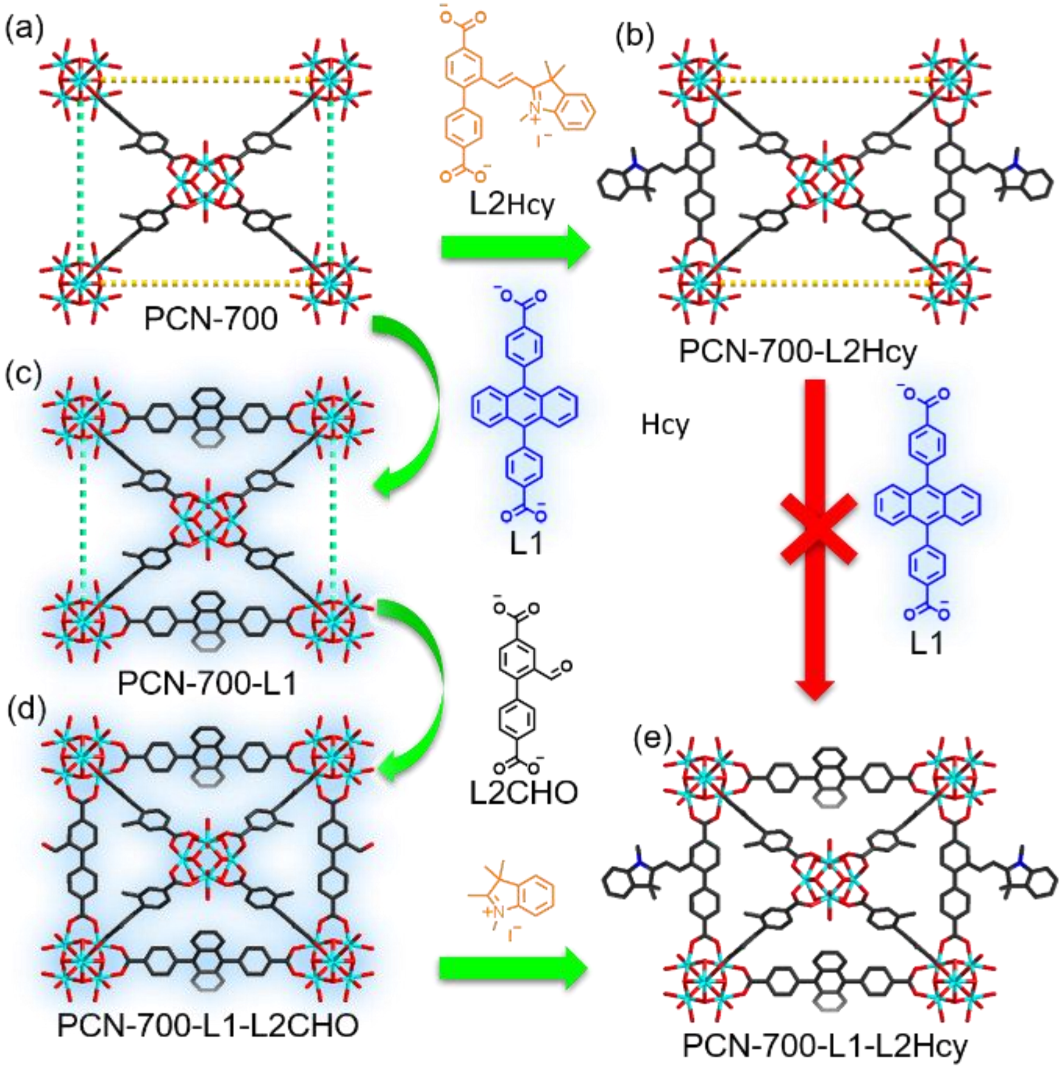

Figure II-2. Synthetic routes of MOFs with anthracene and hemicyanine moieties. Structural representation of PCN-700 (a), PCN-700-L2Hcy (b), PCN-700-L1 (c), PCN-700-L1-L2CHO (d), PCN-700-L1-L2Hcy (e). Reprinted with permission from *Angew. Chem. Int. Ed.* doi.org/10.1002/anie.202000702.

The single crystal to single crystal transformation was realized during the stepwise modification, ensuring that the structure of PCN-700-L1-L2Hcy was unambiguously determined by single-crystal X-ray diffraction. X-ray diffraction studies revealed that PCN-700 crystallized in the tetragonal $P4_2/mmc$ space group. Each Zr6 cluster in the structure is connected to eight original linkers (2,2'- dimethylbiphenyl-4,4'-dicarboxylate), two L1, and two L2Hcy. The anthracene moieties on L1 were clearly observed in the single crystal structure. The biphenyl backbone of L2Hcy could be precisely refined, confirming the successful incorporation of the L2Hcy linker. The disappearance of aldehyde group signal on ^{1}H-NMR spectrum confirmed the 100% conversion from L2 to L2Hcy. The precise refinement of hemicyanine moieties was unsuccessful due to severe disorder. The distance between the L1 and L2Hcy centers was measured to be 14 Å. This is much shorter than the distance allowing for fluorescence resonance energy transfer (FRET, typically in the range of 1–10 nm).[151] The structural transformation of the bulk materials was confirmed by PXRD. The PXRD patterns of PCN-700, PCN-700-L2Hcy, PCN-700-L1, PCN-700-L1-L2CHO, PCN-700-L1-L2Hcy were all matched well with their simulated patterns. The existence of the incorporated L1 and L2Hcy linkers was further verified by ^{1}H-NMR spectroscopy of the digested MOF samples. The ratios between the linkers in the digested MOF samples agreed well with the structural models. The MOFs derived from PCN-700 remained porous, as indicated by N_2 adsorption measurements. When compared to the parent PCN-700 structure, the values of total N_2 uptake and BET surface area for PCN-700-L1, PCN-700-L1-L2CHO, and PCN-700-L1-L2Hcy gradually decreased. (Figure II-3) This experimental result was in agreement with the theorized partially occupied pore space from post synthetic functional group incorporation. The permanent porosity of the material ensures the good contact between the analyte and recognition-centers within MOFs.

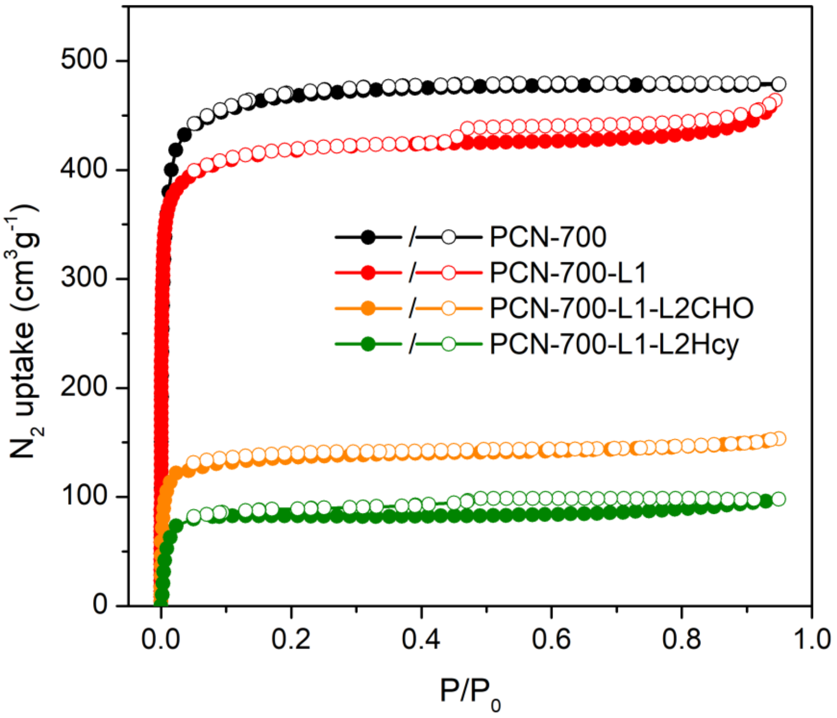

Figure II-3. N_2 adsorption isotherms of PCN-700, PCN-700-L1, PCN-700-L1-L2CHO, and PCN-700-L1-L2Hcy. Reprinted with permission from *Angew. Chem. Int. Ed.* doi.org/10.1002/anie.202000702.

The multi-component MOF scaffold provided a highly tunable platform to optimize the sensing performance of the material. Confocal fluorescence microscopy imaging showed that PCN-700 is weakly fluorescent. However, the fluorescence intensity is dramatically enhanced when the anthracene-based L1 linker was introduced into the structure (Figure II-4). The incorporation of L2Hcy quenched the fluorescence of the MOF. The occupancy of L1 and L2Hcy in PCN-700 can be fine-tuned from 0 to 100% by partially replacing L1 or L2Hcy with nonfunctionalized linkers of the same length during the synthesis. The correlation of the linker ratio in the starting materials and MOF products was plotted (Figure II-5). The effect of the concentration of L1 and L2Hcy in the structure on the fluorescence intensity was also investigated to optimize the linker ratio (Figure II-6). When the L1 occupancy was fixed at 100%, the fluorescence intensity was quickly reduced upon the addition of L2Hcy and then leveled off to a steady state. In fact, 95% quenching was observed when only 50% of L2Hcy ligand was incorporated. On the contrary, the L1 content had a limited effect on the intensity when 100% of the L2Hcy linker was present. The effective quenching of L1 by L2Hcy highlights the efficient energy transfer between the two ligands confined within the MOF cavity. For comparison, no obvious quenching was observed when L1 and L2Hcy co-existed in solution prior to incorporation into a MOF (Figure II-7). The relative intensity at different CN^- concentrations, compared with PCN-700-L1, was measured for the MOF probes with various L2 concentrations (L1 fixed to 100%). The sample with a L2Hcy ratio of 75% (denoted as PCN-700-L1-L2Hcy-75%) exhibited the highest sensitivity within a wide range of CN^- concentration (Figure II-8). The CN^- dependent fluorescence spectra were measured by incubating a MOF suspension in aqueous solutions of CN^- for 1 min. The as-synthesized PCN-700-L1-L2Hcy-75% suspension did not show obvious florescence. Upon the addition of CN^-, the emission at 435 nm sharply increase, owing to the recovered emission of the anthracene linkers in the structure (Figure II-9). The recovery of the florescence in the MOF occurred almost completely within 1 min after the addition of CN^-. This indicated the facile diffusion of CN^- with-in the porous framework, easily reaching the hemicyanine centers. The fluorescence intensity was linearly related to the concentration of CN^- within the range of 0 to 2.67 μM (Figure II-10). The CN^- detection limit was determined to be 0.05 μM, which is much lower than traditional CN^- molecular fluorescent sensors (~0.2 μM)[124, 146, 152] and the permissible level of CN^- according to the world health organization (WHO) for drinking water (1.9 μM).[146] Moreover, PCN-700-L1-L2Hcy-75% possessed high selectivity toward the CN^- over the other competitive anions including F^-, Cl^-, Br^-, I^-, CO_3^{2-}, HCO_3^-, SO_4^{2-}, HSO_4^-, NO_3^-, $HCOO^-$, AcO^-, and SCN^-. Therefore, PCN-700-L1-L2Hcy-75% was shown to be useful as a highly sensitive and selective fluorescent probe for CN^- detection in drinking water. (Figure II-11)

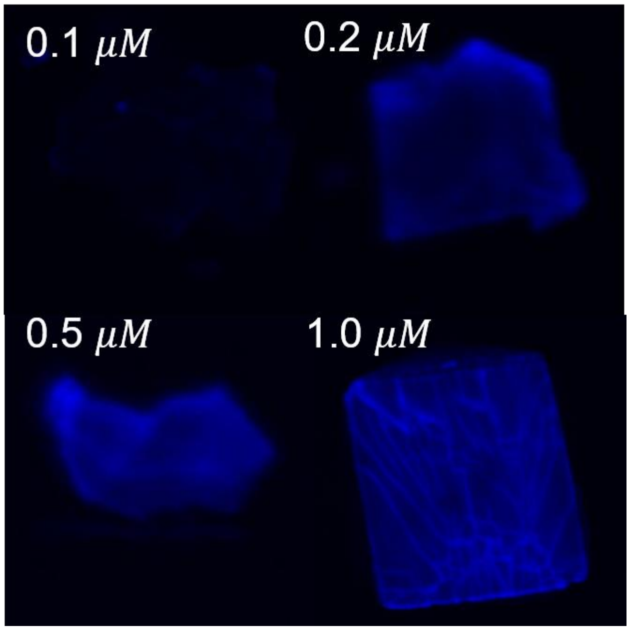

Figure II-4. Confocal fluorescence microscope images of PCN-700-L1-L2Hcy-75% treated by 0.1, 0.2, 0.5, 1.0 μM of CN^- solution respectively. Reprinted with permission from *Angew. Chem. Int. Ed.* doi.org/10.1002/anie.202000702.

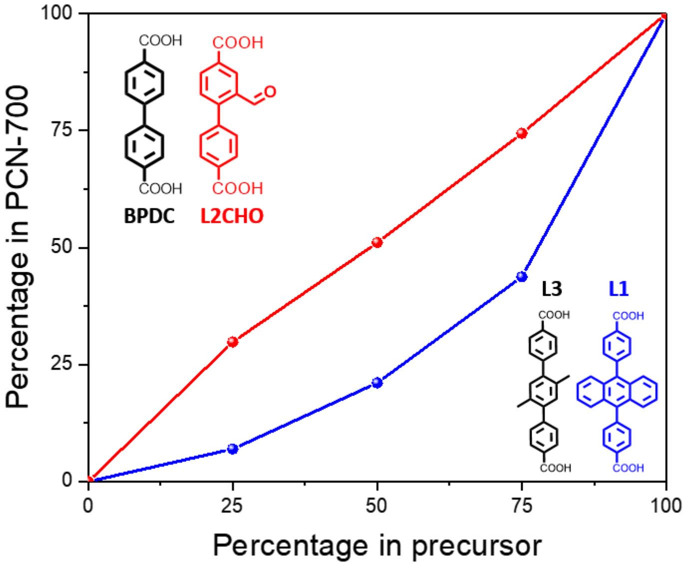

Figure II-5. Correlation of linker ratio in starting materials and MOF products. Reprinted with permission from *Angew. Chem. Int. Ed.* doi.org/10.1002/anie.202000702.

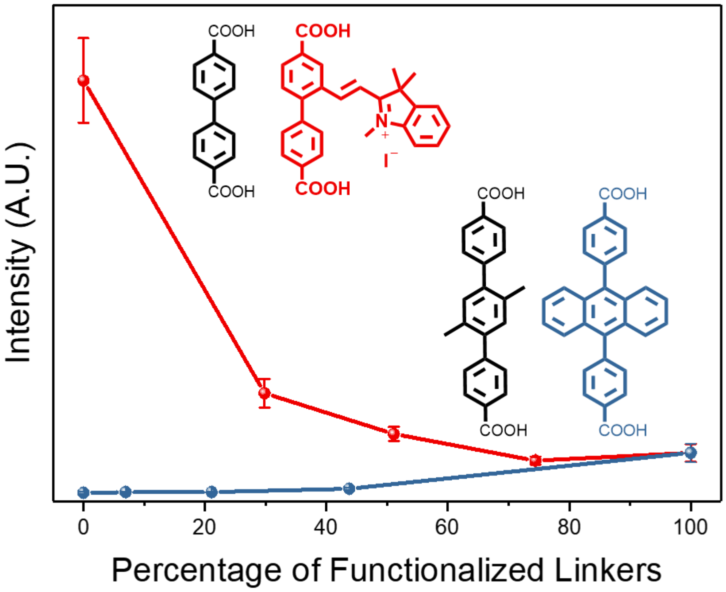

Figure II-6. Fluorescence intensity of MOFs as a function of L1 ratio (L2Hcy fixed to 100%, Blue line) and L2Hcy ratio (L1 fixed to 100%, Red line). (Same mole of PCN-700 was used for each spot). Reprinted with permission from *Angew. Chem. Int. Ed.* doi.org/10.1002/anie.202000702.

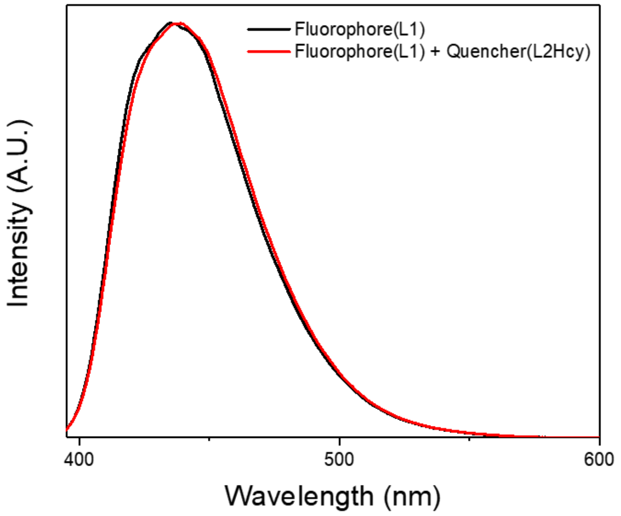

Figure II-7. Fluorescent spectrum of L1 and L1, L2Hcy 1:1 mixed solution (DMF). Intensity remains almost the same indicating unsuccessful quenching by simply mix the fluorophore and quencher in solution. Concerntration of L1 and L2Hcy are $\mathbf{3.0} \times \mathbf{10^{-3}}\ \boldsymbol{mmol}$. Reprinted with permission from *Angew. Chem. Int. Ed.* doi.org/10.1002/anie.202000702.

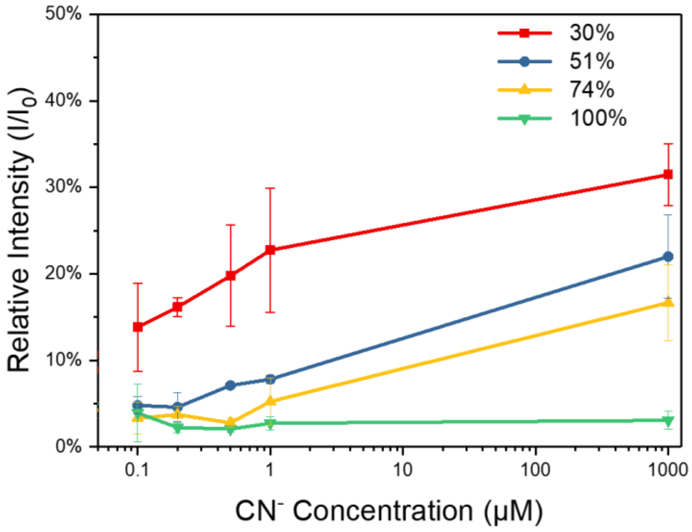

Figure II-8. Signal to noise ratio of samples with various L2Hcy ratio (L1 fixed to 100%) treated by different concentration of CN^{-} solution. Reprinted with permission from *Angew. Chem. Int. Ed.* doi.org/10.1002/anie.202000702.

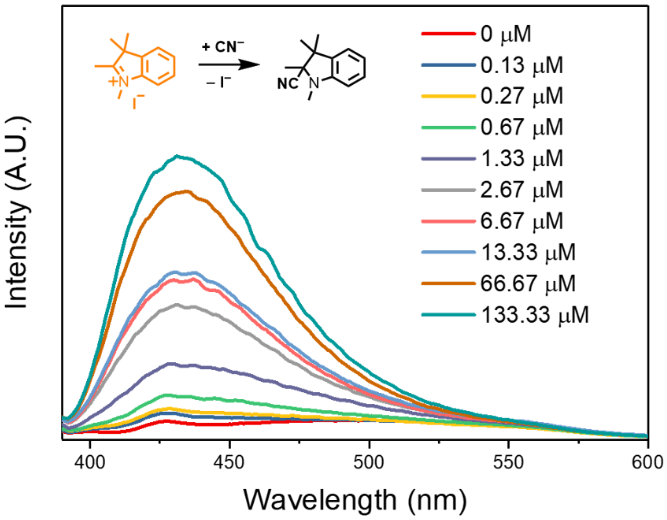

Figure II-9. FL spectra of PCN-700-L1-L2Hcy-75% probe (100 μg) in the presence of various concentrations of CN^- in water (ex= 375 nm, spectrum is recorded 1 min after CN^- addition). Reprinted with permission from *Angew. Chem. Int. Ed.* doi.org/10.1002/anie.202000702.

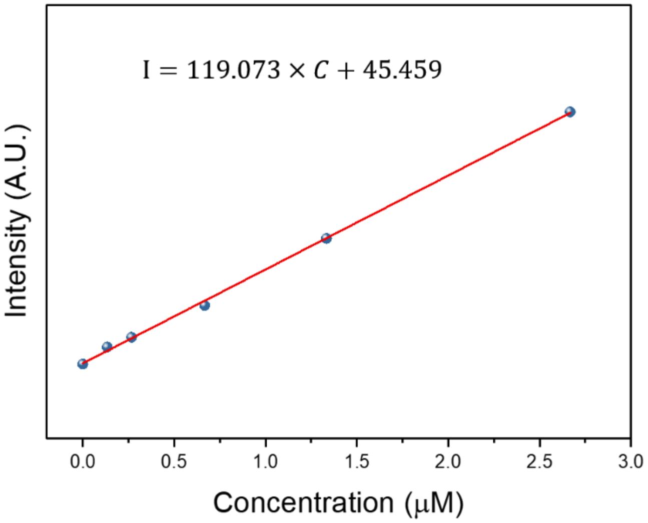

Figure II-10. Correlation between fluorescence intensity and CN^- concentration. Reprinted with permission from *Angew. Chem. Int. Ed.* doi.org/10.1002/anie.202000702.

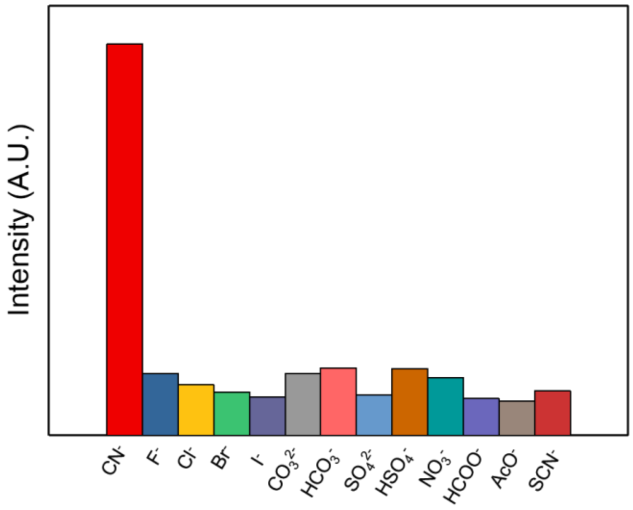

Figure II-11. Selectivity towards different anions (2.67 *μ*M). Reprinted with permission from *Angew. Chem. Int. Ed.* doi.org/10.1002/anie.202000702.

The particle size of the MOF-based probe was controlled by tuning the synthetic conditions. PCN-700-L1-L2Hcy-75% nanoparticles with an average diameter of 500 nm were successfully synthesized by diluting the MOF precursor in the solvothermal synthesis. (Figure II-12) PXRD patterns of PCN-700-L1-L2Hcy-75% nanoparticles showed the same structure as the single crystalline samples, although peak broadening in the PXRD was observed. (Figure II-13) The nanoparticle size of the MOF probes enhanced the cell permeability, allowing for in vitro CN^- detection. The confocal fluorescence image of HeLa cells with/without MOF probes showed almost none fluorescence (Figure II-14a-d), whereas upon incubation with NaCN (1 μM) a strong "turn-on" florescence was observed (Figure II-14e,f). These observations demonstrate the good cell-membrane permeability of the MOF nanoparticles, extending the application of these MOF probes to CN^- detection and bioimaging in living cells.

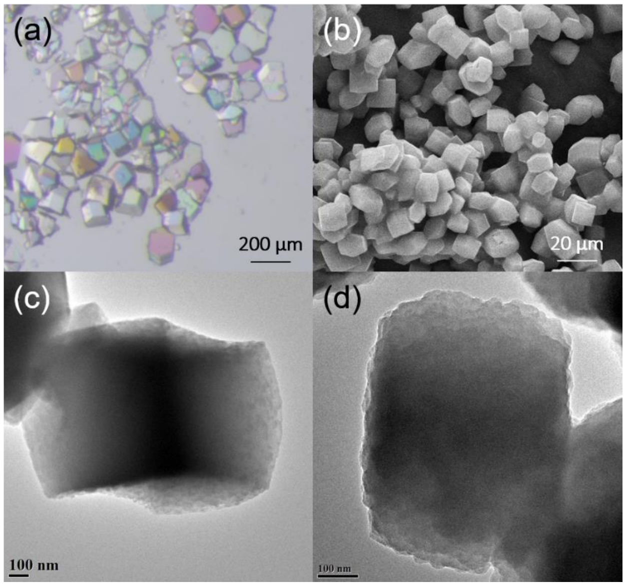

Figure II-12. (a) Optical image of PCN-700 single crystals, (b) SEM image of PCN-700 single crystals, (c) TEM image of nano PCN-700-L1 (500 nm), (d)TEM image of nano PCN-700-L1 (700 nm). Reprinted with permission from *Angew. Chem. Int. Ed.* doi.org/10.1002/anie.202000702.

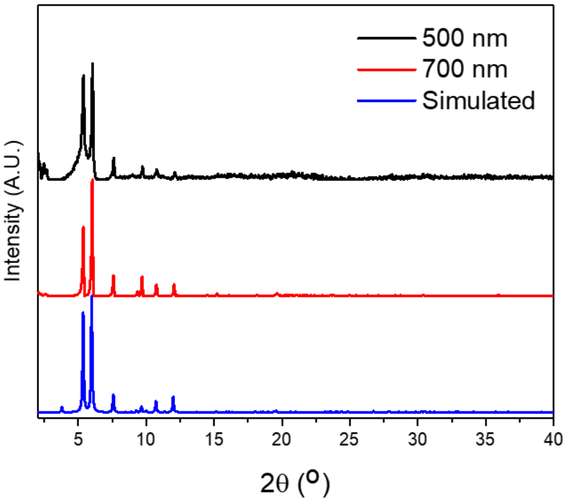

Figure II-13. PXRD pattern of different size of nano PCN-700-L1 and simulated one. Reprinted with permission from *Angew. Chem. Int. Ed.* doi.org/10.1002/anie.202000702.

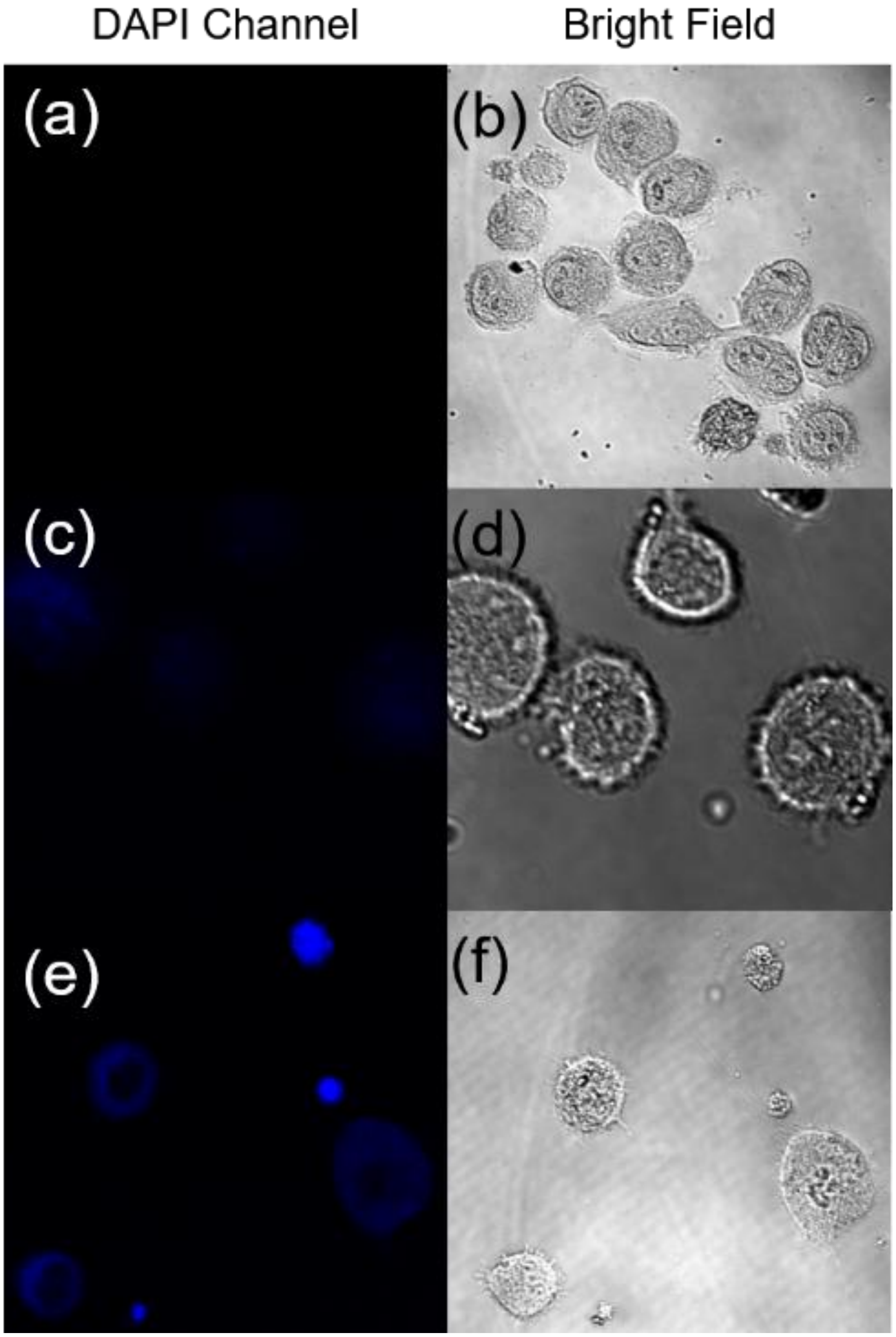

Figure II-14. Confocal fluorescence images of (a) HeLa cells, (c) HeLa cells with PCN-700-L1-L2Hcy-75% probe (100 μg), (e) HeLa cells incubated with 100 μg probe and 1 μM NaCN for 30 min at 37 ◦C. (b), (d), (f) are bright field images of (a), (c), (e), respectively. Reprinted with permission from *Angew. Chem. Int. Ed.* doi.org/10.1002/anie.202000702.

2.4 Conclusion

In conclusion, the integration of an anthracene-based fluorophore and a hemicyanine-based CN^- responsive moiety within a multicomponent MOF successfully generated a highly selective and sensitive “turn-on” fluorescent sensor. Efficient energy transfer between the fluorophore and the recognition moiety was able to be accomplished through the close proximity of the two components within a periodic lattice. When compared to the molecular probe equivalent, the MOF-based probe allowed for the optimization of the analyte sensitivity by tuning the ratio between the fluorophore and the recognition moiety. The optimized MOF-probe was shown to have a CN^- detection limit as low as 0.05 μM, demonstrating its feasibility for CN^- detection in drinking water. In addition, the size of the MOF particles could be tuned to the nanometer scale, extending the application of this material into in vitro CN^- detection. This work also highlights the capability of MOFs for applications in the assembly of energy-transfer based sensors. Furthermore, the findings presented here could be applied to the integration of multiple cooperative moieties within MOFs, helping to inspire the design of new hybrid materials.

2.5 Instrumentation and Methods

2.5.1 Materials and Instrumentation

All reagents and solvents used in these synthetic studies were commercially available and used as supplied without further purification. ^1H NMR spectra were obtained on a Mercury 500 MHz spectrometer. Single crystal X-ray diffraction experiments were carried out on a SuperNova diffractometer equipped with Cu-Kα radiation ($\lambda = 1.5418$ Å) and a Bruker D8-Venture diffractometer equipped with a Cu microfocus tube (λ = 1.54178 Å). Powder X-ray diffraction (PXRD) was carried out with a Bruker D8-Focus Bragg-Brentano X-ray powder diffractometer equipped with a Cu microfocus tube (λ = 1.54178 Å) at 40 kV and 40 mA. Gas sorption measurements were conducted on a Micromeritics ASAP 2020 system. TEM experiments were conducted on a FEI Tecnai G2 F20 ST microscope (America) operated at 200 kV. SEM experiments were conducted on a Quanta 600 FEG field emission scanning electron microscope. Confocal Microscope experiments were conducted on an Olympus FV1000 confocal microscope. Optical images were taken by ZEISS SteREO Discovery.V12 microscope. HeLa (ATCC CCL-2) were grown in DMEM supplemented with FBS and P/S and kept at 37 ℃ in a humidified atmosphere containing 5% CO_2. Photon fluorescence spectrum were taken on Shimadzu RF-5301 PC spectrofluorophotometer. HeLa (ATCC CCL-2) were grown in DMEM supplemented with FBS and P/S and kept at 37 ℃ in a humidified atmosphere containing 5% CO_2. HeLa cells were seeded in a cell culture dish and allowed to grow for 24-48 h. Then the culture media was replaced by fresh DMEM containing 1 μM CN^- at 37 ℃ for 4 h in darkness. Culture media was removed and the cells were washed with fresh FBS for 3 times before being subjected to microscope. The fluorescence signal was collected in DAPI channel (420 nm to 450 nm) under 405 nm laser excitation.

2.5.2 Ligand and MOF Synthesis

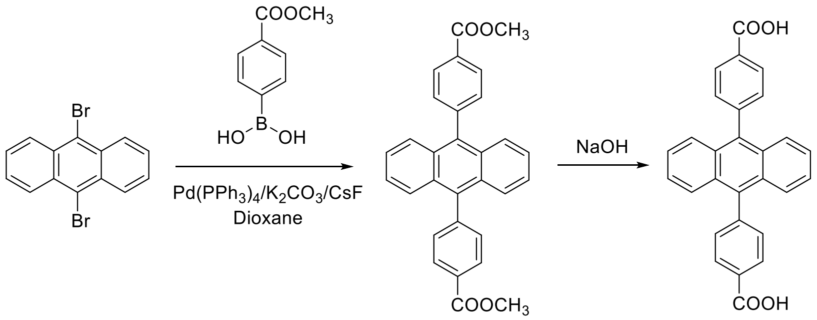

Figure II-15. Synthesis of L1. Reprinted with permission from *Angew. Chem. Int. Ed.* doi.org/10.1002/anie.202000702.

Synthesis of 4,4′-(anthracene-9,10-diyl)dibenzoic acid (L1). 9,10-Dibromoanthracene (2.85 g, 8.5 mmol), 4-(methoxycarbonyl)phenylboronic acid (3.8 g, 21.2 mmol), K_2CO_3 (4.2 g, 30 mmol), CsF (2.5 g, 16.4 mmol), and catalyst [$Pd(PPh_3)_4$] (1.0 g, 0.86 mmol) were dissolved in dioxane (150 mL) under argon in 250 ml three necked flask. The mixture was stirred at 120 °C for 24 h. Dichloromethane (100 mL) and water (50 mL) were added, the organic layer was separated, and the aqueous layer was extracted with dichloromethane (3×20 mL). The combined organic layers were washed with brine (200 mL), dried over anhydrous Na_2SO_4, and filtered. The solvent was removed under reduced pressure and the residue was purified by passing through a silica plug with dichloromethane/petroleum ether (1:1) as the eluent to give a light-yellow solid. The solid was mixed with NaOH solution (0.1 M, 150 ml) and refluxed at 100 ℃ for 12 h. The resulting solution was cooled to room temperature and tuned to pH 5 by HCl. The light yellow precipitate was filtered and dried. (2.12 g, 4.72 mmol, 52.0 %). ^{1}H NMR (400 MHz, DMSO): 7.43 (m, 4H), 7.49 (m, 4H), 7.57 (d, 4H), 8.18 (d, 4H) ppm.[153]

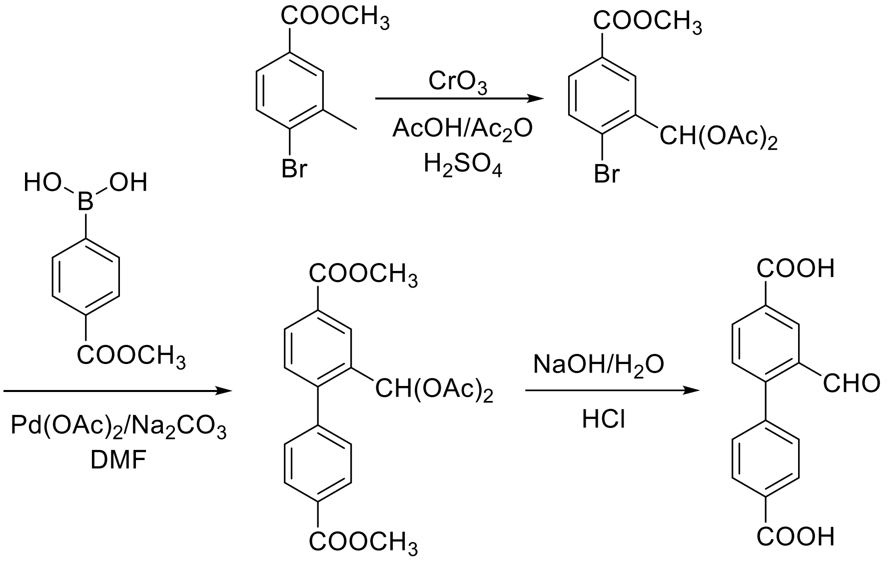

Figure II-16. Synthesis of L2CHO. Reprinted with permission from *Angew. Chem. Int. Ed.* doi.org/10.1002/anie.202000702.

Synthesis of 2-formyl-biphenyl-4,4′-dicarboxylic acid (L2CHO).

(i) Synthesis of 4-bromo-3-diacetoxymethyl-benzoic acid methyl ester

CrO_3 (6.00 g, 60 mmol) was added in portions over 30 min to 4-bromo-3-methyl-benzoic acid methyl ester (4.60 g, 20 mmol) dissolved in AcOH (33 ml) and Ac_2O (34 ml) containing H_2SO_4 (5 ml) cooled on an ice-bath. The mixture was stirred for another hour as the ice bath expired. The reaction mixture was poured into chilled water (300 ml) and stirred vigorously for 20 min before collecting the precipitated solid by filtration and washing with water (3 × 20 ml). (4.58 g, 60 %). ^{1}H NMR (400 MHz; CDCl3): 2.16 (s, 6H), 3.94 (s, 3H), 7.68 (d, 1H), 7.90 (dd, 1H), 7.92 (s, 1H), 8.20 (d, 1H).

(ii) Synthesis of 2-diacetoxymethyl-biphenyl-4,4'-dicarboxylic acid methyl ester

DMF (30 ml) and then 2 M Na_2CO_3 (13.5 ml, 27 mmol) were added by syringe to 4-bromo-3-formyl-benzoic acid methyl ester (3.10 g, 9 mmol), 4-carboxyphenylboronic acid (1.86 g, 11 mmol), and $[Pd(OAc)_2]$ (0.42 g, 4 mol%) while stirring under an atmosphere of N_2. The mixture was heated at 90 ℃ overnight and then cooled, filtered over Celite and the filter pad washed with H_2O (50 ml). The combined filtrates were acidified to a pH of 5 by HCl to precipitate a solid which was collected by filtration, washed with H_2O and oven dried (85 ℃). The solid was crystallized from EtOH/DMF/H2O to give the product as a white solid. (1.50 g, 62 %). ^1H NMR (400 MHz; DMSO-d6): 2.16 (s, 6H), 3.94 (s, 6H), 7.61 (dd, 2 H), 7.65 (d, 1 H), 7.92(s, 1H), 8.06 (dd, 2 H), 8.25 (dd, 1 H), 8.45 (d, 1 H)

(iii) Synthesis of 2-formyl-biphenyl-4,4'-dicarboxylic acid

2-diacetoxymethyl-biphenyl-4,4'-dicarboxylic acid methyl ester (1.50 g) was mixed with 1 M NaOH solution (150 ml) and heated to reflux at 100 ℃ for overnight. The cooled solution was acidified with HCl to precipitate a solid which was collected by filtration, washed with H_2O and oven dried (85 ℃). ^1H NMR (400 MHz; DMSO-d6): 7.61 (dd, 2 H), 7.65 (d, 1 H), 8.06 (dd, 2 H), 8.25 (dd, 1 H), 8.45 (d, 1 H), 9.91 (s, 1 H).[154]

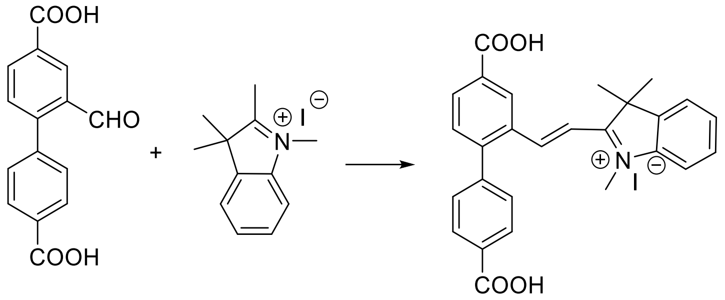

Figure II-17. Synthesis of L2Hcy. Reprinted with permission from *Angew. Chem. Int. Ed.* doi.org/10.1002/anie.202000702.

Synthesis of L2Hcy. Compound L2CHO (0.54 g, 2 mmol), 1,2,3,3-Tetramethyl-3H-indolium iodide (0.6 g, 2 mmol) were added to a 250-mL Schlenk flask containing 80 ml of ethanol charged with a stir bar. The reaction mixture was heated to reflux for 12 h. The ethanol was removed by rotary evaporation and L2Hcy was obtained as an orange solid. ^{1}H NMR (300 MHz, $CDCl_3$): 1.74 (s, 6H), 4.16 (s, 3H), 7.60 (m, 2H), 7.76 (d, 1H), 7.89 (m, 3H), 8.02 (m, 3H), 8.29 (d, 2H), 8.39 (d, 2H) ppm.

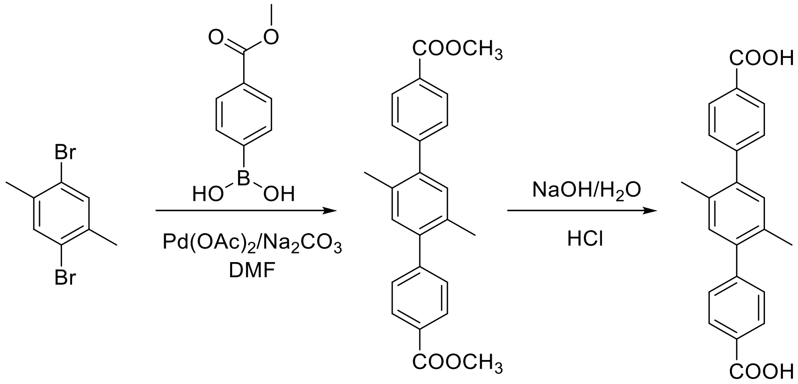

Figure II-18. Synthesis of L3. Reprinted with permission from *Angew. Chem. Int. Ed.* doi.org/10.1002/anie.202000702.

Synthesis of 2′,5′-dimethyl-[1,1′:4′,1′′-terphenyl]-4,4′′-dicarboxylic acid (L3). 1,4-dibromo-2,5-dimethylbenzene (2.24 g, 8.5 mmol), 4-(methoxycarbonyl)phenylboronic acid (3.8 g, 21.2 mmol), K_2CO_3 (4.2 g, 30 mmol), CsF (2.5 g, 16.4 mmol), and catalyst [Pd(PPh3)4] (1.0 g, 0.86 mmol) were dissolved in a mixed solvent of dioxane (100 mL) under argon in an autoclave. The mixture was stirred at 120 °C for 24 h. The reaction was quenched by adding water. Dichloromethane (100 mL) and water (50 mL) were added, the organic layer was separated, and the aqueous layer was extracted with dichloromethane (3×20 mL). The combined organic layers were washed with brine (200 mL), dried over anhydrous Na_2SO_4, and filtered. The solvent was removed under reduced pressure and the residue was purified by passing through a silica plug with dichloromethane/petroleum ether (1:1) as the eluent to give a white solid (1.63 g, 4.72 mmol, 13.0 %). ^{1}H NMR (400 MHz, DMSO-d6): 2.19 (s, 6H), 7.14 (s, 2H), 7.47 (d, 4H), 7.96 (d, 4H).[153]

Synthesis of PCN-700 single crystals. $ZrCl_4$ (200 mg), 2,2′-dimethylbiphenyl-4,4′-dicarboxylate (H_2Me_2-BPDC, 100 mg), trifluoroacetic acid (1.0 ml) and DMF (20 mL) were charged in a Pyrex vial. The mixture was heated in 120 ℃ oven for 72 h. After cooling down to room temperature, the colorless crystals of PCN-700 were harvested.

Synthesis of PCN-700-L1 single crystals. Crystals of PCN-700 (5 mg), L1 (12.5 µmol) and DMF (4 mL) were charged in a Pyrex vial. The mixture was heated in 80 ℃ oven for 12 h. The crystals were washed by DMF for 3 times to yield PCN-700-L1. The synthesis of PCN-700-L1(50%) is similar to that of PCN-700-L1 except that L1 (6.25 μmol) and L1′ (6.25 μmol) are used instead of L1 (12.5 μmol).

Synthesis of PCN-700-L1-L2CHO single crystals. PCN-700-L1 (5 mg), L2CHO (0.0125 mmol) and DMF (4 mL) were charged in a Pyrex vial. The mixture was heated in 80 ℃ oven for 12 h. The crystals were washed by DMF for 3 times to yield PCN-700-L1-L2CHO. The synthesis of PCN-700-L1-L2CHO (50%) is similar to that of PCN-700-L1 except that L2CHO (6.25 μmol) and biphenyl-4,4′-dicarboxylic acid (H_2BPDC, 0.000625 mmol) (6.25 μmol) are used instead of L2CHO (12.5 μmol).

Synthesis of PCN-700-L1-L2Hcy single crystals. PCN-700-L1-L2CHO (5 mg), 1,2,3,3-tetramethyl-3H-indolium iodide (0.05mmol) and ethanol (4 mL) were charged in a Pyrex vial. The mixture was heated in 60 ℃ oven for 12 h. The crystals were washed by ethanol for 3 times followed by DMF for 3 times to yield PCN-700-L1-L2Hcy. The yield is ~99% as confirmed by ^1H NMR of digested PCN-700-L1-L2Hcy.

Synthesis of PCN-700-L1 nano-crystals. $ZrCl_4$ (30 mg), H_2Me_4-BPDC (10 mg), L1 (5 mg), trifluoroacetic acid (0.1 ml) and DMF (20 mL) were charged in a Pyrex vial. The mixture was heated in 120 ℃ oven for 12 h. After cooling down to room temperature, the white powder of nano PCN-700-L1 were harvested.

Synthesis of PCN-700-L1-L2CHO nano-crystals. The synthesis of PCN-700-L1-L2CHO nano-crystals is similar to the synthesis of single crystalline samples except that PCN-700-L1 nano-crystals are used as starting materials.

Synthesis of PCN-700-L1-L2Hcy nano-crystals. The synthesis of PCN-700-L1-L2Hcy nano-crystals is similar to the synthesis of single crystalline samples except that PCN-700-L1-L2CHO nano-crystals are used as starting materials.

2.5.3 Single-crystal X-ray Crystallography

The crystals of PCN-700-L1-L2Hcy were taken from the mother liquid without further treatment, transferred to oil, and mounted onto a loop for single crystal X-ray data collection. The diffraction was measured on a Bruker Smart Apex diffractometer equipped with Cu-Kα radiation ($\lambda = 1.5418$ Å) and a low temperature device (100 K). The structures were solved by direct methods using *SHELXS* and refined by full-matrix least-squares on F^2 using *SHELXL* software.[155] All non-hydrogen atoms were refined with anisotropic displacement parameters. The hydrogen atoms on the aromatic rings were located at geometrically calculated positions and refined by riding. The free solvent molecules are highly disordered in MOFs, and attempts to locate and refine the solvent peaks were unsuccessful. The attempts to locate and refine the hemicyanine moiety attaching on the L2 ligand were unsuccessful due to the high level of disorder. The diffused electron densities resulting from these solvent molecules were removed using the SQREEZE routine of PLATON[156]; structures were then refined again using the data generated. Crystal data are summarized in Table S1. CCDC number for PCN-700-L1-L2Hcy: 1990516.

Table II-1. Crystal data and structure refinements for PCN-700-L1-L2Hcy.

Name	PCN-700-L1-L2Hcy
Formula	$C_{212}H_{144}O_{64}Zr_{12}$ $Zr_6O_4(OH)_4(Me_2\text{-BPDC})_4(L1)_2(L2)_2$
Formula weight	4809.90
Shape/Color	Blocky/yellow
Crystal System	Tetragonal
Space Group	$P4_2/mmc$
a (Å)	23.1982(11)
b (Å)	23.1982
c (Å)	18.9071(9)
α (°)	90.000
β (°)	90.000
γ (°)	90.000
V (Å^3)	10175.0(11)
Z	1
T (K)	100(2)
$d_{\text{calcd.}}$ (g/cm^3)	0.785
μ(mm^{-1})	2.774
F(000)	2408.0
Radiation	CuKα (λ = 1.54184)
2Θ range for data collection/°	7.622 to 137.376

Index ranges	$-20 \le h \le 27$, $-18 \le k \le 26$, $-21 \le l \le 22$
Reflections collected	45263
Independent reflections	5069 [R_{int} = 0.0889, R_{sigma} = 0.0416]
Data/restraints/parameters	5069/3/137
Goodness-of-fit on F^2	1.129
Final R indexes [I>=2σ (I)]	R_1 = 0.0930, wR_2 = 0.2626
Final R indexes [all data]	R_1 = 0.1055, wR_2 = 0.2799
Largest diff. peak/hole / e Å^{-3}	2.98/-2.06

2.5.4 N_2 Sorption Isotherms

N_2 adsorption measurements were performed using a Micromeritics ASAP 2020 surface area and pore size analyzer. Before sorption experiments, as-synthesized samples were washed with DMF several times to remove unreacted starting ligands and inorganic species. Afterwards, the crystals were carefully decanted and washed with DMF and acetone several times. Then, the samples of PCN-700, PCN-700-L1, PCN-700-L1-L2CHO, and PCN-700-L1-L2Hcy were activated under vacuum at 80 °C for 10 h after acetone exchange. Low-pressure N_2 adsorption isotherms were measured at 77 K in a liquid nitrogen bath. The specific surface areas were determined using the Brunauer-Emmett-Teller model from the N_2 sorption data.

2.5.5 ^{1}H-NMR Spectroscopy

For ^{1}H NMR spectroscopy, the dry MOF sample (around 5 mg) was digested by a few drop of concentrated D_2SO_4-d_2 in a 4 mL vial. About 0.5 mL DMSO-d_6 was added to the vial and the mixture was sonicated for 5 minutes for NMR measurement. ^{1}H NMR spectra for PCN-700, L1, L3, L2CHO, H2BPDC, PCN-700-L1-7%, PCN-700-L1-20%, PCN-700-L1-43%, PCN-700-L2CHO-30%, PCN-700-L2CHO-50%, PCN-700-L2CHO-75% are presented collected.

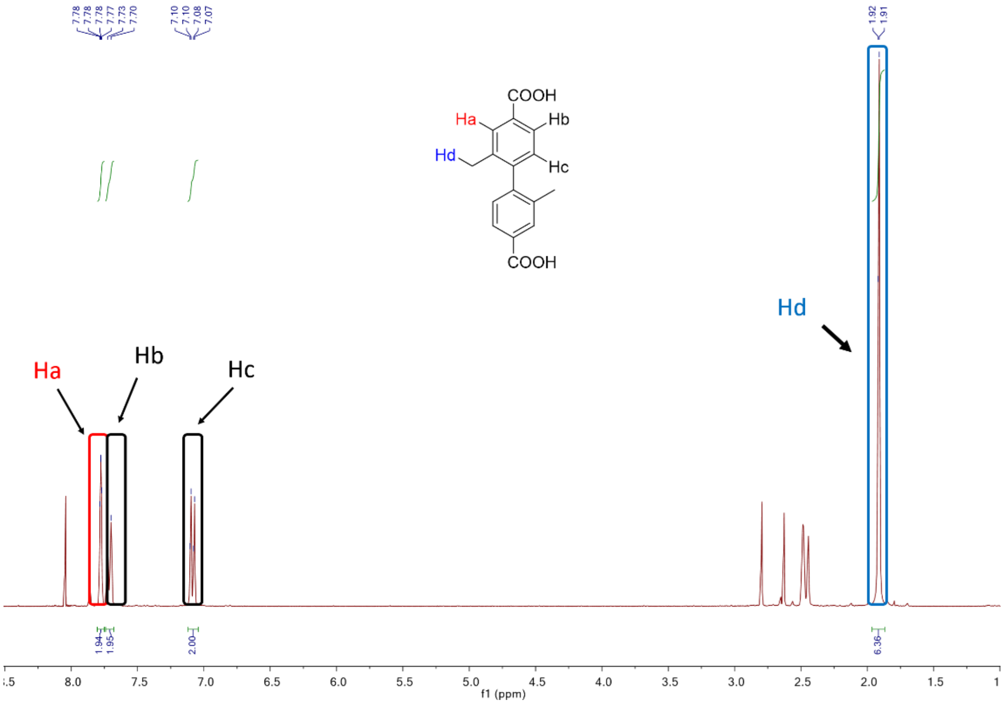

Figure II-19. ^{1}H NMR spectroscopy of PCN-700. Reprinted with permission from *Angew. Chem. Int. Ed.* doi.org/10.1002/anie.202000702.

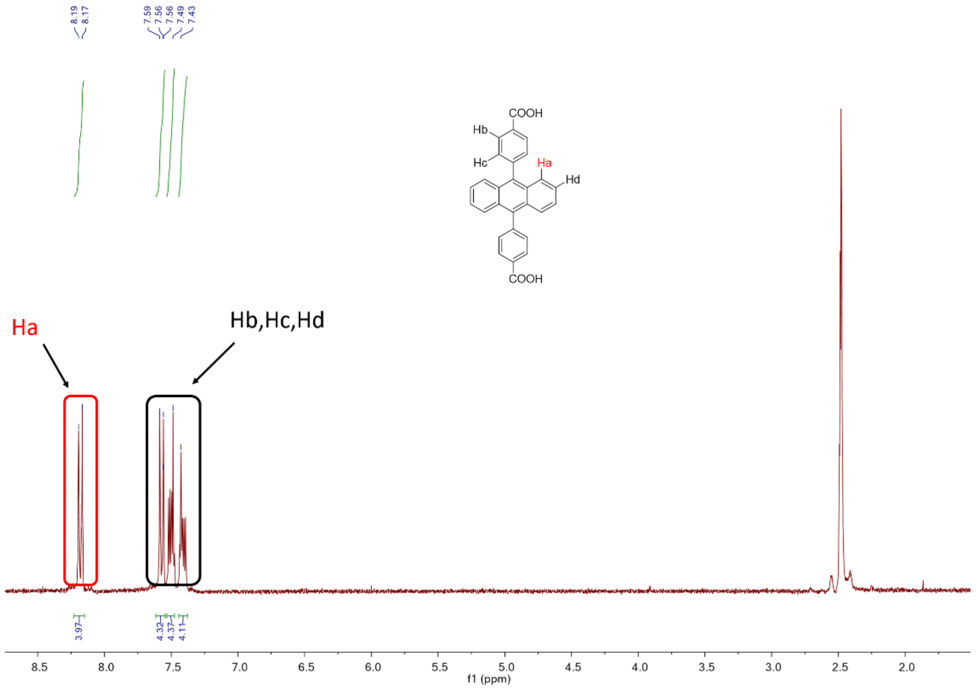

Figure II-20. ^{1}H NMR spectroscopy of L1. Reprinted with permission from *Angew. Chem. Int. Ed.* doi.org/10.1002/anie.202000702.

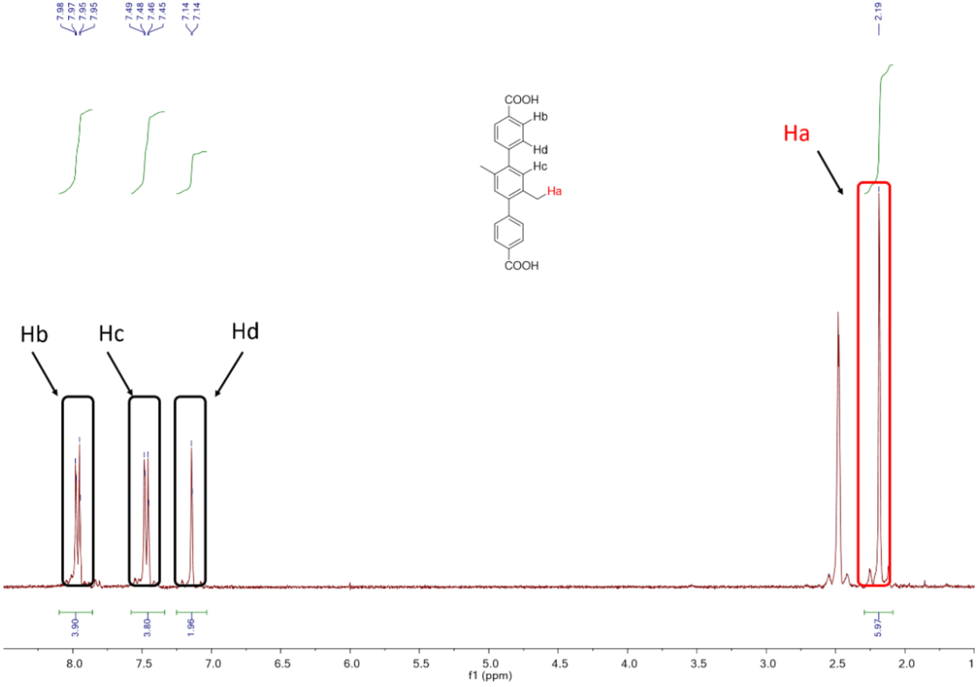

Figure II-21. ^{1}H NMR spectroscopy of L3. Reprinted with permission from *Angew. Chem. Int. Ed.* doi.org/10.1002/anie.202000702.

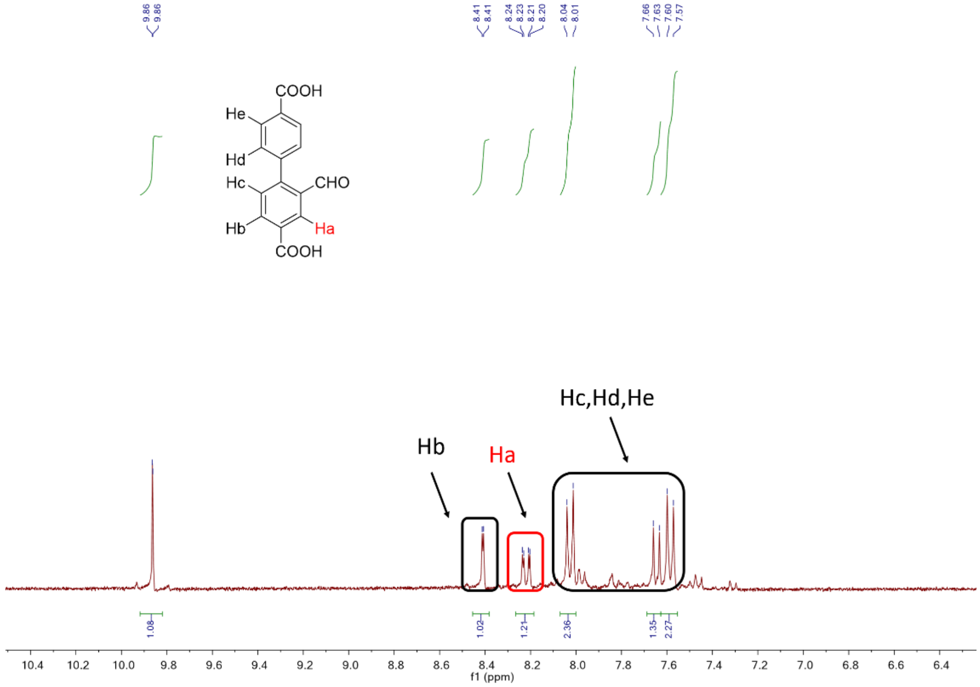

Figure II-22. ^{1}H NMR spectroscopy of L2CHO. Reprinted with permission from *Angew. Chem. Int. Ed.* doi.org/10.1002/anie.202000702.

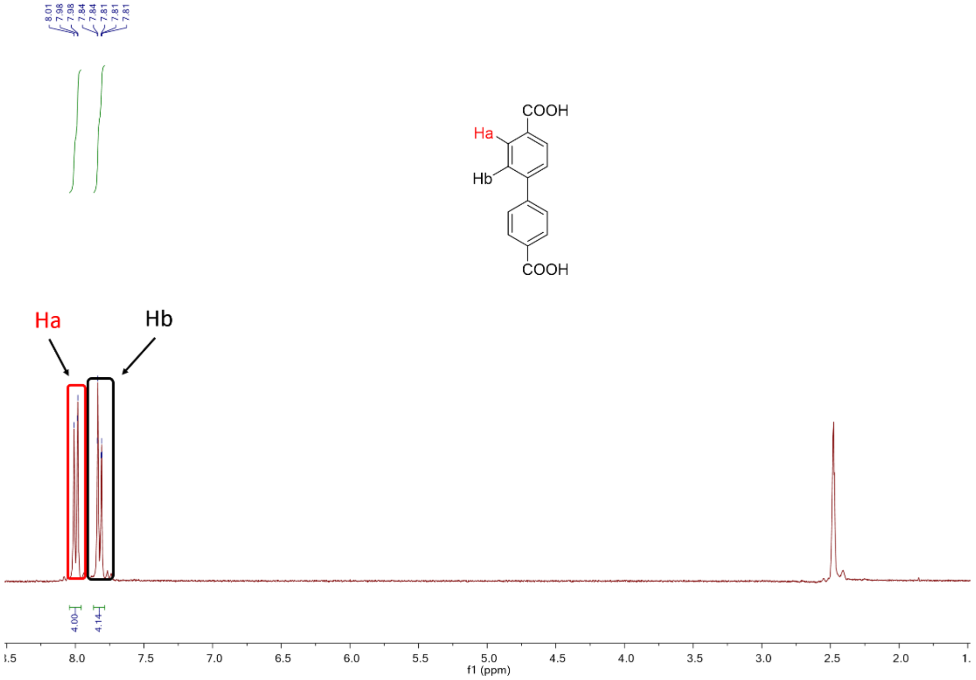

Figure II-23. ^{1}H NMR spectroscopy of H_2BPDC. Reprinted with permission from *Angew. Chem. Int. Ed.* doi.org/10.1002/anie.202000702.

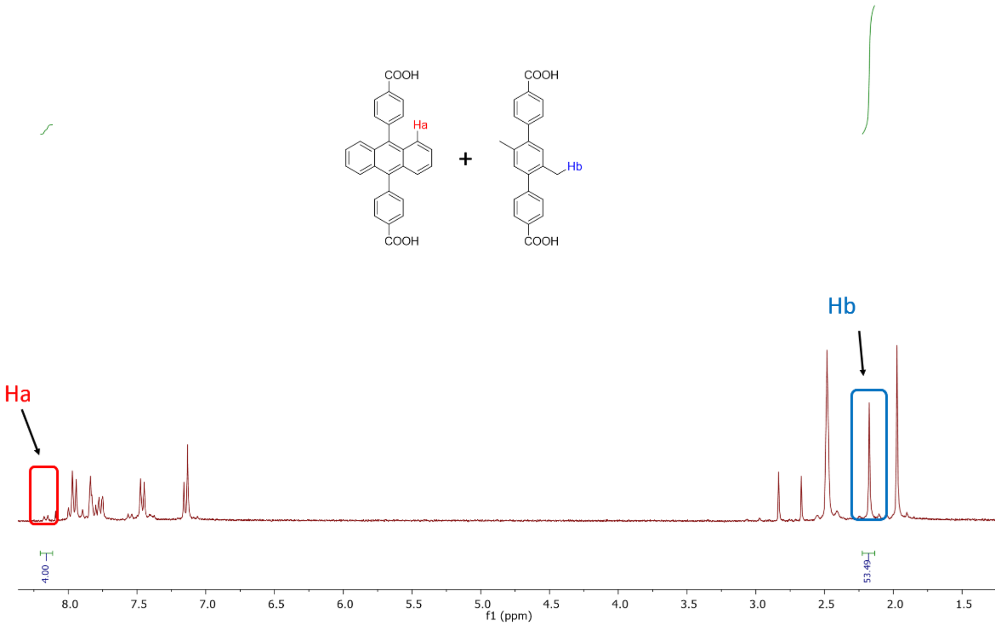

Figure II-24. ^{1}H NMR spectroscopy of PCN-700-L1-7%. Reprinted with permission from *Angew. Chem. Int. Ed.* doi.org/10.1002/anie.202000702.

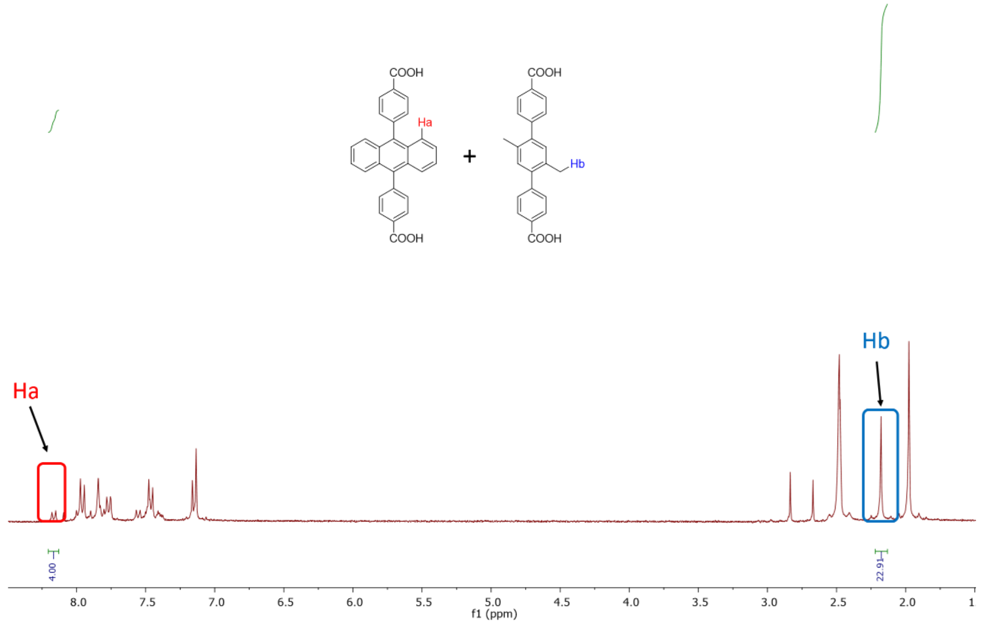

Figure II-25. ^{1}H NMR spectroscopy of PCN-700-L1-20%. Reprinted with permission from *Angew. Chem. Int. Ed.* doi.org/10.1002/anie.202000702.

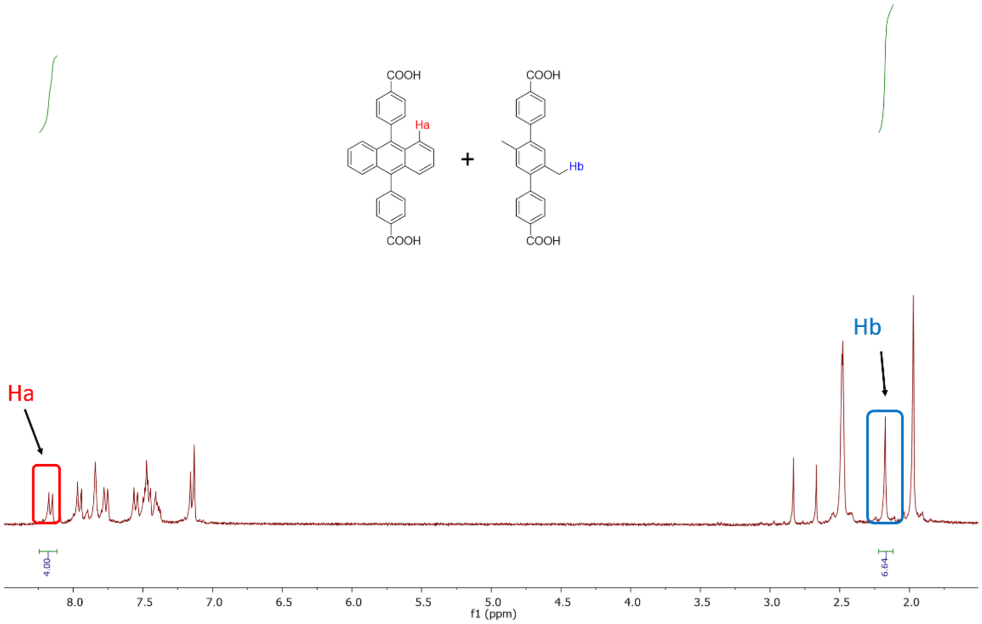

Figure II-26. ^{1}H NMR spectroscopy of PCN-700-L1-43%. Reprinted with permission from *Angew. Chem. Int. Ed.* doi.org/10.1002/anie.202000702.

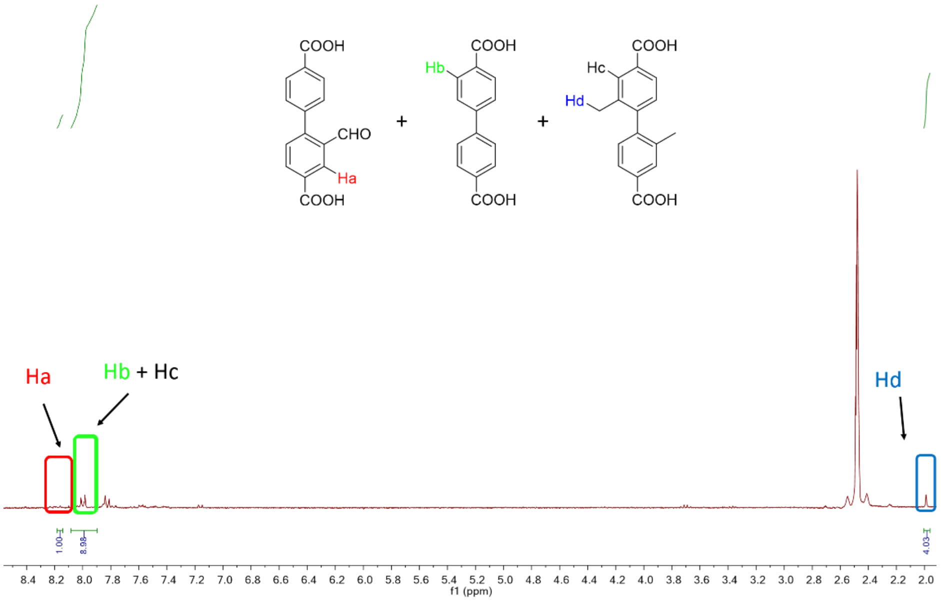

Figure II-27. ^{1}H NMR spectroscopy of PCN-700-L2CHO-30%. Reprinted with permission from *Angew. Chem. Int. Ed.* doi.org/10.1002/anie.202000702.

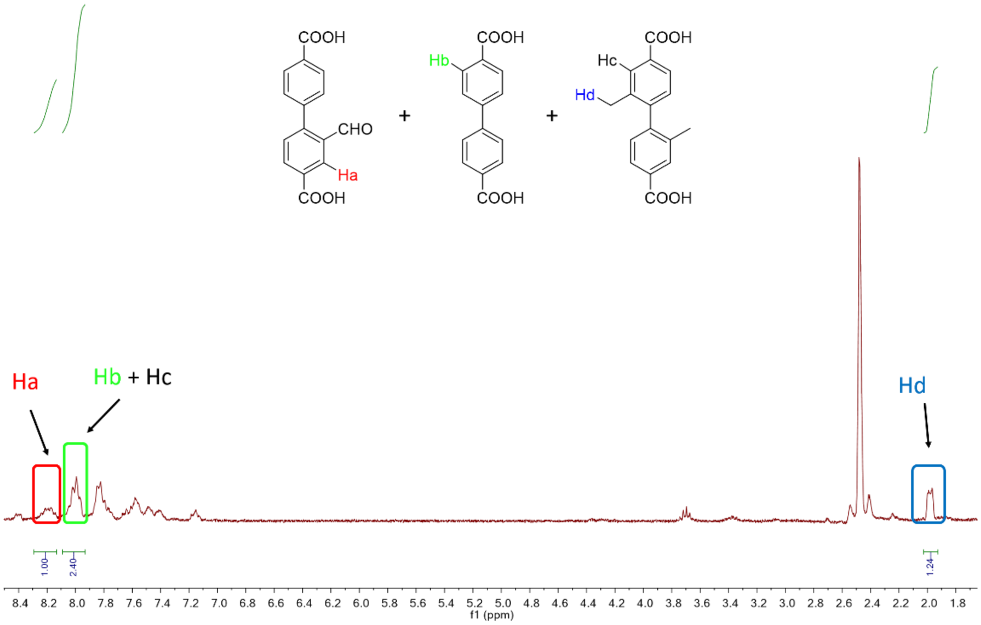

Figure II-28. ^{1}H NMR spectroscopy of PCN-700-L2CHO-50%. Reprinted with permission from *Angew. Chem. Int. Ed.* doi.org/10.1002/anie.202000702.

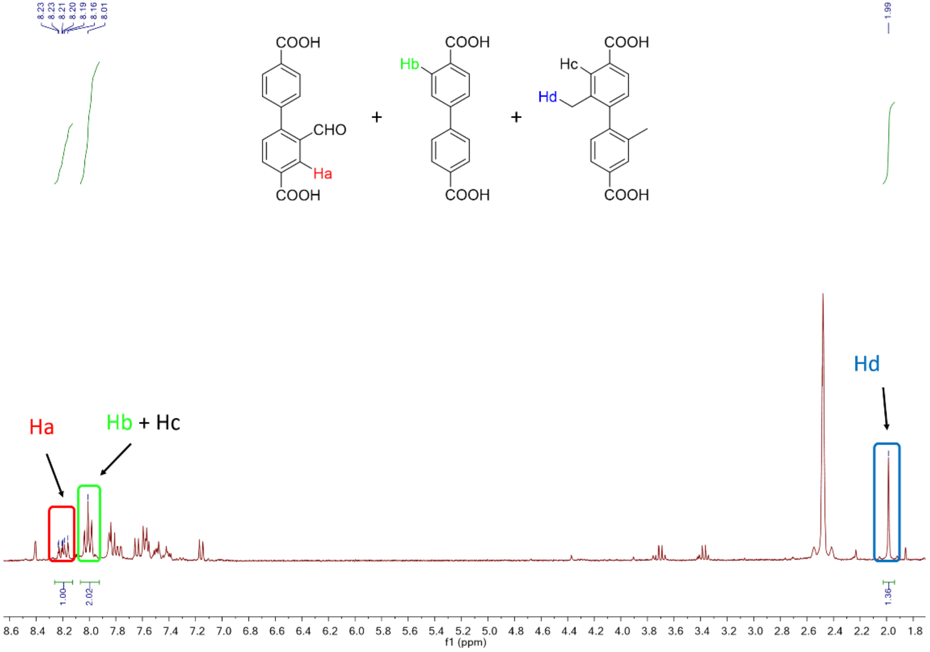

Figure II-29. ^{1}H NMR spectroscopy of PCN-700-L2CHO-75%. Reprinted with permission from *Angew. Chem. Int. Ed.* doi.org/10.1002/anie.202000702.

2.5.6 Optical Images

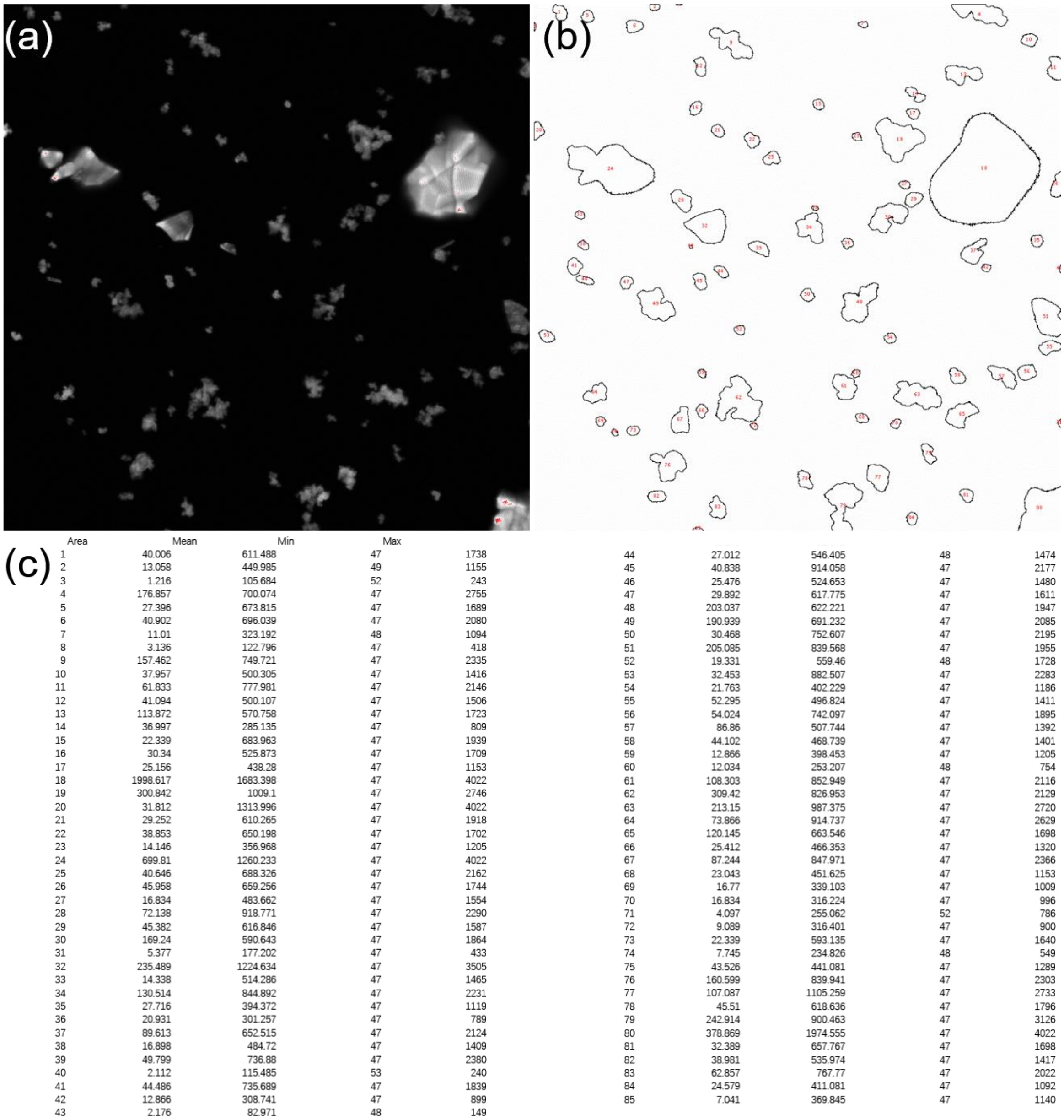

Area	Mean	Min	Max	
1	40.006	611.488	47	1738
2	13.058	449.985	49	1155
3	1.216	105.684	52	243
4	176.857	700.074	47	2755
5	27.396	673.815	47	1689
6	40.902	696.039	47	2080
7	11.01	323.192	48	1094
8	3.136	122.796	47	418
9	157.462	749.721	47	2335
10	37.957	500.305	47	1416
11	61.833	777.981	47	2146
12	41.094	500.107	47	1506
13	113.872	570.758	47	1723
14	36.997	285.135	47	809
15	22.339	683.963	47	1939
16	30.34	525.873	47	1709
17	25.156	438.28	47	1153
18	1998.617	1683.398	47	4022
19	300.842	1009.1	47	2746
20	31.812	1313.996	47	4022
21	29.252	610.265	47	1918
22	38.853	650.198	47	1702
23	14.146	356.968	47	1205
24	699.81	1260.233	47	4022
25	40.646	688.326	47	2162
26	45.958	659.256	47	1744
27	16.834	483.662	47	1554
28	72.138	918.771	47	2290
29	45.382	616.846	47	1587
30	169.24	590.643	47	1864
31	5.377	177.202	47	433
32	235.489	1224.634	47	3505
33	14.338	514.286	47	1465
34	130.514	844.892	47	2231
35	27.716	394.372	47	1119
36	20.931	301.257	47	789
37	89.613	652.515	47	2124
38	16.898	484.72	47	1409
39	49.799	736.88	47	2380
40	2.112	115.485	53	240
41	44.486	735.689	47	1839
42	12.866	308.741	47	899
43	2.176	82.971	48	149
44	27.012	546.405	48	1474
45	40.838	914.058	47	2177
46	25.476	524.653	47	1480
47	29.892	617.775	47	1611
48	203.037	622.221	47	1947
49	190.939	691.232	47	2085
50	30.468	752.607	47	2195
51	205.085	839.568	47	1955
52	19.331	559.46	48	1728
53	32.453	882.507	47	2283
54	21.763	402.229	47	1186
55	52.295	496.824	47	1411
56	54.024	742.097	47	1895
57	86.86	507.744	47	1392
58	44.102	468.739	47	1401
59	12.866	398.453	47	1205
60	12.034	253.207	48	754
61	108.303	852.949	47	2116
62	309.42	826.953	47	2129
63	213.15	987.375	47	2720
64	73.866	914.737	47	2629
65	120.145	663.546	47	1698
66	25.412	466.353	47	1320
67	87.244	847.971	47	2366
68	23.043	451.625	47	1153
69	16.77	339.103	47	1009
70	16.834	316.224	47	996
71	4.097	255.062	52	786
72	9.089	316.401	47	900
73	22.339	593.135	47	1640
74	7.745	234.826	48	549
75	43.526	441.081	47	1289
76	160.599	839.941	47	2303
77	107.087	1105.259	47	2733
78	45.51	618.636	47	1796
79	242.914	900.463	47	3126
80	378.869	1974.555	47	4022
81	32.389	657.767	47	1698
82	38.981	535.974	47	1417
83	62.857	767.77	47	2022
84	24.579	411.081	47	1092
85	7.041	369.845	47	1140

Figure II-30. Demonstration of intensity calculation of confocal microscope image for PCN-700-L1-L2Hcy-30%. (a) Confocal microscope image. (b) Areas detected by ImageJ. (c) Intensity calculated by ImageJ. Reprinted with permission from *Angew. Chem. Int. Ed.* doi.org/10.1002/anie.202000702.

2.5.7 Additional Figures

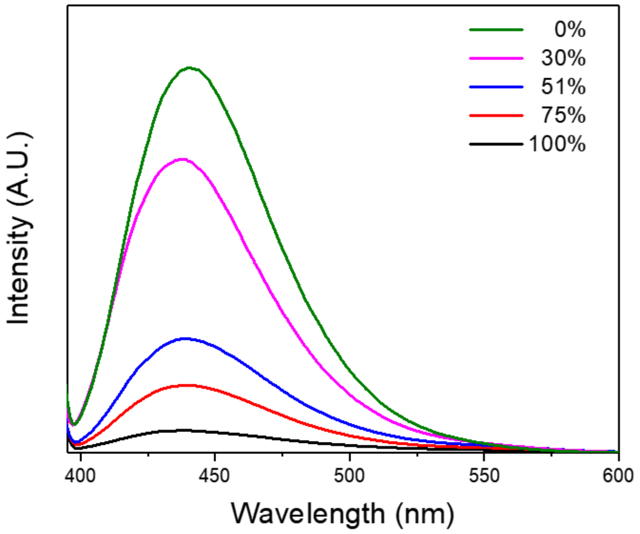

Figure II-31. **Fluorescent spectrum of PCN-700-L1-L2Hcy-X%.** Reprinted with permission from *Angew. Chem. Int. Ed.* doi.org/10.1002/anie.202000702.

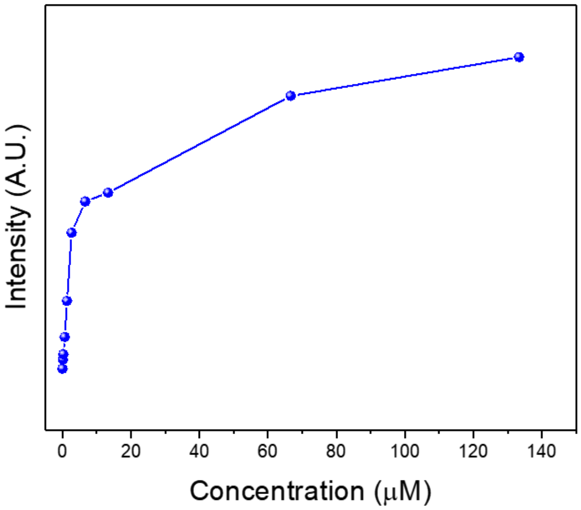

Figure II-32. Fluorescent intensity response of PCN-700-L1-L2Hcy-75% to different concentration of CN^- solutions. Reprinted with permission from *Angew. Chem. Int. Ed.* doi.org/10.1002/anie.202000702.

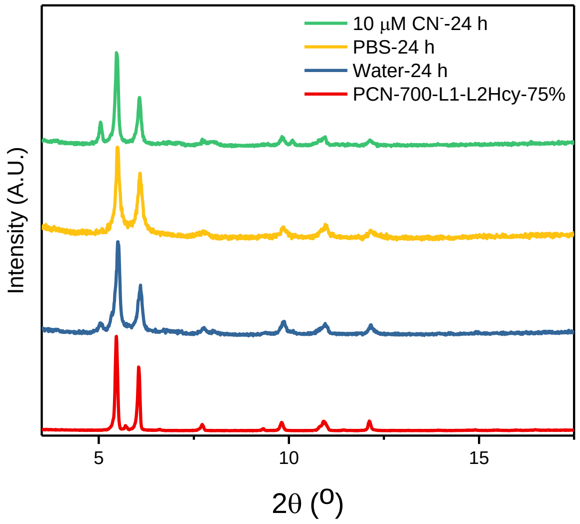

Figure II-33. PXRD patterns of PCN-700-L1-L2Hcy-75% after emmersing in water, PBS and 10 μM CN^- solutions for 24 h. There is no significant change of peaks which implies the good stability of PCN-700-L1-L2Hcy-75%. Reprinted with permission from *Angew. Chem. Int. Ed.* doi.org/10.1002/anie.202000702.

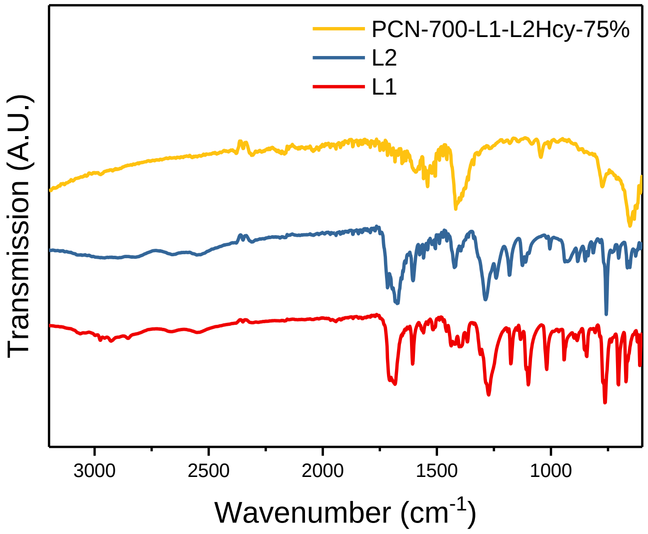

Figure II-34. FTIR spectrum of L1, L2 and PCN-700-L1-L2Hcy-75%. The absence of C=O peak around 1700 cm^{-1} of PCN-700-L1-L2Hcy-75% showed that there is no L1 or L2 physically adsorbed. All ligands are coordinated with Zr clusters. Reprinted with permission from *Angew. Chem. Int. Ed.* doi.org/10.1002/anie.202000702.

CHAPTER III

FLUORESCENCE ENHANCEMENT BY ISOLATING PERYLENE IN SOLID STATE VIA METAL-ORGANIC FRAMEWORKS[*]

3.1 Introduction

Polycyclic aromatic hydrocarbons such as perylene, pyrene, and their derivatives are highly emissive fluorophores in solution phase with wide applications in the field of molecular electronic and light emitting devices. However, the practical applications of these materials are often hindered by self-quenching effects due to the formation of non-fluorescent aggregates in concentrated solutions or in the solid state. Herein, we demonstrate that aggregation caused quenching of perylenes can be minimalized by molecular incorporation into metal-organic frameworks (MOFs). This study utilized a stable Zr6 cluster-based MOF, UiO-67, as a matrix. Linear linkers containing the photo-responsive moieties were designed and incorporated into the parent UiO-67 scaffold through the partially replacement of the non-fluorescent linkers of a similar length, forming mixed-linker MOFs. The average distance between perylene moieties was tuned by changing the linker ratios, thus controlling the fluorescence intensity, emission wavelength, and quantum yield. Molecular modeling was further adopted to correlate the

---

[*] Reprinted with permission from “Fluorescence Enhancement in Solid State by Isolating Perylene Fluorophores in Metal-Organic Frameworks.” Li, J.; Yuan, S.; Qin, J.-s.; Huang, L.; Bose, R.; Pang, J.; Zhang, P.; Xiao, Z.; Tan, K.; Malko, A. V.; Cagin, T.; Zhou, H.-C., (2020). *ACS Appl. Mater. Interfaces.* doi.org/10.1021/acsami.0c05512 Copyright 2020 American Chemical Society.

number of isolated perylene linkers within the framework to the ratio between the two linkers, therefore rationalizing the change in the observed fluorescent properties. Taking advantage of the tunable fluorescence, inherent porosity, and high chemical stability of this MOF platform, it was applied as a fluorescent sensor for oxygen detection in the gas phase, showing fast response and good recyclability.

3.2 Background

Polycyclic aromatic hydrocarbons, with extended π conjugated structures, have been widely investigated as candidates of fluorescent materials.[157-160] Perylene is known to have intriguing photophysical properties such as high fluorescence quantum yield, long lifetimes of excited singlet, environment responsive emissions, and the ability to form excimers/exciplex by aggregation. Therefore, perylene and its derivatives have attracted enormous research interests as highly emitting materials for chemosensors, light-emitting diodes (LEDs), liquid crystal lasers, and solar cells.[161-164] Despite numerous advantages, the practical application of perylene-based fluorophores is often limited by their poor solubility and their tendency to form π-stacked aggregates with forbidden fluorescence (so-called H-aggregates). This phenomenon, known as "aggregation-caused quenching" (ACQ), has been observed in many π conjugated systems. Applications for fluorescent devices often require the fluorophore to be in a solid state. However, perylene solids are usually non-fluorescent due to the ACQ effect, hindering their application (Figure III-1). In addition, some luminescence probes based on hydrophobic aromatics form aggregates in polar solvents further limiting their application. To eliminate the ACQ effect, bulky substituents such as alkyl groups or cyclodextrin groups have been introduced to the aromatic fluorophores, preventing the stacking of the π conjugated structures. For example, alkyl substituted pyrene molecules were synthesized showing enhanced fluorescence induced by the incorporation of alkyl groups.[165] In another example, perylene bisimide was grafted onto β-cyclodextrin molecules to avoid aggregation, resulting in a solid-state vapor fluorescence sensor.[166] Although these modification methods effectively reduced ACQ, they usually require complicated structural design and tedious organic synthesis. Furthermore, the application of these non-porous solids as fluorescent gas sensors are often hindered by their low gas permeability. As an alternative to molecular covalent modifications, metal−ligand coordination interactions represent an effective approach to the controlled assembly of aromatic fluorophores. This idea has been recently demonstrated in an elegant work by Peter J. Stang and coworkers where they demonstrated the increased solubility and enhanced fluorescent tunability of metallocycles that contained pyrene molecules in the super structure.[167]

It has been demonstrated that metal-organic frameworks (MOF) could be utilized as ideal platforms for the isolation of aromatic fluorophores in the solid state. MOFs are a class of porous materials constructed from metal-based inorganic nodes and organic linkers. Due to their inherent porosity and structural diversity, MOFs have been recognized as potential candidates for various applications, including gas storage/separation, catalysis, chemical sensing, energy harvesting, and biomedicine.[38, 119-120, 122-123, 168] The structure, composition and physiochemical properties of MOFs are highly tunable through the judicious selection of the metal nodes and organic linkers. Organic fluorophores such as pyrene, anthracene, tetraphenylethylene, boron dipyrromethene, and porphyrin, have been designed as organic linkers, forming solid state fluorescent MOFs.[3, 61, 66-67] These MOFs can be viewed as an inherent three-dimensional array of fluorescent molecules separated from each other through a vast array of highly ordered metal-based inorganic nodes. Compared with traditional organic fluorescent materials, MOFs exhibit additional advantages in fluorescent sensing: 1) the rigid framework structure prevents the formation of π-stacking between aromatic fluorophores, enhancing their fluorescence; 2) the inherent porosity of the framework ensures the access of guest molecules even in bulk materials without necessarily fabricating thin films.

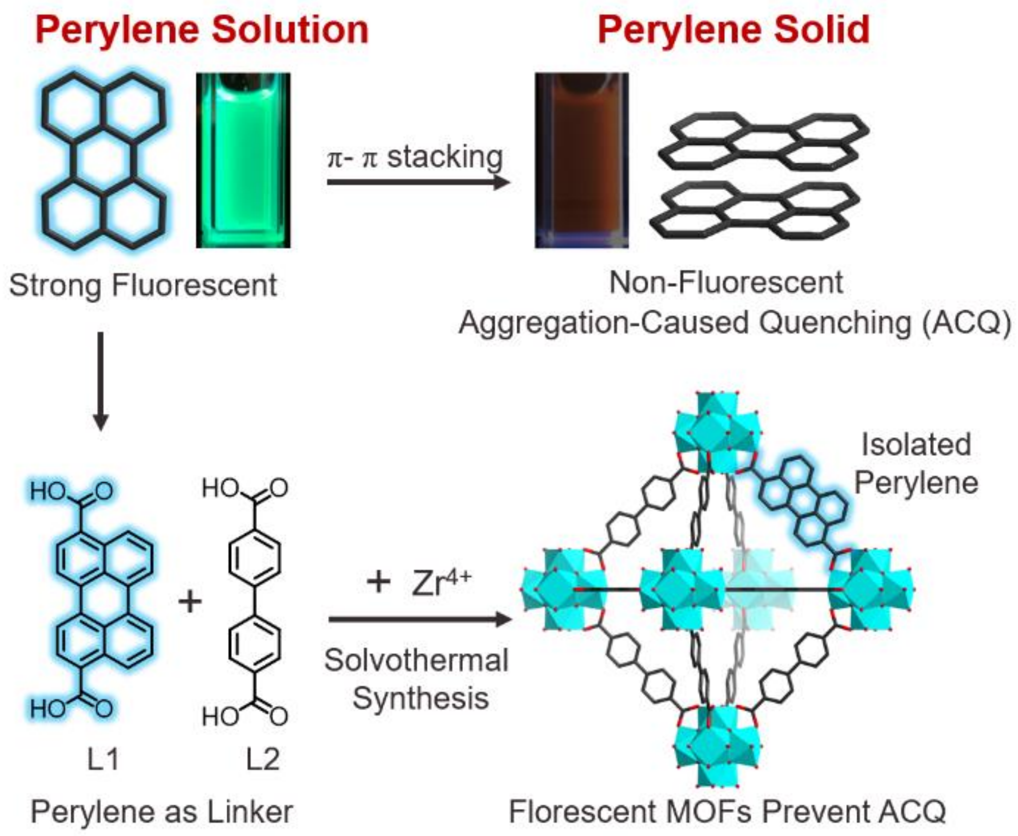

Figure III-1. The design isolated perylene fluorophores in a solid MOF. Reprinted with permission from *ACS Appl. Mater. Interfaces.* doi.org/10.1021/acsami.0c05512.

Herein, we isolated perylene fluorophore in a MOF to enhance fluorescence by avoiding ACQ. Linear organic linkers with perylene moieties as part of the backbone (3,10-perylene-dicarboxylate, denoted as L1) were connected with Zr6-nodes to form UiO-67 isostructures (University of Oslo). The concentration of the perylene moieties within the MOF were further optimized by partially replacing with a non-fluorescent linker of similar length (4,4'-biphenyldicarboxylate, denoted as L2), forming mixed-linker MOF series (Figure III-1). By tuning the linker ratios, the distance between the perylene molecules could be adjusted, which in turn modulated the excimer formation and photophysical properties of MOFs. By carefully controlling the linker ratios, a highly fluorescent MOF with inherent porosity and strong chemical stability was obtained which acts as a fluorescent sensor for the detection of oxygen gas.

3.3 Results and Discussions

A Zr-based MOF, UiO-67, was initially selected as a platform because of its high chemical stability and the close shell d0 configuration of the Zr^{4+} metal centers, precluding any contribution from paramagnetic quenching by the metal clusters. A fluorescent linker, L1, was designed by anchoring two carboxylate groups to the 3,10-position of perylene molecules. Meanwhile, a non-fluorescent linker L2, possessing an identical length to that of L1, was selected. The combination of the linear linkers and the Zr metal clusters was expected to give rise to a Zr-MOFs with the fcu topology. Furthermore, it has been reported that linkers with identical lengths and coordination groups but different substituents can be incorporated into a mixed-linker MOF without phase separation.

Therefore, we expected that L1 and L2 could be simultaneously incorporated into a UiO-type MOF scaffold in the form of a solid solution.

As expected, an isoreticular UiO-67 MOF structure was obtained through the solvothermal reaction between L1, L2, and Zr^{4+}. By varying the L1 ratio in the starting material from 0 to 100%, MOFs with the same framework structure but different perylene contents were obtained, namely UiO-67-X%. The L1 ratio (X%) in UiO-67-X%, defined as the moles of L1 divided by the moles of total organic linkers (L1 + L2), were be determined by the 1H-NMR and UV-Vis of the digested samples (Figure III-2). Single crystals of UiO-67-8% were successfully obtained. Single crystal X-ray diffraction (SCXRD) revealed that UiO-67-8% crystallized in the cubic space group Fm-3m.[169] The structure of UiO-67-8% was similar to that of UiO-67. Each Zr_6 cluster was 12-connected to linear linkers, forming a network with the fcu topology. The existence of both L1 and L2 in the mixed-linker UiO-67-8% was clearly observed in the single crystal structures in which L1 and L2 were substitutional disordered (Figure III-3). Meanwhile, the L1 is two-fold disordered because of the high symmetry of the crystal lattice (Fm-3m). The occupancy of L1 was refined as 0.08 in UiO-67-8% based on the 1H-NMR data of the digested sample. Further increasing the L1 concentration caused severe disorders so that the crystal structures cannot be precisely refined from SCXRD data. Powder X-ray diffraction patterns (PXRD) of the UiO-67-X% series (X = 0, 1.8, 3.8, 20, 41, and 100%) are almost identical (Figure III-4). These results are in line with the same framework structures determined by SCXRD. The PXRD pattern matches well with simulations based on SCXRD, verifying the phase purity of the bulk samples.

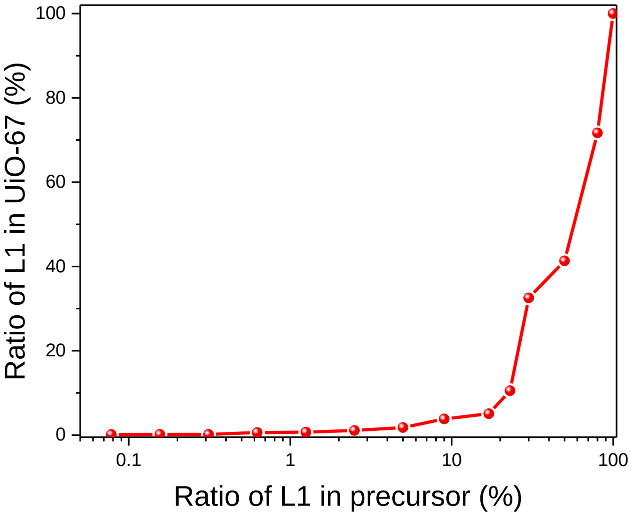

Figure III-2 Correlation of linker ratio in starting materials and MOF products. Reprinted with permission from *ACS Appl. Mater. Interfaces.* doi.org/10.1021/acsami.0c05512.

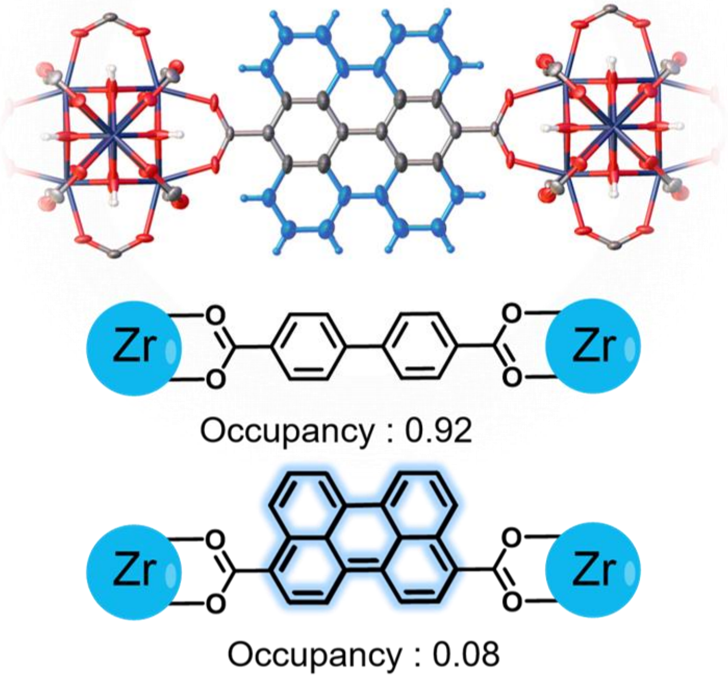

Figure III-3. Single crystal structure of UiO-67-0.8% showing the co-existence of L1 (blue) and L2 (black). Reprinted with permission from *ACS Appl. Mater. Interfaces.* doi.org/10.1021/acsami.0c05512.

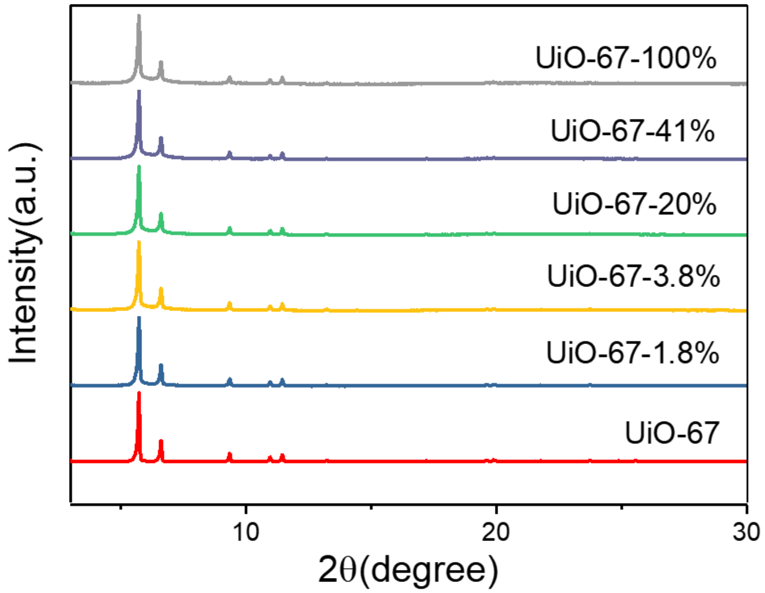

Figure III-4. PXRD patterns of UiO-67-X% (X = 0, 1.8, 3.8, 20, 41, and 100%). Reprinted with permission from *ACS Appl. Mater. Interfaces.* doi.org/10.1021/acsami.0c05512.

The porosity of the UiO-67-X% series (X = 0, 1.8, 3.8, 20, 41, and 100%) was determined through N_2 adsorption-desorption isotherms at 77 K, 1 bar. The total N_2 uptakes were shown to gradually decrease with the increase of L1 concentration in the sample (Figure III-5). This corresponded to the partial occupancy of the pore space by the bulkier perylene moieties. This result was in line with the pore size distributions for the MOFs as well, showing a reduction in the pore size upon the incorporation of L1. UiO-67 possesses a total N_2 uptake of 740 $cm^3 \cdot g^{-1}$, BET surface area of 2120 m^2g^{-1} and a pore size of 1.2 nm, whereas UiO-67-100% showed a reduced N_2 uptake (450 $cm^3 \cdot g^{-1}$), BET surface area (1168 m^2g^{-1}) and pore size (1.0 nm). The uniform and gradually reduced pore size upon the incorporation of L1 also suggests that the two linkers were well-mixed within the framework (Figure III-6).

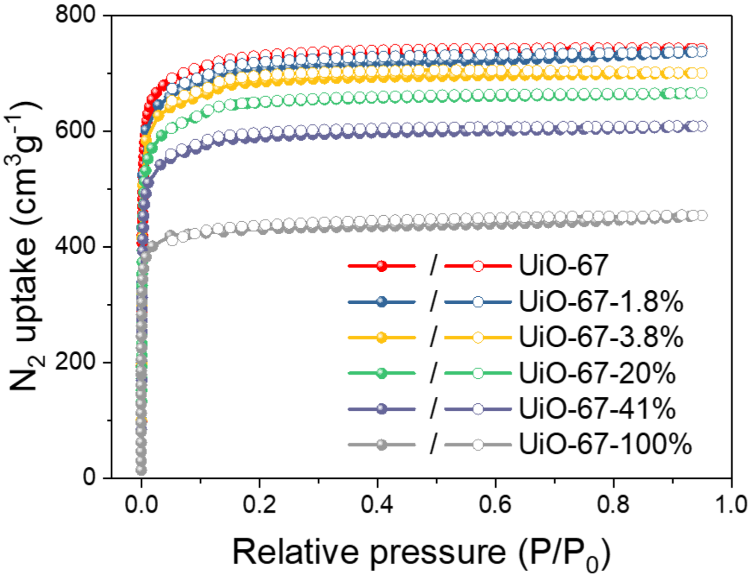

Figure III-5. N$_2$ adsorption-desorption isotherms of UiO-67-X% (X = 0, 1.8, 3.8, 20, 41, and 100%) at 77 K, 1 bar. Reprinted with permission from *ACS Appl. Mater. Interfaces.* doi.org/10.1021/acsami.0c05512.

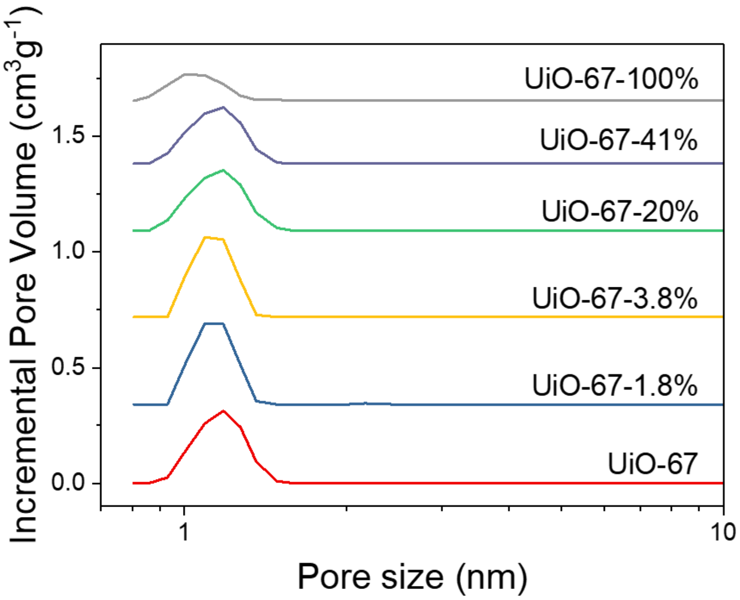

Figure III-6. Pore size distribution derived from adsorption isotherms. (e) PL emission spectra of UiO-67-X% (excitation wavelength 300 nm). Reprinted with permission from *ACS Appl. Mater. Interfaces.* doi.org/10.1021/acsami.0c05512.

The UiO-67-X% series are fluorescent platform with well separated perylene molecules, preventing ACQ affects. Moreover, the average distance between the fluorophores could be modified by adjusting the concentration of the perylene containing linker in the mixed-linker MOF. The UV-vis absorption spectra and photoluminescence (PL) emission spectra for the MOF was monitored as linker ratios were adjusted (Figure III-7). The absorption spectrum showed a signature perylene-linker, L1, peak at 445 nm, while the adsorption of the non-perylene containing linker, L2, appeared at 275 nm. This is further confirmed by the increased perylene peak intensity upon increasing the concentration of L1 in the MOF. The excitation wavelength for the PL spectra was set to 300 nm. This wavelength was chosen as L1 has a strong absorption at 300nm but L2 remains silent. Upon irradiation at 300 nm, the samples with low L1 ratios (< 0.35 %) showed a single emission peak centered at 400 nm. This peak corresponded to the emission of the isolated perylene monomers. When the L1 doping ratio was higher than 0.35 %, a broad emission peak emerged at ~520 nm. This peak could be attributed to excimer formation between adjacent perylene moieties. Along with the augmentation of the excimer emission peak at ~520 nm, the monomer emission band was shown to dramatically decreases as a function of concentration of the linker. The larger the contribution of the excimers to the emission of the MOF, the more the observed fluorescence became redshifted. The excimer emission reached a maximum when the content of the L1 linker reached 1.8%. Further increases to the L1 concentration in the final MOF significantly decreased the emission intensity of both monomer and excimer. The UiO-67-30% framework had little to no fluorescence due to concentration-based quenching. The change of the fluorescent intensity and wavelengths could be visually observed in the photos of the UiO-67-X% samples under ambient light and UV light (365 nm, Figure III-8, III-9). The peak intensities of the monomer (400 nm) and excimer emissions (520 nm) were plotted against the L1 ratio to demonstrate the excimer formation and concentration quenching. Due to samples over 10% have almost none PL intensity, only samples within 10% were included when discussing their PL intensity. The excitation lifetime also showed a strong dependence on the L1 ratio, reaching a maximum when the L1 concentration was within the range of 0.35-1.8%. This agreed well with the formation of the excimers and the quenching of the fluorescence emission. The global fluorescence quantum yields of the solid UiO-67-X% samples were measured in air, and were shown to follow a similar trend to the PL intensity. UiO-67-1.8% had the highest quantum yield (50%) of the UiO-67-X% series (Figure III-10). A similar excimer formation and the concentration-based quenching phenomenon has been previously reported for a naphthalene-based MOF.[170]

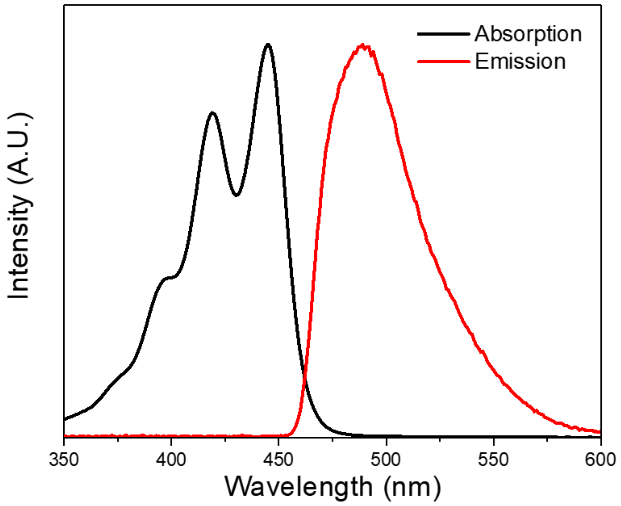

Figure III-7. Fluorescence spectrum (red) and UV-Vis spectrum (Black) of L1 in DMF. Reprinted with permission from *ACS Appl. Mater. Interfaces.* doi.org/10.1021/acsami.0c05512.

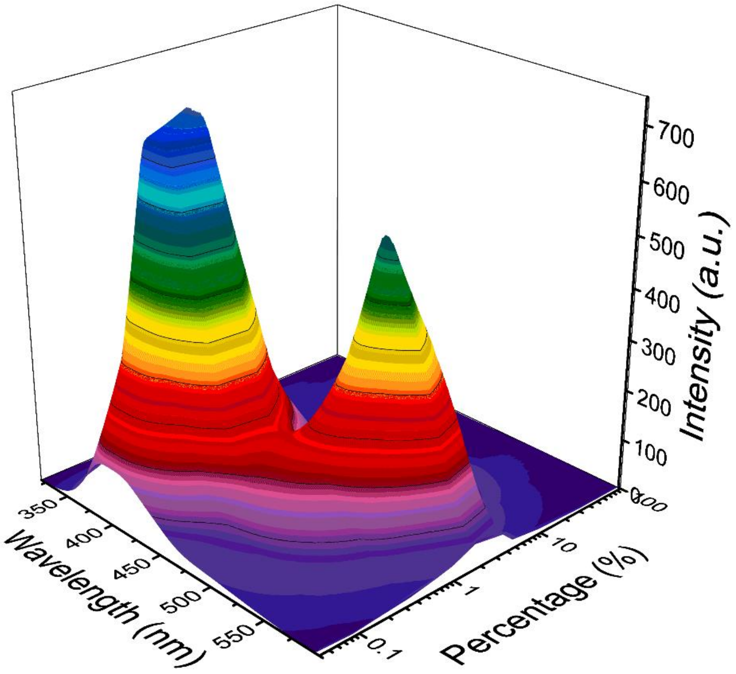

Figure III-8. PL emission spectra of UiO-67-X% (excitation wavelength 300 nm). Reprinted with permission from *ACS Appl. Mater. Interfaces.* doi.org/10.1021/acsami.0c05512.

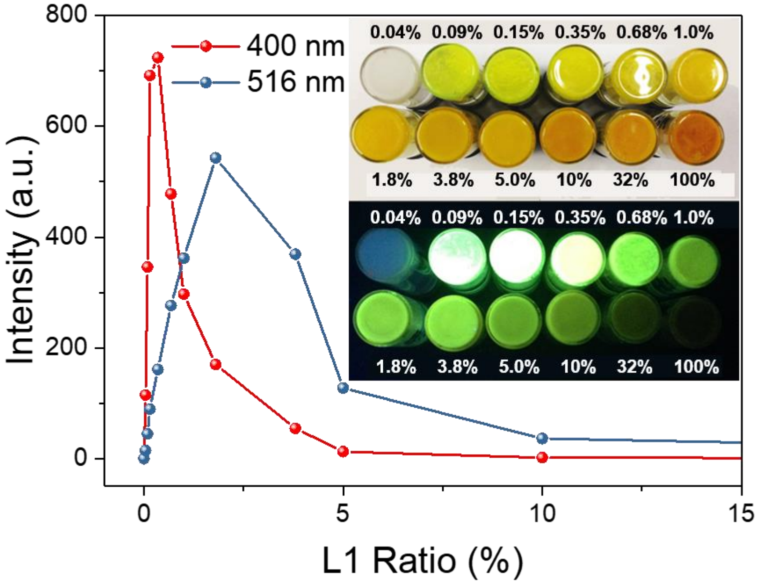

Figure III-9. Intensity of monomer (400 nm) and excimer emission peaks (520 nm) as a function of L1 ratios. Insert shows the photos of UiO-67-X% samples under ambient light and UV light (365 nm). Reprinted with permission from *ACS Appl. Mater. Interfaces.* doi.org/10.1021/acsami.0c05512.

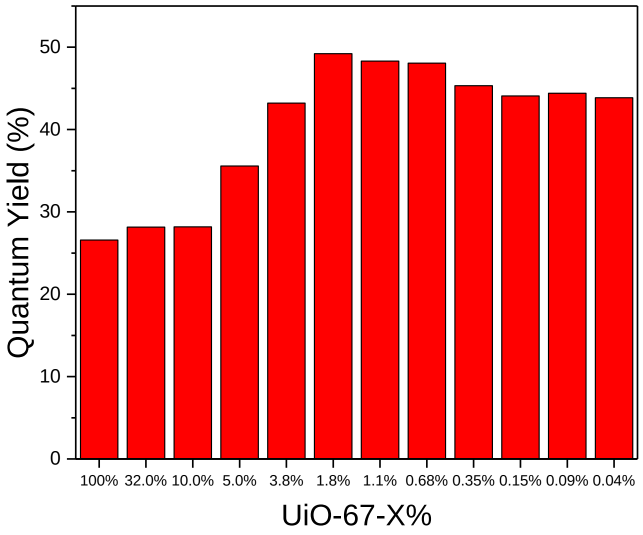

Figure III-10. Quantum Yield of UiO-67-X%. Reprinted with permission from *ACS Appl. Mater. Interfaces.* doi.org/10.1021/acsami.0c05512.

To understand the distribution of fluorescent L1 linker in the framework of UiO-67-X%, models of UiO-67-X% were constructed by Monte Carlo simulation.[171] It has been demonstrated that variation of the interactions between linkers in a mixed-linker MOF can lead to different apportionment.[172] Linkers with preferential interactions (i.e. Intermolecular attractions) with each other form clusters in the MOF lattice, whereas linkers without preferences give random distributions. Therefore, a 7.5×7.5×7.5 superlattice of UiO-67-X% was constructed and the original L2 linkers was randomly replaced by fluorescent L1 linker. Monte Carlo simulation was then conducted by randomly exchange linkers within the superlattice, and the exchange was accepted depending on the energy. By adjusting the interaction energies between L1, three models of UiO-67-X% were resulted, where L1 is formed large clusters, small clusters, or arranged randomly. The ratios of L1 were increased from 0.078% to 30%, and the modeling process iterated to get structural models of UiO-67-X% with different L1 ratios. For example, the three structural models of UiO-67-6% were illustrated (Figure III-11a), in which L1 is randomly distributed or aggregates into clusters with different sizes. The fluorescent intensity of UiO-67-X% at 400 nm can be estimated by the number of isolated L1 linkers, because adjacent L1 linkers form excimer and quenched the fluorescence. The fluorescent intensity for UiO-67-X% with various L1 ratios and different distributions of L1 was calculated (Figure III-11b). A plot of normalized intensity against the L1 ratio in UiO-67-X% shows a dramatically different self-quenching behavior of large cluster, small cluster, and random models. When L1 form large clusters within the lattice, the fluorescence is completely quenched only 0.15% L1 presented. Indeed, any L1 linkers will aggregate into clusters in this structural model, which explains the immediately quenched intensity even at low L1 ratios. Small cluster model and random model both show the highest fluorescent intensity at L1 ratio of ~0.2%. However, the fluorescent intensity of random model quickly decreases as the L1 ratio increase to 1.2%, whereas the small cluster model maintains its fluorescence until L1 ratio reaches 10%. This is explained by the fact that the formation small clusters reduce the average concentration of L1 in the rest part of the material, therefore, the fluorescence is not quenched at high L1 ratios. The small cluster model fits better to the experimental fluorescent data, suggesting that the L1 linker in UiO-67-X% tend to form small clusters. The preferential interactions between L1 was tentatively attributed to the π-interactions between conjugated perylene moieties of L1.

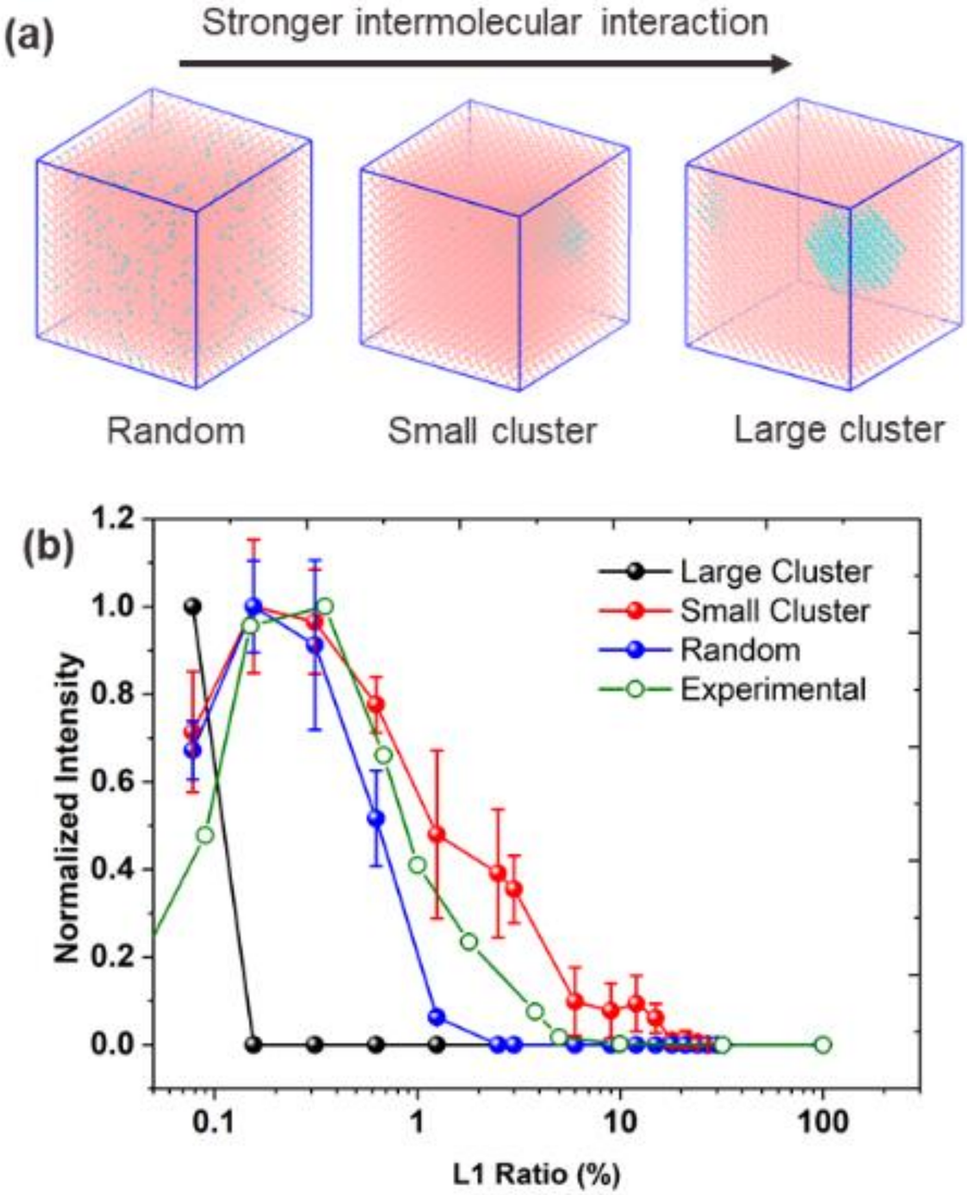

Figure III-11. (a) Structural models of UiO-67-6% showing different distribution of L1 (blue) and L2 (red). (b) Simulated fluorescent peak intensity of monomer (400 nm) as a function of L1 ratios. Reprinted with permission from *ACS Appl. Mater. Interfaces.* doi.org/10.1021/acsami.0c05512.

The tunable fluorescent properties and inherent porosity of the UiO-67-X% series enabled their utilization as a platform for the fabrication of gas sensors. Bulk UiO-67-X% samples were directly utilized for gas sensing without the fabrication of thin films. The highly porous structure of the framework allowed for the efficient diffusion of gas molecules, enabling rapid access to the fluorophore. As a proof of concept, UiO-67-X% MOFs were optimized for the detection of oxygen in the gas phase (Figure III-12). The fluorescent emission spectra of UiO-67-1.8% and UiO-67-0.35% were recorded in a gas mixture with various O_2/N_2 ratios at 1 bar under 300 nm light irradiation. The sensitivity (R) of the fluorophores were defined as the quenching of the emission intensity in pure O_2 divided by the inherent emission intensity in pure N_2. UiO-67-1.8% was demonstrated to be the top-performing material with the highest sensitivity among the UiO-67-X% MOFs. The PL spectra of UiO-67-1.8% quickly changed upon the exposure of O_2/N_2 gas, reaching equilibrium within seconds. This supported the idea that a fast diffusion of the gas within the framework was possible due to the high porosity of the material. The PL spectra clearly showed that both the monomer and excimer emission of UiO-67-1.8% were sensitive to O_2, but the excimer emission peak possessed higher sensitivity (R = 70%) than that of the monomer (58%) (Figure III-13). It may be contributed to that the interactions between triplet and ground state may lower the energy of upper triplet slightly. Thus, the energy of excimer is almost equal to the second triplet state resulting in higher sensitivity of the excimer.[173] The limit of detection is 5%. The stability of UiO-67-1.8% and UiO-67-0.35% were also tested via exposure to 100% O_2 and N_2 alternately. The performance of both sensors maintained the same during 5 cycles, indicating the good recyclability of them as

O_2 sensors (Figure III-14 and III-15). The fluorescent quenching by O_2 is attributed to the energy transfer from the triplet state in the perylene unit to the ground state oxygen. This transition has previously been well-investigated.[174] As a control, the sensitivity of the perylene linkers both in aqueous solution and in the solid state was tested (Figure III-16). The perylene-linker showed almost no fluorescence in the solid state because of severe ACQ, resulting in low sensitivity. The sensitivity of the L1 solutions (10%) was also much lower than that of the MOF. Additionally, each solution required up to 30 minutes of O_2/N_2 gas exposure to equilibrate. The oxygen gas needed to be pre-dissolved in the solution to quench the fluorophore adequately as a positive control.

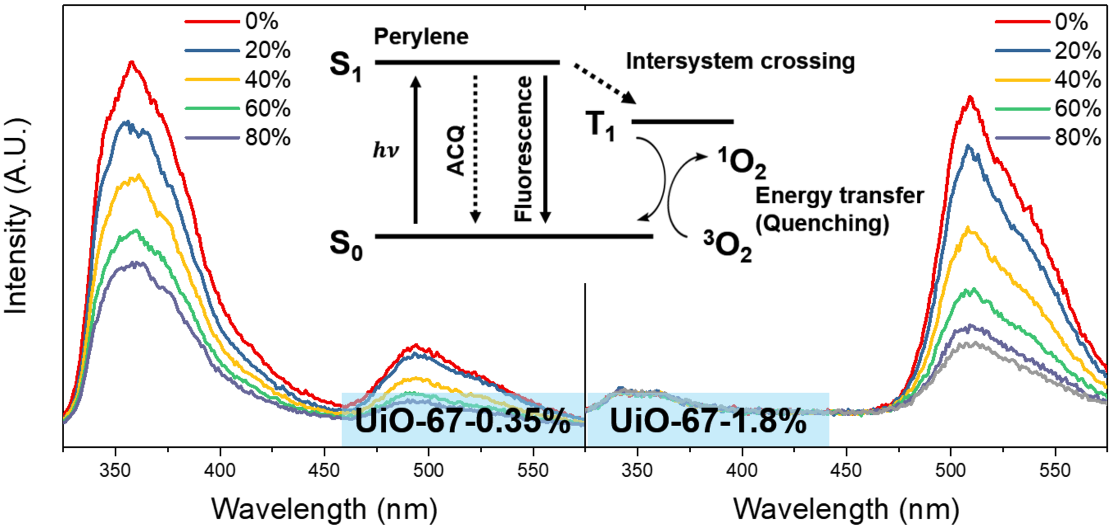

Figure III-12. PL emission spectra of UiO-67-0.35% and UiO-67-1.8% monitored in a mixture of O_2/N_2 gas (excitation wavelength 300 nm). Reprinted with permission from *ACS Appl. Mater. Interfaces.* doi.org/10.1021/acsami.0c05512.

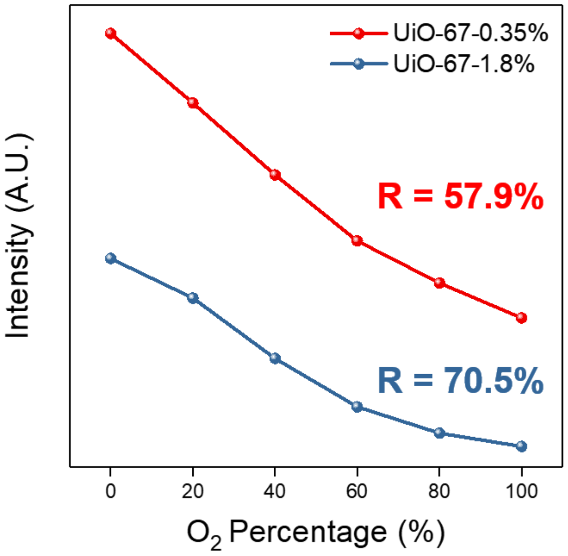

Figure III-13. Oxygen response of monomer (340 nm) and excimer emission (510 nm). Reprinted with permission from *ACS Appl. Mater. Interfaces.* doi.org/10.1021/acsami.0c05512.

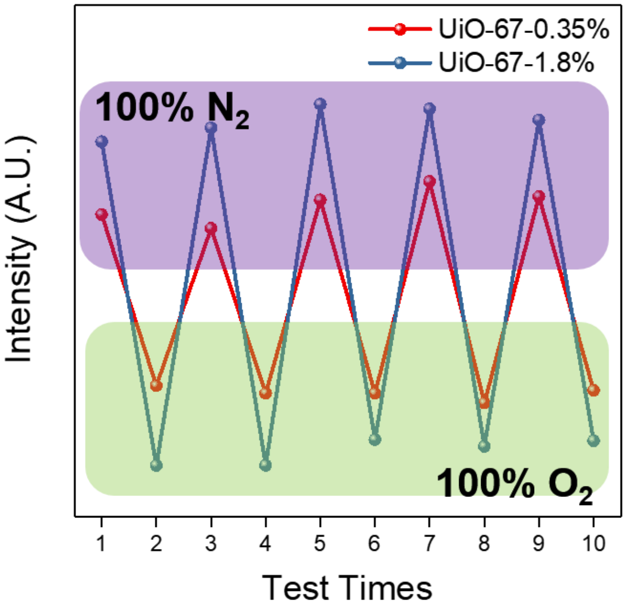

Figure III-14. Reversibility test of UiO-67-1.8% and UiO-67-0.35%. Reprinted with permission from *ACS Appl. Mater. Interfaces.* doi.org/10.1021/acsami.0c05512.

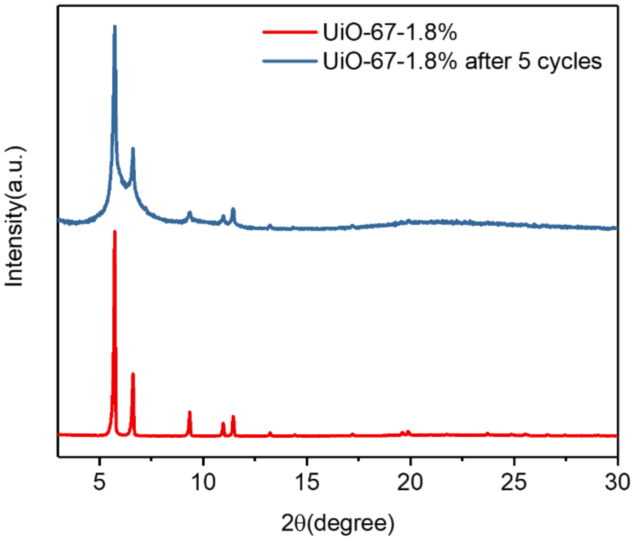

Figure III-15. PXRD patterns of UiO-67-1.8% before (red) and after (red) 5 catalytical cycles. Reprinted with permission from *ACS Appl. Mater. Interfaces.* doi.org/10.1021/acsami.0c05512.

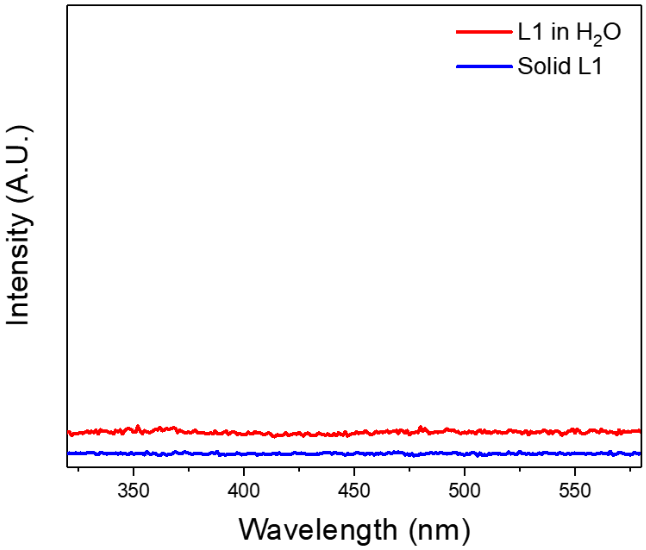

Figure III-16. Fluorescence spectrum of L1 in H_2O (red) and solid state (blue). Both spectrum showed almost none fluorescent signal. Reprinted with permission from *ACS Appl. Mater. Interfaces.* doi.org/10.1021/acsami.0c05512.

3.4 Conclusion

In conclusion, perylene fluorophores were isolated in the solid state through the incorporation of the molecule into a linker in a mixed-linker Zr-MOF. The rigid framework prevented the formation of π-stacked perylene aggregates, minimalizing ACQ affects. Meanwhile, the distance between perylene moieties was able to be tuned through altering the linker ratios. This controls the formation of excimers and self-quenching aggregates, dictating the fluorescence properties. The resulting MOFs were highly porous and the fluorescence could be easily tuned. Both features were employed for the design and optimization of a fluorescent sensor for oxygen gas detection. This body of work demonstrates a successful strategy for the incorporation of isolated aromatic fluorophores in a MOF and can be utilized as a general method for future efforts in preparing fluorophore containing MOFs.

3.5 Instrumentation and Methods

3.5.1 Materials and Instrumentation

All reagents and solvents used in synthetic studies were commercially available and used as supplied without further purification. ^{1}H NMR spectra were obtained utilizing a Mercury 500 MHz spectrometer. Powder X-ray diffraction (PXRD) was carried out on a Bruker D8-Focus Bragg-Brentano X-ray powder diffractometer equipped with a Cu microfocus tube (λ = 1.54178 Å) at 40 kV and 40 mA. Gas sorption measurements were conducted on a Micromeritics ASAP 2020 system. Photon fluorescence spectra were taken on a Shimadzu RF-5301 PC spectrofluorophotometer. UV-Vis spectra were taken on a Shimadzu UV-2450. Steady-state photoluminescence spectra were measured using a Jobin-Yvon-Horiba Fluoromax-4 spectrofluorometer. Qutam yield was measured with an integration sphere accessory on a Jobin-Yvon-Horiba Fluoromax-4 spectrofluorometer. Time-tagged time-correlated single photon counting (TCSPC) was performed using PicoQuant TimeHarp 300 electronics. TCSPC measurements were based on an amplified Ti:Sapphire laser system producing a fundamental beam with 100 fs pulses at 800nm. The Pump beam was produced by frequency doubling fundamental to 402 nm in the BBO nonlinear crystal. All measurements were done at room temperature. Complementary photoluminescence (PL) emission measurements of the samples were performed utilizing an Olympus IX 71 microscope and the samples were excited by a 402 nm laser pulse of 1.5 ps at a repetition rate of 7.5 MHz. The PL emission was then recorded by a MicroHR 140mm spectrometer.

3.5.2 Ligand and MOF Synthesis

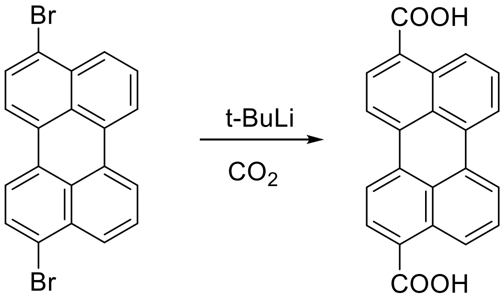

Figure III-17. Synthesis of L1. Reprinted with permission from *ACS Appl. Mater. Interfaces.* doi.org/10.1021/acsami.0c05512.

Synthesis of perylene-3,10-dicarboxylic acid (L1) 3,10-dibromoperylene (32.8 g, 80 mmol) was dissolved in 1 L of dry THF. The solution was cooled to -78 ℃ and t-BuLi (190 ml, 1.7 mol/l, 320 mmol) was added via a syringe. The cooling bath was removed and the mixture was stirred for 3 h during which it was allowed to warm up to 0 ℃. Subsequent addition of dry CO_2 gas was followed by the precipitation of the L1 with 2 M hydrochloric acid. The precipitate was filtered off and thoroughly washed with water.[175]

Synthesis of UiO-67-X%

$ZrCl_4$ (40 mg), H_2-BPDC (20 mg), trifluoroacetic acid (0.1 ml) and DMF (3 mL) were charged in a Pyrex vial. The mixture was heated in a 120 ℃ oven for 24 h. After cooling to room temperature, the colorless crystals of UiO-67 were harvested. For a typical synthesis of UiO-67-1.8%, $ZrCl_4$ (40 mg), H_2-BPDC (19 mg), L1 (1.4 mg), trifluoroacetic acid (0.1 ml) and DMF (3 mL) were mixed and heated.

3.5.3 Single-crystal X-ray Crystallography

The crystals of PCN-700-L1-L2Hcy were taken from the mother liquid without further treatment, transferred to oil, and mounted onto a loop for single crystal X-ray data collection. The diffraction was measured on a Bruker Smart Apex diffractometer equipped with a Cu-Kα radiation (λ = 1.5418 Å) and a low temperature device (100 K). The structures were solved by direct methods using *SHELXS* and refined by full-matrix least-squares on F^2 using *SHELXL* software.[167] All non-hydrogen atoms were refined with anisotropic displacement parameters. The hydrogen atoms on the aromatic rings were located at geometrically calculated positions and refined by riding. The free solvent molecules are highly disordered in MOFs, and attempts to locate and refine the solvent peaks were unsuccessful. The attempts to locate and refine the hemicyanine moiety attaching on the L2 ligand were unsuccessful due to the high level of disorder. The diffused electron densities resulting from these solvent molecules were removed using the SQREEZE routine of PLATON[156]; structures were then refined again using the data generated. Crystal data is summarized in Table III-1.

Table III-1 Crystal data and structure refinements for UiO-67-8%.

Name	UiO-67-8%
Formula	$C_{86.88}H_{48.96}O_{32}Zr_6$ $Zr_6O_4(OH)_4(L1)_{0.64}(L2)_{7.36}$
Formula weight	2150.84
Shape/Color	Blocky/yellow
Crystal System	Cubic
Space Group	Fm-3m
a (Å)	26.7798(11)
b (Å)	26.780
c (Å)	26.780
α (°)	90.000
β (°)	90.000
γ (°)	90.000
V (Å^3)	19205(2)
Z	24
T (K)	100(2)
$d_{\text{calcd.}}$ (g/cm^3)	0.735
μ(mm^{-1})	0.352
F(000)	4136.0
Radiation	MoKα (λ = 0.71073)
2Θ range for data collection/°	4.302 to 54.93

Index ranges	$-28 \le h \le 32$, $-29 \le k \le 34$, $-26 \le l \le 34$
Reflections collected	25702
Independent reflections	1159 [R_{int} = 0.1347, R_{sigma} = 0.0383]
Data/restraints/parameters	1159/78/62
Goodness-of-fit on F^2	1.057
Final R indexes [$I>=2\sigma$ (I)]	R_1 = 0.0583, wR_2 = 0.1630
Final R indexes [all data]	R_1 = 0.0738, wR_2 = 0.1768
Largest diff. peak/hole / e Å^{-3}	1.43/-0.68

3.5.4 N_2 Sorption Isotherms

N_2 adsorption measurements were performed using a Micromeritics ASAP 2020 surface area and pore size analyzer. Before sorption experiments, as-synthesized samples were washed with DMF several times to remove unreacted starting ligands and inorganic species. Afterwards, the crystals were carefully decanted and washed with DMF and acetone several times. Then, the samples were activated under vacuum at 80 °C for 10 h after an acetone exchange. Low-pressure N_2 adsorption isotherms were measured at 77 K in a liquid nitrogen bath. The specific surface areas were determined using the Brunauer-Emmett-Teller model from the N_2 sorption data.

Table III-2. Summary of N_2 isotherms.

	Total N_2 Uptakes (cm^3g^{-1})	**Pore Volume (cm^3g^{-1})**	**BET Surface area (m^2g^{-1})**
UiO-67	**740**	**1.074**	**2120**
UiO-67-1.8%	**735**	**1.060**	**2028**
UiO-67-3.8%	**700**	**1.026**	**1938**
UiO-67-20%	**660**	**0.964**	**1929**
UiO-67-41%	**600**	**0.882**	**1655**
UiO-67-100%	**450**	**0.417**	**1168**

3.5.5 1H NMR Spectroscopy

For ^{1}H NMR spectroscopy, the activated samples (around 5 mg) in 4 mL vials were digested by one drop of D_2SO_4-d_2. About 0.5 mL of DMSO-d_6 was then added to the vial and the mixture was sonicated for 5 minutes before the clear supernatant was extracted for NMR measurements. 1H NMR spectra for L1, L2 and UiO-67-40% are presented below:

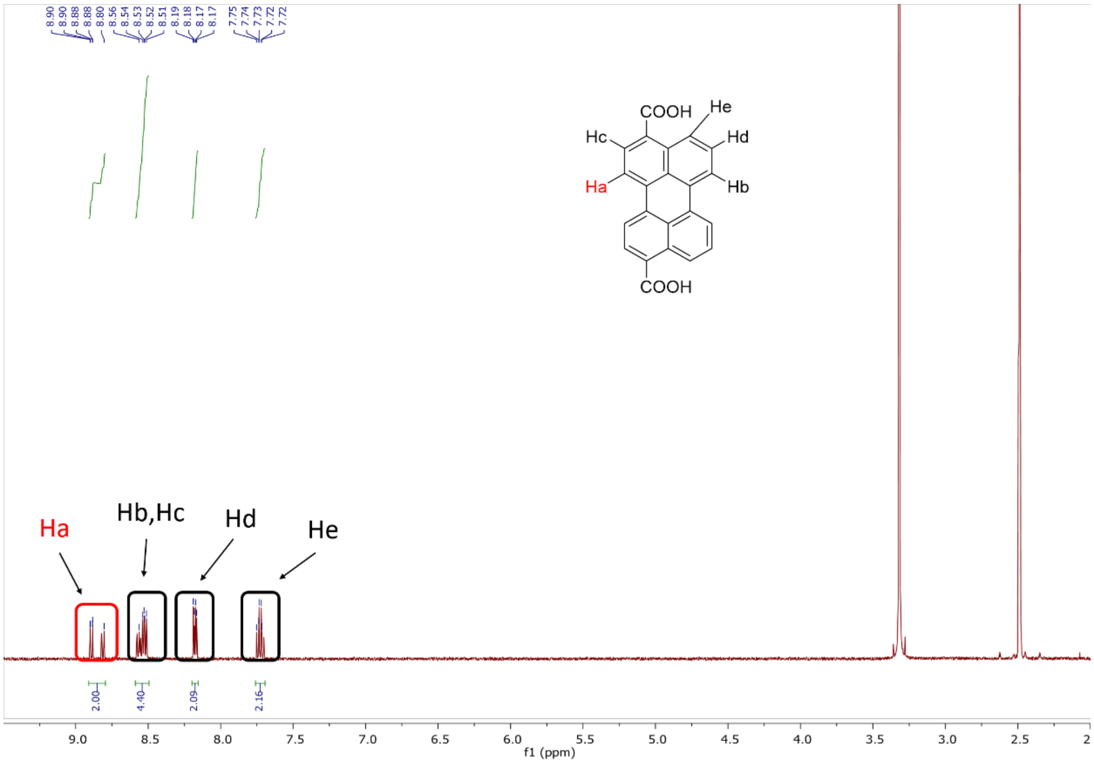

Figure III-18. ^{1}H NMR spectroscopy of L1. Reprinted with permission from *ACS Appl. Mater. Interfaces*. doi.org/10.1021/acsami.0c05512.

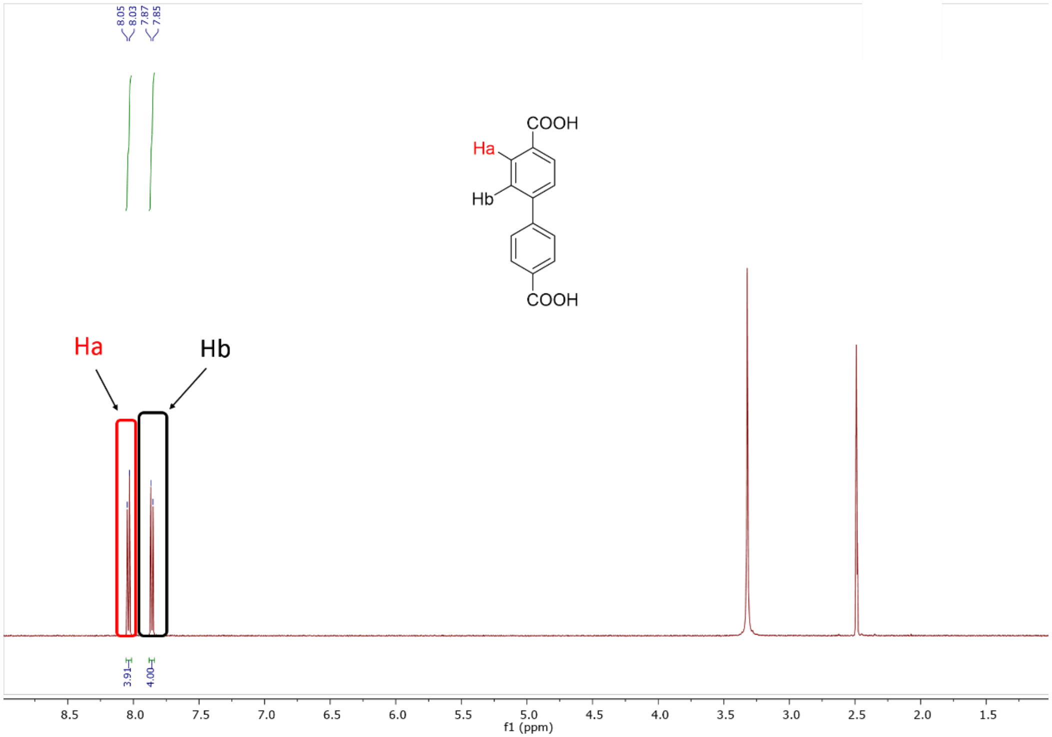

Figure III-19. ^{1}H NMR spectroscopy of L2. Reprinted with permission from *ACS Appl. Mater. Interfaces.* doi.org/10.1021/acsami.0c05512.

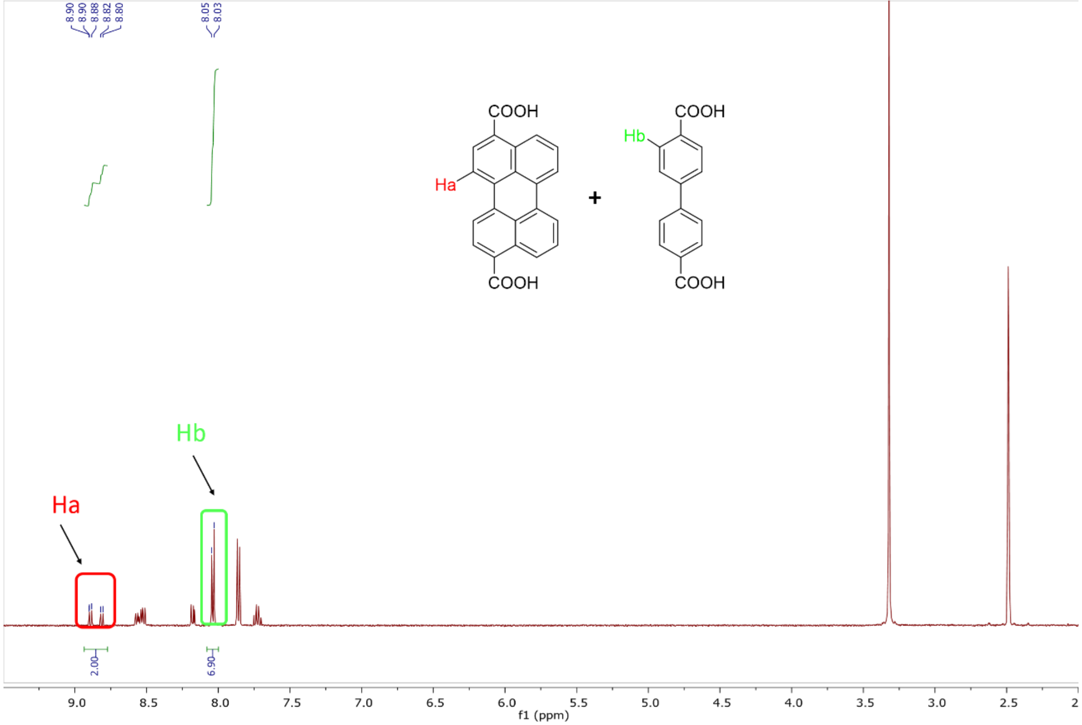

Figure III-20. ^{1}H NMR spectroscopy of UiO-67-40%. Reprinted with permission from *ACS Appl. Mater. Interfaces.* doi.org/10.1021/acsami.0c05512.

3.5.6 Additional Figures

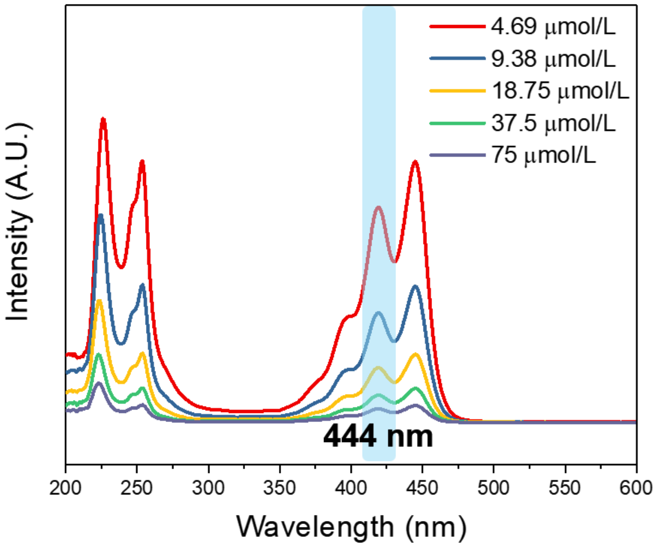

Figure III-21. UV-Vis spectrum of different concentration of L1. Wavelength 444nm was chosen to calculate absorption coefficient. Reprinted with permission from *ACS Appl. Mater. Interfaces.* doi.org/10.1021/acsami.0c05512.

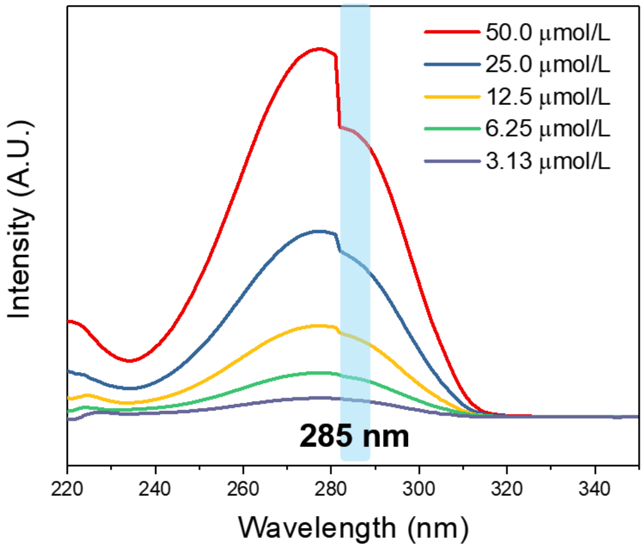

Figure III-22. UV-Vis spectrum of different concentration of L2. Wavelength 285nm was chosen to calculate absorption coefficient where L1 almost has none absorption. Reprinted with permission from *ACS Appl. Mater. Interfaces.* doi.org/10.1021/acsami.0c05512.

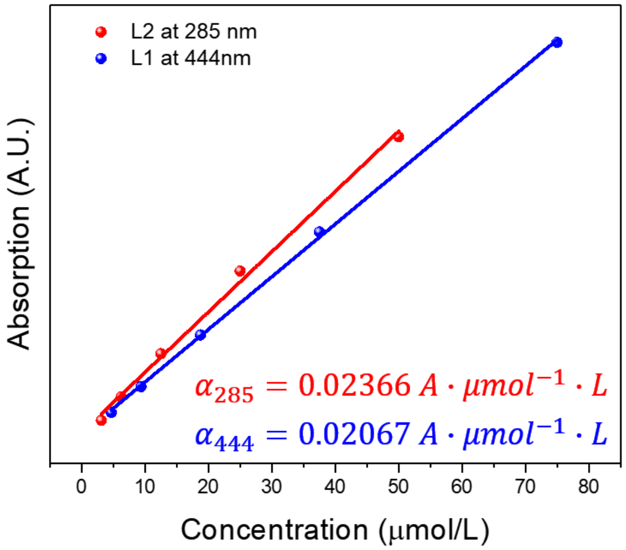

Figure III-23. Standard curve of UV-Vis absorption of L1 and L2. The absorption coefficient of L1 and L2 are 0.02067 and 0.02366 $\mathbf{A \cdot \mu mol^{-1}} \cdot L$, respectively. Reprinted with permission from *ACS Appl. Mater. Interfaces.* doi.org/10.1021/acsami.0c05512.

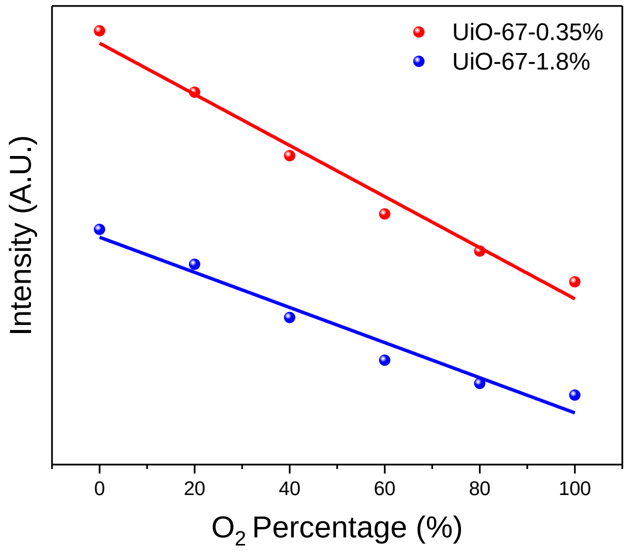

Figure III-24. Correlation of fluorescence intensity of UiO-67-0.35% and UiO-67-1.8%. O_2 percentage is defined as pressure of O_2 over total pressure of O_2 and N_2. Reprinted with permission from *ACS Appl. Mater. Interfaces.* doi.org/10.1021/acsami.0c05512.

Simulation Details

Lattice Monte Carlo technique is used to get the equilibrium structures of mixed linker MOFs. An underlining assumption is that the equilibrium structures are in the energy minimum state. To construct the model, each linker is abstracted as a single lattice point. Therefore, basis sets for unit cell of abstract lattice are [0.5, 0.5, 0.0], [0.0, 0.5, 0.5], [0.5, 0.0, 0.5] with 1/2 length of original lattice. The simulation is carried out in dimensionless units where $k_BT=1$.

Similar to the method adopted by Yaghi and coworkers, pair-wise effective interaction energies are assigned to linkers, which can be tuned to control the spatial preference of L1.[172]

For single linker i, the energy is calculated by summing over all first nearest neighbors, $E_i = \sum_j E_{ij}$ A Monte Carlo move is defined as swapping the position of L1. The configuration accepting probability criteria as follow:

$acc(o \rightarrow n)$=min(1,exp($-\Delta E$)) where ($\Delta E = Enew - Eold$)

Periodic boundary conditions are also adopted with 15 × 15 × 15 supercells. Initially, linkers L1 and L2 are randomly distributed. We assume no interaction between the same type of linker. The interaction energies for different types of clusters are listed in Table S3. Each simulation is repeated 10 times and energy convergence is checked to make sure the system is in the equilibrium state.

The equilibrium system configuration is obtained after Lattice Monte Carlo simulation. This configuration is then mapped to real units in Å for Förster resonance energy transfer calculation. The Förster radius (r0=38 Å) is calculated from the emission spectra and adsorption spectra of L1. The energy transfer efficiency for linker i with linker j is given by:$Eij = \frac{r_0^6}{r_{ij}^6 + r_0^6}$ where rij is the distance between linker i and j. A cutoff distance of 2.5 r0 is adopted since Eij decay rapidly with the increase of rij. Photoluminescence intensity (Ii) of linker i in the system is calculated by multiply over all ij linker pairs within the cutoff distance $Ii = \prod_j (1 - E_{ij})$. Where ij linker pairs are L1-L1 pairs. The final photoluminescence intensity for system is averaged over all linkers.

Table III-3. Effective interaction parameters for L1

System Type	Large Clusters	Small Clusters	Random
EAB	2.0	0.25	0.0

CHAPTER IV

ULTRA-SMALL FACE-CENTERED-CUBIC RU NANOPARTICLES CONFINED WITHIN A POROUSCOORDINATION CAGE FOR DEHYDROGENATION[*]

4.1 Introduction

Ruthenium nanoparticles (Ru NPs) with a face-centered-cubic (fcc) structure exhibit high catalytic activity in a number of reactions. In order to obtain highly crystalline and reactive fcc Ru NPs, we applied an anionic porous coordination cage (PCC-2) to encapsulate them and tune their crystal structures. The cage was assembled with six vertex ligands (V) and eight panel ligands (L), creating a truncated octahedral inner cavity 2.5 nm in diameter. As a result of electrostatic attraction, Ru^{3+} ions were encapsulated within the cavity of PCC-2. By an in situ reduction, metal atoms in the cavity of PCC-2 formed ultra-fine fcc Ru NPs, which were uniform in size. The as-synthesized Ru NPs@PCC-2 composite exhibited record-high catalytic activity in methanolysis of ammonia borane, which is critically important in chemical hydrogen storage. This offers a new way of forming stable metal nanoclusters with ultra-small size and desirable structure within the cavities of a soluble porous material.

---

[*] Reprinted with permission from “Ultra-Small Face-Centered-Cubic Ru Nanoparticles Confined within a Porous Coordination Cage for Dehydrogenation” Fang, Y.; Li, J.; Togo, T.; Jin, F.; Xiao, Z.; Liu, L.; Drake, H.; Lian, X.; Zhou, H.-C. *Chem*, **4**, 555-563. Copyright 2018 Elsevier.

4.2 Background

Metal nanoparticles (M NPs) have been widely used as catalysts as a result of their synthetic accessibility and unique catalytic efficiency.[176-179] Both heterogeneous porous hosts and homogeneous templates have been used as support for M NPs.[180-191] For example, metal-organic frameworks (MOFs),[181] covalent organic frameworks (COFs),[182] porous organic polymers (POPs),[183, 191] organic cages,[185] and ionic liquids[186] are all commonly applied to encapsulate M NPs. As a result, M NP/support composites are widely used for catalysis because the space confinement effect of these supports increases substrate selectivity and improves the catalytic activity as a result of enhanced exposure of active centers. In particular, MOFs have been studied intensively[192-196] because of their structural diversity and tunable porosity. Although MOFs have been attracting great interest in the catalysis field, their secondary building units (SBUs), such as metal-organic polyhedral (MOPs), have rarely been discussed for encapsulating M NPs for catalysis.[197] As a typical SBU for a 3D infinitely connected MOF, MOPs often adopt a discrete (0D) cage-like structure in a highly crystalline form and are usually soluble in solvents, exhibiting completely different properties and functionalities from their original framework. Conventionally, MOPs have been used for host-guest chemistry.[198-201] There are very few examples of using coordination cages to tailor the size of encapsulated NPs.[202-203] We envision that MOPs may have great potential for catalysis because of their cavity confinement effect and facile functionalization.

Face-centered-cubic (fcc) noble-metal (Ru/Rh/Pd) NPs are more active catalytically than other close-packing structures[204] because the more active crystal surfaces are exposed in an fcc structure.[205] Recent research indicates that the rare fcc Ru NPs[206] are more efficient than common hcp Ru NPs, although the data available in the literature only apply to particle sizes > 3.0 nm.[207-208] Presumably, this could be extended to the size range < 3.0 nm. However, obtaining stable noble-metal NPs, particularly fcc Ru NPs, with an ultra-small diameter (<3.0 nm) and in highly crystalline form is very difficult but highly desirable. Although theoretical studies on the catalytic activity of fcc Ru NPs have been presented,[209-210] their synthesis is extremely rare.[211-212] As a result, the reactivity of these M NPs has not yet been explored. It occurred to us that by using highly crystalline MOPs as host to encapsulate M NPs, we would most likely obtain highly crystalline M NPs with tunable structure.

To have high catalytic activity toward designated reactions, a soluble porous material that can strongly interact with and encapsulate M NPs is needed. Here, we propose a suitable candidate of MOP species, namely porous coordination cages (PCCs), for such a purpose. PCCs often have intrinsic micro- and mesopores and are usually soluble in common solvents. Furthermore, specific functional groups can be introduced to the PCCs, intensifying the interaction between the support (PCC) and the M NPs. Encapsulated M NPs may adopt the same geometry as the host cavity, stabilizing their unusual close-packing form and exposing more active crystal surface. In addition, PCCs can prevent agglomeration of the M NPs, making the active surface more accessible during the catalytic process.

4.3 Results and Discussion

4.3.1 Synthesis and Characterization of PCC-2

PCC-2 was designed to have an octahedral cage structure and was assembled by panel ligands, vertex ligands, and metal clusters (Figure IV-1A). It was synthesized by a solvothermal reaction of vertex ligand (Na_4H_4V), panel ligand (H_3L), and $CoCl_2$ at 80 ℃ in methanol for 12 hr. It crystallizes in the rhombohedral $R\bar{3}$ space group as large, purple blocks (Figures IV-1B). Each PCC-2 cage molecule comprises six tetranuclear cobalt clusters $[Co_4(\mu_4\text{-}OH)]$ and six vertex ligands as vertices and eight panel ligands as the faces of an octahedral cage, giving rise to the anionic host $\{[Co_4(\mu_4\text{-}OH)V]_6L_8\}^{30-}$. Each cobalt atom coordinates one sulfonic oxygen, two phenolate oxygen atoms from V, two carboxylate oxygens from L, and a μ4 -OH, leading to an octahedral coordination environment. On the basis of the crystal structure, the longest inner cavity dimension of PCC-2 is 25.1Å (the distance between two μ4-OH of two opposite Co_4 clusters), and the diameter of the sphere in which the octahedral cage is inscribed is 42.2 Å . From the packing diagram of the crystal structure, multiple pores from micro- to meso-range are found in the solid state (Figure IV-1C). A pore-size distribution is given on the basis of the crystal structure of PCC-2 with van derWaals radii; the most populated intermolecular cavity is 14 Å in diameter.

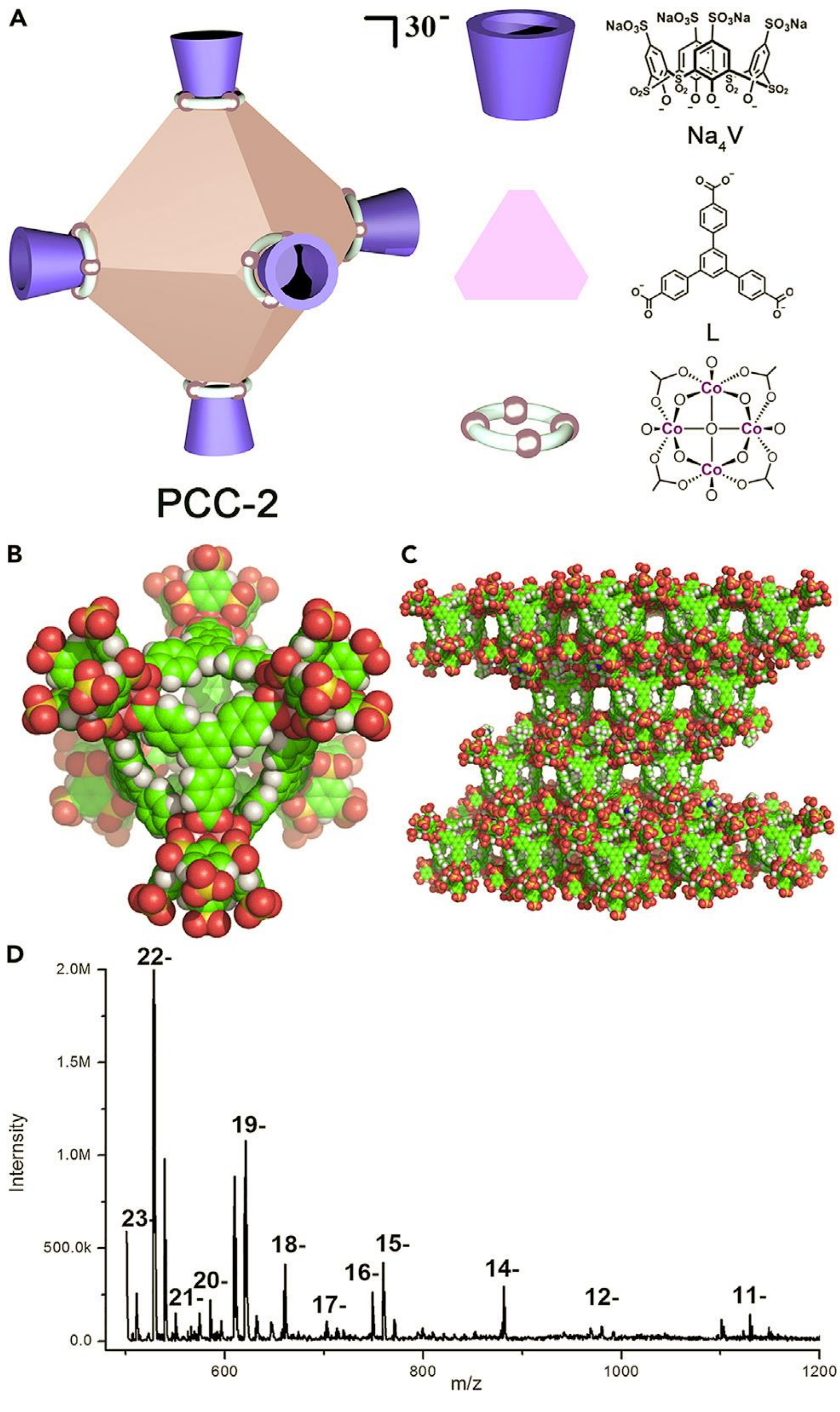

Figure IV-1. Structure of PCC-2 and its components (A), crystal structure of PCC-2 (B), packing diagram of PCC-2 (C), and ESI-mass spectrum of PCC-2 (D). Reprinted with permission from *Chem*, 4, 555-563.

Cationic cages[213-216] and neutral giant cages[217-219] have been reported previously, but PCC-2 represents one of the most negatively charged coordination cages[220] reported to date. For PCC-2, the charge is derived from the following: coordination of the Co^{2+} ions produces a total of 48 positive charges, which are compensated by the phenolate groups from V (24 negative charges) and the carboxylates from L (24 negative charges). However, there are still an additional 24 negative charges from V, as well as 6 negative charges from the anionic μ_4-OH group in the center of the Co_4 cluster. Thus, the overall charge of PCC-2 is 30-. To balance these charges, 24 Na^+ and Et_3NH^+ counter cations are presumed to be placed around the cage. Elemental analysis further confirmed that the formula of the dry sample of PCC-2 is $Na_{24}(Et_3NH)_6\{[Co_4(\mu_4\text{-}OH)V]_6L_8\}^{30-}\cdot 5\ MeOH\cdot 10\ H_2O$. PCC-2 readily dissolves in polar solvents, such as dimethylformanide (DMF) and DMSO. Analysis using electrospray ionization-mass spectrometry (ESI-MS) unambiguously revealed the ionic fragment distribution of negatively charged PCC-2 (Figures IV-1D). Thermogravimetric analysis (TGA) indicated that the cage structure of PCC-2 does not decompose until 240 ℃.

The large cavity coupled with the enormous negative charge of PCC-2 could potentially make it a superior molecular material for exchange, adsorption, and storage of cations. This is further supported by molecular simulations. The crystal structure of the anionic cage of PCC-2 reveals a remarkable helium-accessible void fraction of 74.3%. This corroborates well with the simulated N_2 uptake of 640 m^2/g (STP) at 77 K and P/P0 = 0.94. PCC-2 did not show gas uptake after guest removal, presumably because of blockage of the gas diffusion path by the large amount of counter cations surrounding the cage. Nevertheless, these simulations indicate large accessible voids potentially available for cation exchange, which was further corroborated by the experiments of Ru^{3+} exchange and M NP inclusion.

4.3.2 Preparation and Characterization of Ru NPs@PCC-2

The Ru NPs@PCC-2 homogeneous catalyst was readily prepared as depicted by Figure 2A. An aliquot of DMF (2 mL) was added to a flask containing dry PCC-2 (20 mg, 1.77×10^{-3} mmol) to give a pale-purple transparent solution. The color of the solution became red upon the addition of RuCl3 (0.74 mg, 3.57×10^{-3} mmol). After standing for 30 min to allow cation exchange to complete, the mixture was subsequently reduced with a DMF solution of sodium borohydride (0.9 mg, 2.37×10^{-2} mmol, sonication, 25 °C). The solution immediately darkened without precipitation (Figure IV-2A), indicating efficient Ru(III) reduction and further stabilization of the resulting Ru NPs by PCC-2. In a control experiment, Ru(III) reduction in the absence of PCC-2 resulted in immediate precipitation of a black solid, indicative of MNP aggregation (Figure IV-3). The conversion of Ru(III) to Ru(0) could be monitored by absorption spectroscopy (Figure IV-2B). The disappearance of the absorption band of Ru(III) at 432 nm upon the addition of $NaBH_4$ indicates that the metal ions were reduced completely.[221-222] The as-synthesized Ru NPs@PCC-2 did not precipitate even after standing for 6 months in ambient air. The solid form of Ru NPs@PCC-2 was prepared by the direct addition of a large amount of MeCN to the DMF solution of Ru NPs@PCC-2 to force the precipitation of a black solid, which was collected through filtration. The Ru NPs@PCC-2 solid could be re-dissolved in DMF.

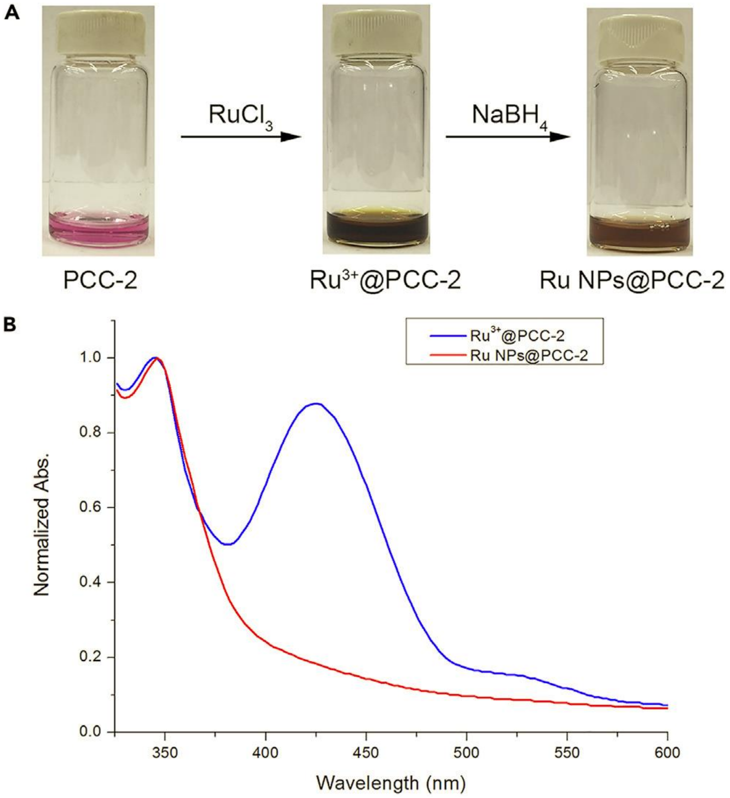

Figure IV-2. Preparation of Ru nanoparticles by PCC-2 (A) and absorption spectra of PCC-2 after the addition of a Ru salt and NaBH4 (B). Reprinted with permission from *Chem*, 4, 555-563.

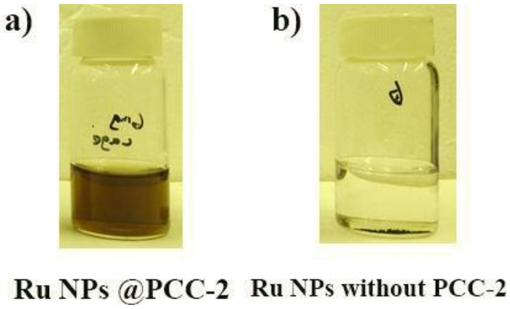

Figure IV-3. Images of Ru NPs a) with and b) without PCC-2 as stabilizer. Reprinted with permission from *Chem*, 4, 555-563.

The as-synthesized Ru NPs@PCC-2 was further analyzed by transmission electron microscopy (TEM). In one experiment, the prepared solution was drop casted onto carbon-coated copper grids and allowed to dry before the measurements. In another run, the solid sample was ground and then directly put onto the carbon- coated copper grids. The images for Ru NPs@PCC-2 from both attempts show the formation of uniform and well-dispersed Ru NPs (Figures IV-4A and IV-4B). The images of the control sample in the absence of PCC-2 show bulky (>10.0 nm) and aggregated NPs (Figure IV-5). The narrow size distribution of Ru NPs@PCC-2 shows a main peak at 2.5 nm (Figures IV-4C and IV-6), which is almost identical to the size of the internal cavity of the cage (2.5 nm), indicating the size limiting effect for M NPs by PCC-2. High-resolution TEM (HRTEM) images (Figures IV-4D and IV-7) clearly show that Ru NPs@PCC-2 adopted a truncated octahedral fcc structure with the {111} and {100} planes exposed.[223-224] Fast Fourier transform (FFT) also confirmed the fcc structure as shown in Figure IV-4E, giving an electron diffraction pattern consistent with an fcc crystal viewed along the [110] direction. This is the first direct observation of an fcc single crystal of a truncated octahedral Ru NP < 3 nm in size.[225] As mentioned before, fcc Ru NPs have rarely been synthesized.[211-212] This is also the first instance where a 2.5 nm single crystalline fcc Ru NPs has been encapsulated within a molecular polyhedron. Good matching of the shapes and sizes of Ru NPs and PCC-2 strongly indicates that PCC-2 is capable of regulating the size and shape of included nanoparticles. Powder X-ray diffraction was also performed to confirm that the crystal form of Ru NPs@PCC-2 was fcc (Figure IV-8). Energy dispersive X-ray spectroscopy mapping also confirmed that the Ru NPs (Ru) were entrapped within the cage (Figures IV-9 and IV-10). X-ray photoelectron spectroscopy revealed that a Ru $3d_{5/2}$ peak at 279.8 eV corresponded well with the $3d_{5/2}$ and $3d_{3/2}$ lines of elemental Ru(0), indicating that the majority of Ru NPs encapsulated within PCC-2 were present as metallic Ru (Figure IV-11).[226]

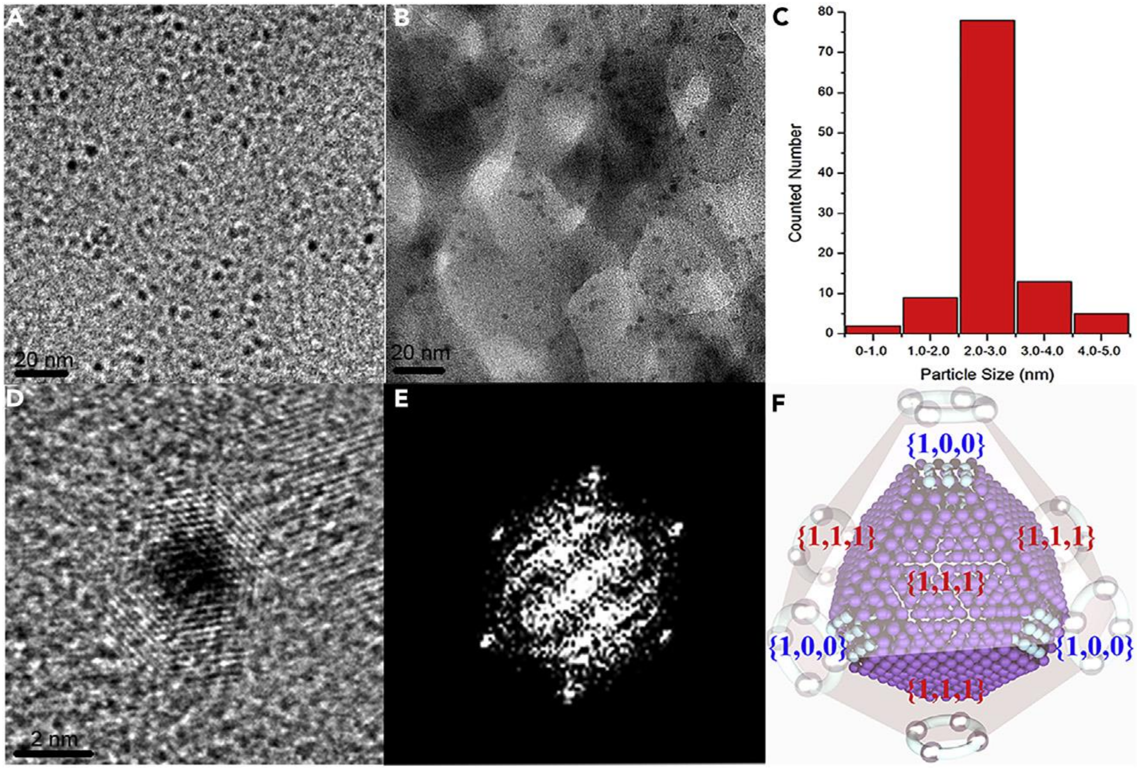

Figure IV-4. TEM images of Ru NPs@PCC-2 in both solution (A) and solid state (B), size distribution of Ru NPs@PCC-2 (C), HRTEM image of an individual Ru NPs@PCC-2 (D), FFT of d (view direction [110]) (E), and truncated octahedral fcc Ru NPs encapsulated within PCC-2 (V of PCC-2 was omitted for clarity) (F). Scale bars: 20 nm (A and B) and 2 nm (D). Reprinted with permission from *Chem*, 4, 555-563.

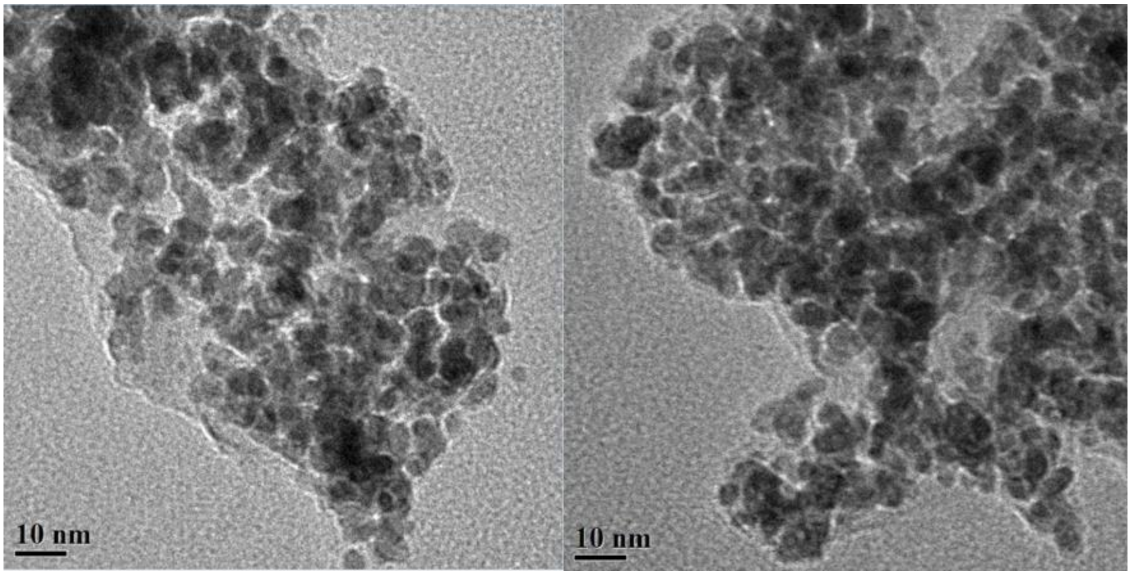

Figure IV-5. TEM image of Ru NPs in the absence of PCC-2. Reprinted with permission from *Chem*, 4, 555-563.

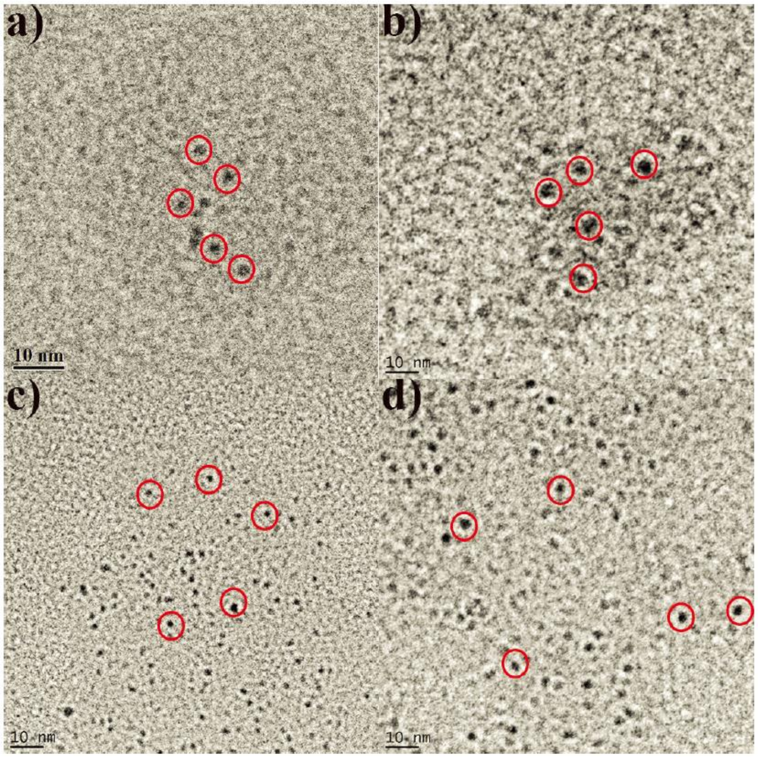

Figure IV-6. TEM image of Ru NPs@PCC-2. Reprinted with permission from *Chem*, 4, 555-563.

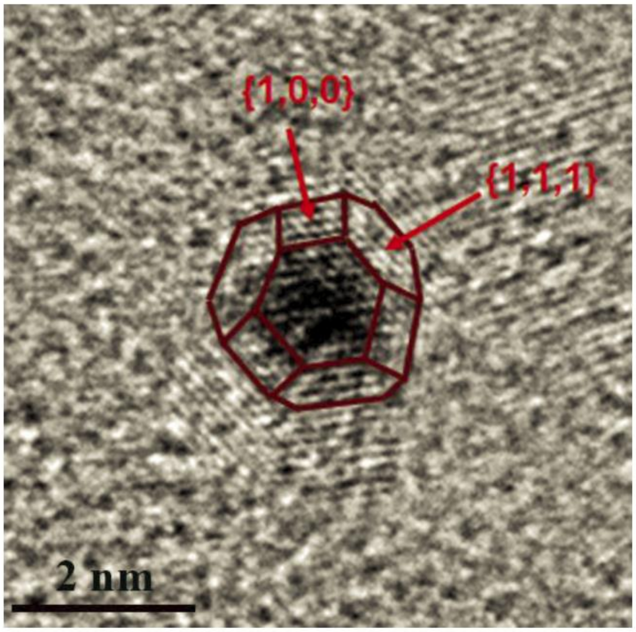

Figure IV-7. TEM image of individual Ru NPs@PCC-2 with labeled crystal surfaces. Reprinted with permission from *Chem*, 4, 555-563.

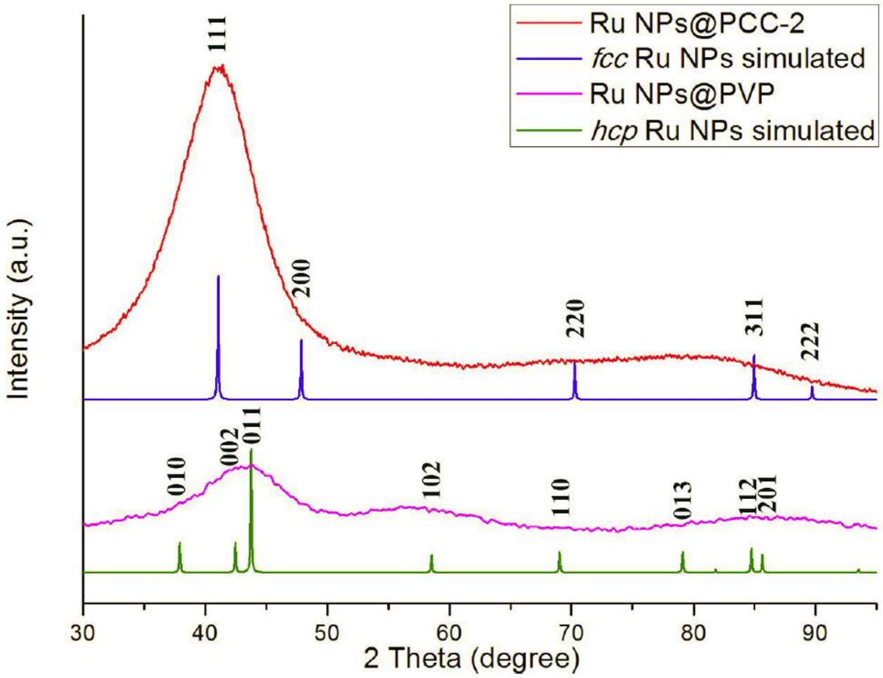

Figure IV-8. PXRD of experimental Ru NPs@PCC-2, simulated Ru fcc, experimental Ru NPs@PVP, and simulated Ru hcp. Reprinted with permission from *Chem*, 4, 555-563.

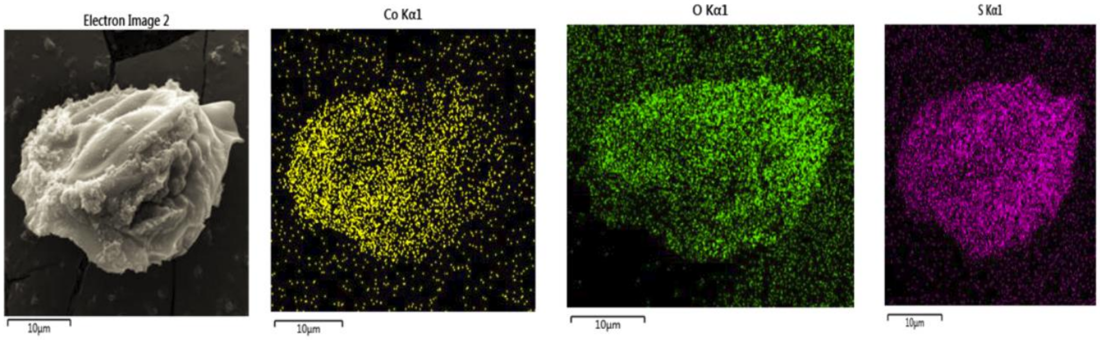

Figure IV-9. SEM-EDS analysis of PCC-2. EDS analysis of PCC-2 showing only C, Co, S and O elements. Reprinted with permission from *Chem*, 4, 555-563.

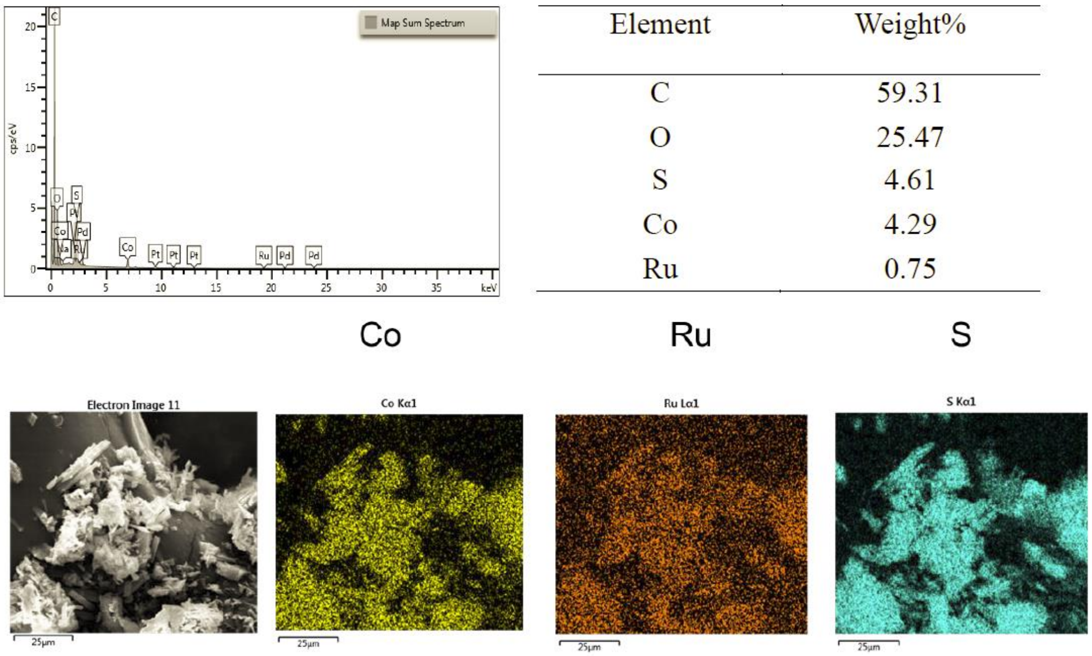

Element	Weight%
C	59.31
O	25.47
S	4.61
Co	4.29
Ru	0.75

Figure IV-10. SEM-EDS analysis of Ru NPs@PCC-2. EDS analysis of Ru NPs@PCC-2 showing C, Co, Ru, O and S elements. The calculated Co:Ru ratio is 10:1, and the experimental ratio is 9:1. Reprinted with permission from *Chem*, 4, 555-563.

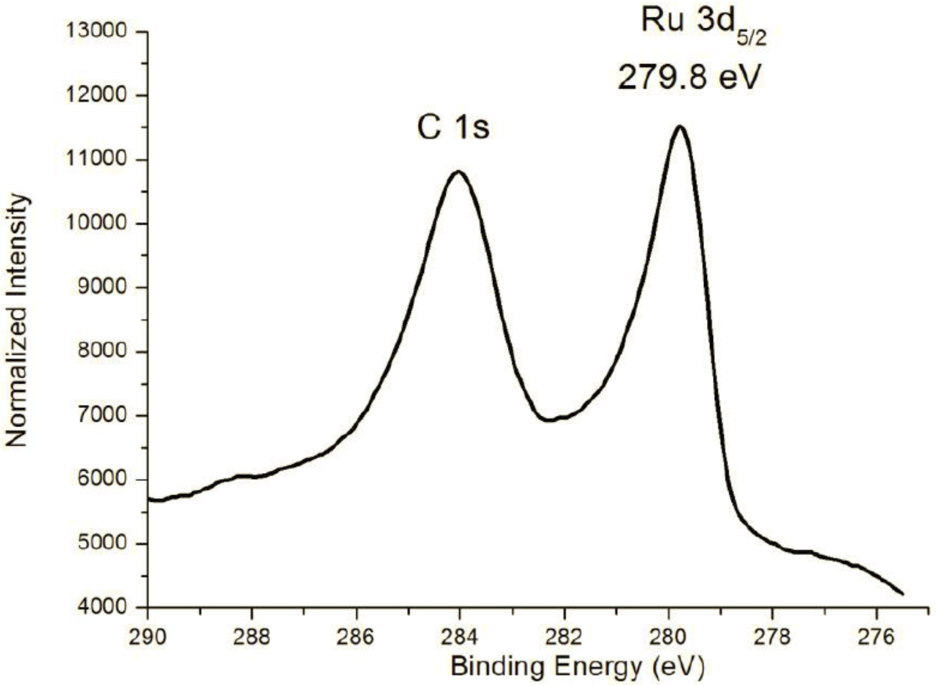

Figure IV-11. XPS spectrum of Ru NPs@PCC-2. The main peak is 279.8 eV belong to Ru $3d_{5/2}$ (metallic Ru species). Reprinted with permission from *Chem*, 4, 555-563.

4.3.3 Dehydrogenation of Ammonia Borane

Because Ru NPs@PCC-2 has a rare fcc structure and more active crystal surfaces, we were curious about the stability and reactivity of the encapsulated NPs. Because of its high hydrogen content (19.6 wt %), high stability, and non-toxicity, ammonia borane ($NH_3{\cdot}BH_3$ [AB]) is widely used as a chemical hydrogen source.[227] The hydrogen can be readily released through hydrolysis or methanolysis of AB with full control and at low cost. Compared with the hydrolysis reaction, the merits of methanolysis are as follows: a single gaseous product (H_2), recoverable by-products, and the possibilities of handling at low temperatures (<0 ℃). In our study, the methanolysis of AB (Equation IV-1) was used as a test reaction for evaluating the catalytic activity of Ru NPs@PCC-2. The reaction was initiated by injection of a DMF/MeOH solution of Ru NPs@PCC-2 into a reaction flask containing AB powder, which was vigorously stirred at room temperature (298 K). The H_2 generated from the methanolysis of AB was collected in a buret, with which the volume of H_2 was monitored. Figure IV-12 shows the generation of H_2 from AB in the presence of the Ru NPs@PCC-2 catalyst. Under our optimized conditions, the Ru NPs@PCC-2 catalyst with a Ru/PCC molar ratio loading of 2/1 showed the highest catalytic activity, and the reaction could be completed (H_2/AB = 3.0) within 4.5 min (Ru/AB = 3.5/1,000) at 298 K (Figure 4), giving a turnover frequency (TOF) of 304.4 mol of H_2 per mol of Ru per min. Notably, this is the best catalytic activity ever reported for the methanolysis of AB.[228] Previously, Xu and coworkers achieved the highest TOF of methanolysis of AB (TOF = 215 min^{-1}) by using Rh/CC3-R-homo.[185] Such a remarkable performance was the result of the ultrasmall metal nanocluster catalyst and the active fcc crystal faces. Furthermore, the anionic and soluble PCC-2 played a critical role in encapsulating, stabilizing, homogenizing, and distributing the metal nanoclusters by regulating the size and the atomic arrangement of the encapsulated NPs. The homogeneous catalyst Ru NPs@PCC-2 can also be reused at least five times without a significant loss of activity (Figure IV-13).

Equation IV-1. Reaction of Methanolysis of Ammonia Borane

$$NH_3{\cdot}BH_3 + 4\ CH_3OH \xrightarrow[\text{rt}]{\text{Ru NPs}} NH_4{\cdot}B(OCH_3)_4 + 3\ H_2$$

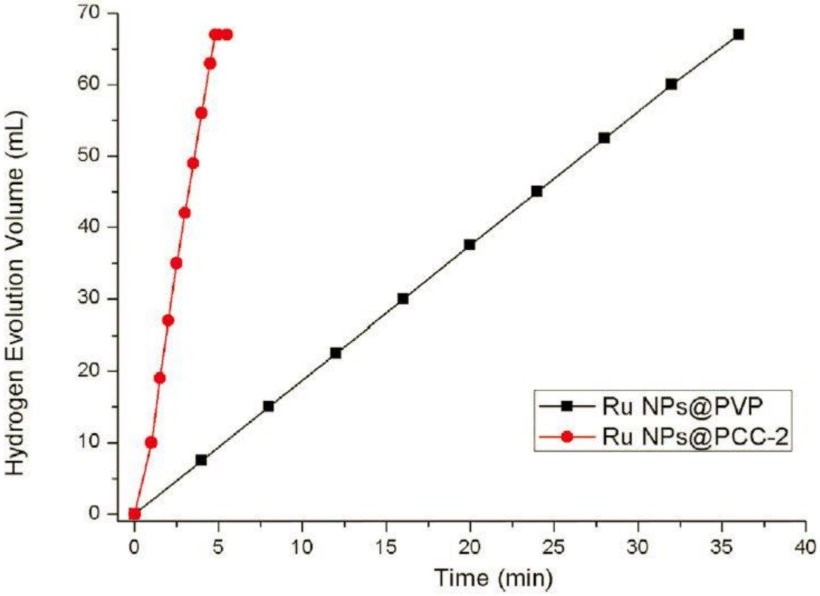

Figure IV-12. Hydrogen generation of AB catalyzed by Ru NPs@PCC-2 (red plot) and by Ru NPs@PVP (black plot). Reprinted with permission from *Chem*, 4, 555-563.

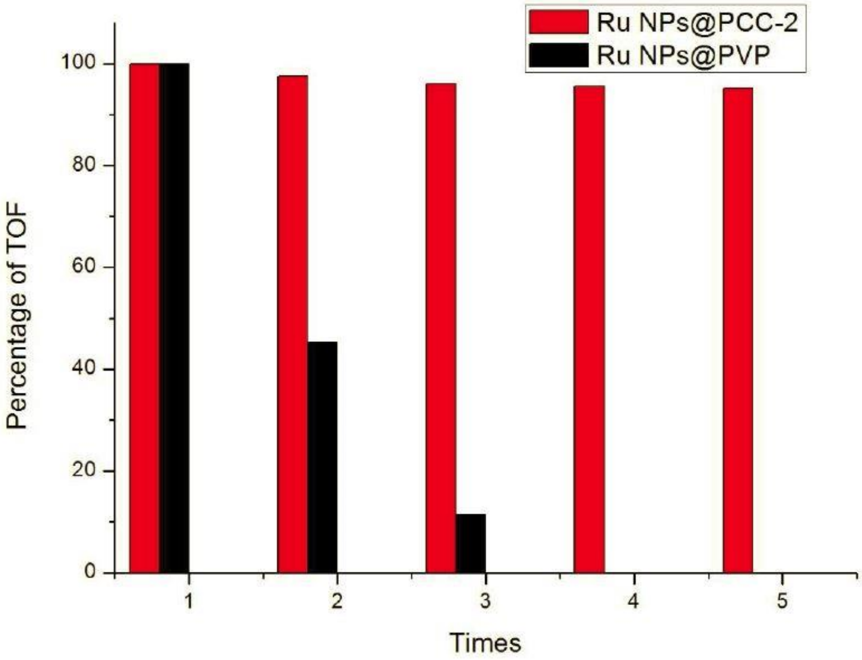

Figure IV-13. Recyclability test of Ru NPs@PCC-2 and Ru NPs@PVP. Reprinted with permission from *Chem*, 4, 555-563.

To further compare the reaction rates with those of the cage components (common homogeneous and heterogeneous catalysts), we conducted control experiments (Table IV-1). Both cage components, Na_4H_4V and H_3L, failed to stabilize the metal nanocluster, as indicated by the formation of black aggregation after the addition of reductant (Figure IV-14). Thus, the catalytic performance was considerably low for components Na_4H_4V and H_3L with TOFs of 4.2 and 3.4, respectively. Conventional surfactant polyvinylpyrrolidone (PVP) could indeed stabilize the as-formed M NPs, but it still showed poor catalytic activity (TOF = 38.1 for Ru NPs@PVP). Finally, a commercially available heterogeneous catalyst Pd@C showed the lowest catalytic activity (TOF = 2.0; Table 1). After the reaction, the Ru NPs@PVP sample became aggregated, whereas the Ru NPs@PCC-2 sample maintained a highly dispersed form (Figure IV-15). Surprisingly, the PCC-2 cage remained intact after the catalytic reaction. These control experiments strongly indicate that (1) PCC-2 served as an ion reservoir to attract the metal ion, thus stabilizing the encapsulated M NPs formed in situ; (2) the uniform 2.5 nm hydrophobic cavity regulated the size of the encapsulated M NPs; (3) the unique truncated octahedral cavity of PCC-2 regulated the crystal structure of the encapsulated Ru NPs to an unusual fcc arrangement in a single-crystal form; (4) the anionic property of PCC-2 prevented the encapsulated Ru NPs from agglomeration as a result of charge repulsion; (5) the high porosity of PCC-2 made the encapsulated Ru NPs highly accessible; and (6) the Ru NPs@PCC-2 composite exhibited record-high catalytic activity for methanolysis of AB.

Table IV-1. Catalytic Performance of PCC-2 and Other Compounds.

Catalyste	Reaction Time (min)	Ru/AB Molar Ratio (%)	Ru/Support Molar Ratio	H_2/AB Molar Ratio	TOF (min^{-1})
Ru NPs@PCC-2	4.5	0.35	2/1	3/1	304.4
Rh/CC3-R-homo	0.7	2.0	-[a]	3/1	215.3
Ru NPs@PVP	36	0.35	2/1	3/1	38.1
Ru NPs + Na_4H_4V	326	0.35	2/1	3/1	4.2
Ru NPs + H_3L	403	*0.35*	2/1	3/1	*3.4*
Pd/C	-	2.0	-[b]	3/1	2.0

Abbreviations are as follows: Ru NP, ruthenium nanoparticle; PCC-2, porous coordination cage 2; Rh, rhodium nanoparticle; CC3-R-homo, cycloimine cage-3-R homogeneous; and PVP, polyvinylpyrrolidone.

[a] 2.4 wt % loading.

[b] 10 wt % loading.

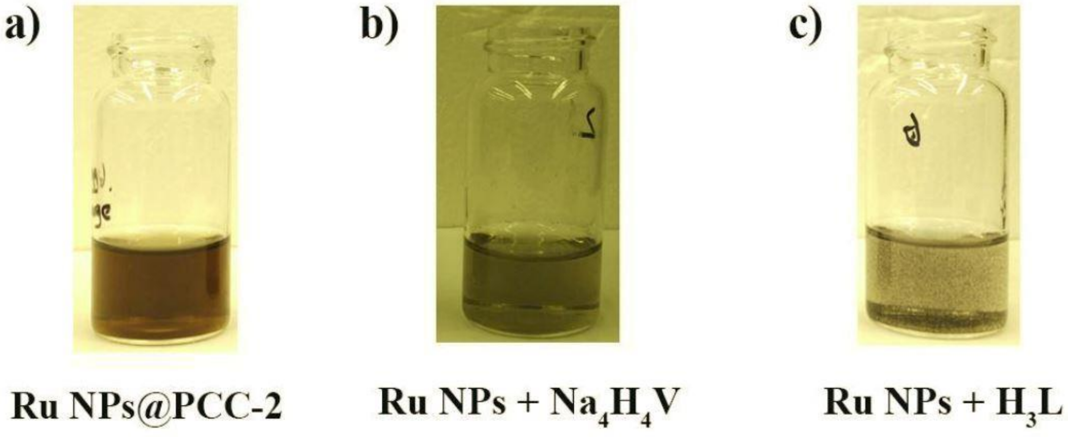

Figure IV-14. Images of a) Ru NPs@PCC-2, and Ru NPs physically mixed with b) compound Na_4H_4V and c) H_3L. Reprinted with permission from *Chem*, 4, 555-563.

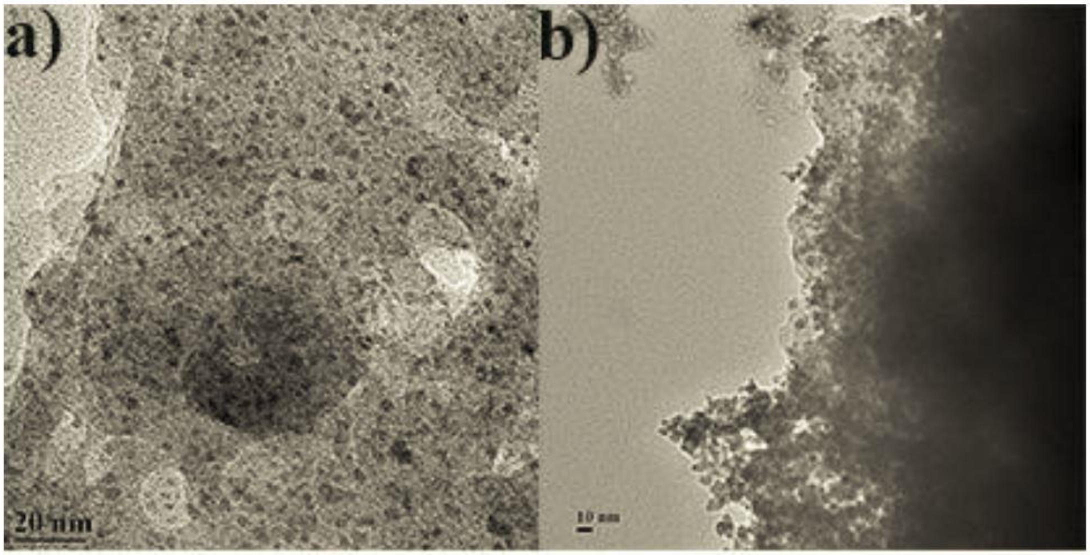

Ru NPs @PCC-2 Ru NPs @PVP

Figure IV-15. TEM images comparison between a) Ru NPs@PCC-2 and b) Ru NPs@PVP after 5 times of reactions. Reprinted with permission from *Chem*, 4, 555-563.

4.4 Conclusion

In conclusion, a highly negatively charged (30^-) porous coordination cage (PCC-2) was synthesized and utilized to encapsulate Ru NPs to form a Ru NPs@PCC-2 composite, which showed enormously enhanced catalytic activity. Through electrostatic interactions and a cavity confinement effect, PCC-2 encapsulated Ru precursor and regulated the sizes and structures of the resulting NPs, leading to encapsulated NPs uniform in size with an unusual fcc crystal structure. The Ru NPs@PCC-2 composite exhibited the highest catalytic activity for methanolysis reactions for AB, which may be ascribed to the highly active fcc structure and the ultra-small diameter of the encapsulated NPs. This study has demonstrated not only the feasibility of constructing a highly charged

PCC but also a promising strategy for encapsulating M NPs of uniform size and desired structure for highly active catalysis.

4.5 Instrumentation and Methods

4.5.1 Materials and instrumentation

p-tert-butylsulfonylcalix[4]arene (H_4TBSC), $CoCl_2$, $RuCl_3$, $NaBH_4$, N,Ndimethylformamide (DMF), acetone, ethanol were purchased from TCI USA and Sigma- Aldrich. All commercial chemicals were used without further purification unless otherwise mentioned. Compound Na_4H_4V was synthesized by using H_4TBSC according to literature reported procedures.[229] Single crystal X-ray diffraction was carried out on a Bruker Quest diffractometer equipped with a Mo Kα sealed-tube X-ray source (graphite radiation monochromator, $\lambda = 0.71073$ nm) and a low temperature device (110 K). TEM was performed on a FEI Tecnai G2 F20 ST microscope at 200 kV equipped with a field emission gun. Thermogravimetric analyses (TGA) were carried out on a METTLER TOLEDO TGA/DSC 1 thermogravimetric analyzer from room temperature to 500 ℃ at a ramp rate of 2 ℃/min in flowing nitrogen atmosphere. Gas sorption measurements were conducted at different temperatures using a Micrometritics ASAP 2020 system. Nuclear magnetic resonance (NMR) data were collected on a Mercury 300 spectrometer. ESI Mass was conduct by Applied Biosystems PE SCIEX QSTAR system. The electronic absorption spectra were measured on a Hitachi U-4100 UV-Vis-NIR spectrophotometer. Steady-state luminescence spectra were acquired with a PTI Quanta Master Model QM-4 scanning spectrofluorometer equipped with a 75-watt xenon lamp, emission and excitation monochromators, excitation correction unit, and a PMT detector. The excitation and emission spectra have been corrected for the wavelength-dependent lamp intensity and detector response, respectively. Energy-dispersive X-ray spectroscopy (EDS) was measured using a JEOL JSM-7500F field emission SEM. X-ray Photoelectron Spectroscopy (XPS) was measured using Omicron’s DAR 400 with dual Mg/Al X-ray source.

4.5.2 The self-assembly of PCC-2.

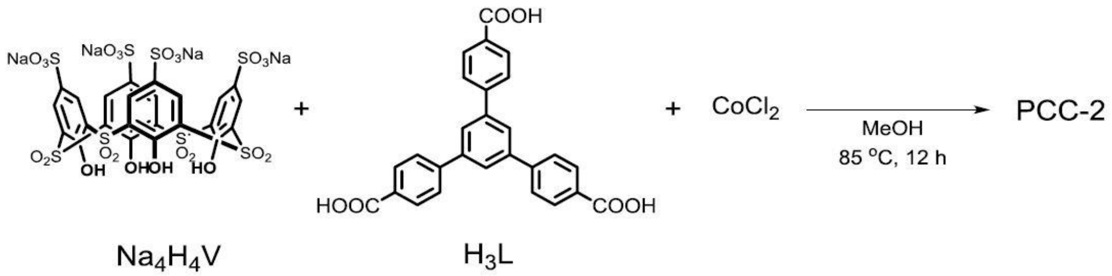

Figure IV-16. Synthetic procedures for PCC-2. Reprinted with permission from *Chem,* 4, 555-563.

Na_4H_4V (14.5 mg, 0.014 mmol) and H_3L (14.5 mg, 0.033 mmol) and $CoCl_2$ (13.3 mg, 0.103 mmol) were suspended in 2 mL MeOH. The mixture was heated up at 85 ^oC in an oven for 12 h. After cooling down to ambient temperature, big purple crystals were collected and washed by methanol. Yield of PCC-2 is about 95% (according to H_4V_1). Elemental analysis: calculated (%) for $Na_{30}(Et_3NH)_6$ $[C_{360}H_{222}S_{48}O_{198}Co_{24}]$ ·5 MeOH ·10 H_2O, C 39.56, H 2.96, N 0.69, S 12.64; found (%):C 39.28, H 2.92, N 0.70 S 12.86. ESI-MS: 510.73 (232-), 528.15 (22-), 539.09 (22-), 550.12 (21-), 574.11 (21-), 585.09 (20-), 609.99 (19-), 619.98 (19-), 631.94 (19-), 646.49 (18-), 660.50 (18-), 702.87 (17-), 748.47 (16-), 760.56 (15-), 772.88 (15-), 881.69 (14-), 971.50 (12-), 979.02 (12-), 990.11 (12-), 1102.56 (11-), 1131.84 (11-).

4.5.3 Preparation of Nanoparticle

A solution of DMF (2 mL) was added to a flask containing dried PCC-2 (20 mg, 0.00177 mmol, MW= 11310.12) to give a pale purple transparent solution. Then, $RuCl_3$ (0.74 mg, 0.00357 mmol) was added to furnish a dark red solution. After aging for 30 min, a 1 mL of DMF solution of sodium borohydride ($NaBH_4$, 0.9 mg/mL) was added to the mixture and sonicated. The solution immediately changed to brown color. The solution is homogenous and will not precipitate after 6 months. After adding excess amount of acetonitrile, the solid state PCC-2 stabilized nanoparticles can be isolated by filtration. The homogenous solution was put into 1 mm cell for UV-Vis measurement. For comparison, a DMF solution of $NaBH_4$ was added to DMF solution of $RuCl_3$. A black precipitate was formed immediately. Also, when cage components, compound Na_4H_4V or H_3L presents, there are still black precipitate can be observed.

4.5.4 Hydrogen generation reaction and TOF calculation

Procedures for the methanolysis of ammonia borane by nanoparticle catalyst: A solution of DMF (2 mL) was added to a flask containing dried PCC-2 (20 mg, 0.00177 mmol, MW= 11310.12) to give a pale purple solution. Then, $RuCl_3$ (0.74 mg, 0.00357 mmol) was added to furnish a dark red solution. After aging for 30 min, a 1 mL of DMF solution of sodium borohydride ($NaBH_4$, 0.9 mg/mL) was added to the mixture and sonicated. The solution immediately changed to brown color. This homogenous solution is as-synthesized Ru NPs@PCC-2 catalyst. A gas burette filled with water was connected to the reaction flask to measure the volume of hydrogen. The reaction started when 1 mL methanol solution of ammonia borane (30 mg, 1 mmol) were injected into the flask by syringe. The volume of the evolved hydrogen gas was monitored by recording the displacement of water in the gas burette. The reaction was completed when there was no more gas generated. And the byproduct was purified by column and characterized by NMR (Fig. S15).

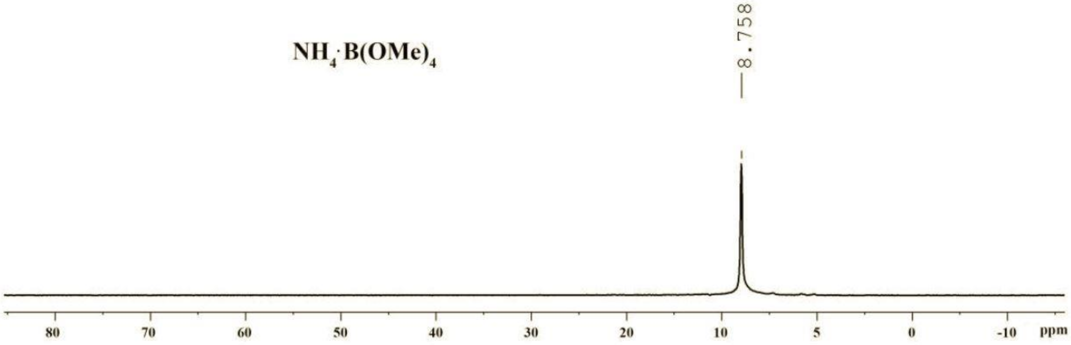

Figure IV-17. ^{11}B NMR of ammonium tetramethoxy borate [$NH_4B(OCH_3)_4$]. Solvent: d_4-MeOH. Reprinted with permission from *Chem*, 4, 555-563.

For the control experiments, Ru NPs@PCC-2 was replaced by as-synthesized Ru NPs@PVP, or cage components H_4L_1 and H_3L_2. Then we conduct the reaction followed by exact the same procedures as Ru NPs@PCC-2's case. The turnover frequency (TOF) is based on the amount of Ru atoms, which was calculated from the equation below:

$$\mathrm{TOF} = \frac{V_{H_2}}{V_m \cdot n_{Ru} \cdot t}$$

Where V_{H_2} is the total volume of generated H_2, V_{H_2} is calculated by Patm/RT (Patm is 101.325 kPa, R is 8.3145 $m^3 \cdot Pa \cdot mol^{-1} \cdot K^{-1}$, and T is 298 K), n_{Ru} is the total mole number of Ru atoms in catalyst and t is the completion time of the reaction in minute.

Recyclability tests were done by five-time injection of ammonia borane methanol solution to the Ru NPs@PCC-2 and Ru NPs@PVP homogenous catalyst solution. The TOFs of each injection are calculated by each reaction time and the volume of hydrogen generated for each time.

CHAPTER V

CONCLUSIONS

5.1 Stepwise Assembly of "Turn-On" Fluorescent Sensors in Multicomponent Metal–Organic Frameworks for in vitro Cyanide Detection

PCN-700-L1-L2Hcy was successfully synthesized in chapter II. The integration of an anthracene-based fluorophore and a hemicyanine-based CN^- responsive moiety within a multicomponent MOF successfully generated a highly selective and sensitive "turn-on" fluorescent sensor. The optimized MOF-probe was shown to have a CN^- detection limit as low as 0.05 μM, much lower than similar probe reported in the literature (0.2 μM), demonstrating its feasibility for CN- detection in drinking water and in vitro detection. The better performance can be attributed to efficient energy transfer between the fluorophore and the recognition moiety through the close proximity (less than 2 nm) of the two components within a periodic lattice via fluorescence resonance energy transfer (FRET). When compared to the molecular probe equivalent, the MOF-based probe allowed for the optimization of the analyte sensitivity by tuning the ratio between the fluorophore and the recognition moiety. The ratio will not be restricted to integral anymore, with linker-installation method, more precise ratio can be achieved. In addition, the size of the MOF particles could be tuned to the nanometer scale, extending the application of this material into in vitro CN^- detection. Chapter II highlights the capability of MOFs for applications in the assembly of energy-transfer based sensors. In the future, multiple cooperative moieties could be involved in to same MOF structure, creating new hybrid materials.

5.2 Fluorescence Enhancement by Isolating Perylene in Solid State Via Metal-Organic Frameworks

In chapter III, perylene fluorophores were successfully isolated in the solid state through the incorporation of the molecule into a linker in a mixed-linker Zr-MOF. The rigid framework prevented the formation of π-stacked perylene aggregates, which minimalizing aggregation-caused quenching (ACQ) affects. Meanwhile, the distance between perylene moieties was able to be tuned through altering the linker ratios, which controls the formation of excimers and self-quenching aggregates, dictating the fluorescence properties. The chapter III demonstrates a successful strategy for the incorporation of isolated aromatic fluorophores in a MOF and can be utilized as a general method for future efforts in preparing fluorophore containing MOFs. In the future, this strategy can be applied in solving ACQ effects of metal clusters. Similar to ligands, metal clusters in MOF were also isolated by ligands. The metal ligand charge transfer usually requires large energy which can be treated as an isolator. Some primary data have demonstrated that MOF as substrate can increase the ACQ limitation up to 80%, when conventional materials can only achieve around 30%. On the other hand, MOF can not only be applied to solve ACQ effects, it can also be used to demonstrate aggregation-induced emission (AIE) affects. By introducing the ligand into MOF backbone, the free rotation will be reduced and the AIE emission can be improved. Compared to pure organic ligand in solid state, MOF can provide porous structure without scarifying fluorescent intensity.

5.3 Ultra-Small Face-Centered-Cubic Ru Nanoparticles Confined Within a Porous Coordination Cage for Dehydrogenation

In chapter IV, a highly negatively charged (30^-) porous coordination cage (PCC-2) was successfully synthesized and utilized to encapsulate Ru NPs to form a Ru NPs@PCC-2 composite, which showed enormously enhanced catalytic activity. PCC-2 can encapsulate Ru precursor and regulate the sizes and structures of the resulting NPs via electrostatic interactions and a cavity confinement effect. The resulting Ru NPs are uniform in size with an unusual fcc crystal structure. The Ru NPs@PCC-2 composite exhibited the highest catalytic activity for methanolysis reactions for AB, which may be ascribed to the highly active fcc structure and the ultra-small diameter of the encapsulated NPs. Chapter IV has demonstrated not only the feasibility of constructing a highly charged PCC but also a promising strategy for encapsulating metal NPs of uniform size and desired structure for highly active catalysis. In the future, DFT calculation could be involved to demonstrate the process of forming of Ru NPs from Ru^{3+} salts and the methanolysis reactions for AB. By studying the simulated data, more solid evidence would be found to support the future application of PCC-2 in NPs synthesis. Meanwhile, the calculation of reaction procedure can help to understand which crystal structure is more favored for the reaction and provide a guide for NPs synthesis.

REFERENCES

1. Deng, H.; Grunder, S.; Cordova, K. E.; Valente, C.; Furukawa, H.; Hmadeh, M.; GÁNdara, F.; Whalley, A. C.; Liu, Z.; Asahina, S., Large-Pore Apertures in A Series of Metal-Organic Frameworks. *Sci.*, **2012**, *336*, 1018-1023.

2. Sato, H.; Kosaka, W.; Matsuda, R.; Hori, A.; Hijikata, Y.; Belosludov, R. V.; Sakaki, S.; Takata, M.; Kitagawa, S., Self-Accelerating CO Sorption in A Soft Nanoporous Crystal. *Sci.*, **2014**, *343*, 167-170.

3. Cui, Y.; Yue, Y.; Qian, G.; Chen, B., Luminescent Functional Metal–Organic Frameworks. *Chem. Rev.*, **2012**, *112*, 1126-1162.

4. Yoon, M.; Srirambalaji, R.; Kim, K., Homochiral Metal–Organic Frameworks for Asymmetric Heterogeneous Catalysis. *Chem. Rev.*, **2012**, *112*, 1196-1231.

5. Kreno, L. E.; Leong, K.; Farha, O. K.; Allendorf, M.; Van Duyne, R. P.; Hupp, J. T., Metal–Organic Framework Materials As Chemical Sensors. *Chem. Rev.*, **2012**, *112*, 1105-1125.

6. Nath, I.; Chakraborty, J.; Verpoort, F., Metal Organic Frameworks Mimicking Natural Enzymes: A Structural and Functional Analogy. *Chem. Soc. Rev.*, **2016**, *45*, 4127-4170.

7. Horcajada, P.; Gref, R.; Baati, T.; Allan, P. K.; Maurin, G.; Couvreur, P.; Ferey, G.; Morris, R. E.; Serre, C., Metal–Organic Frameworks in Biomedicine. *Chem. Rev.*, **2012**, *112*, 1232-1268.

8. Ramaswamy, P.; Wong, N. E.; Shimizu, G. K., Mofs As Proton Conductors–Challenges and Opportunities. *Chem. Soc. Rev.*, **2014**, *43*, 5913-5932.

9. Qin, J.-S.; Yuan, S.; Lollar, C.; Pang, J.; Alsalme, A.; Zhou, H.-C., Stable Metal–Organic Frameworks As A Host Platform for Catalysis and Biomimetics. *Chem. Commun.*, **2018**, *54*, 4231-4249.

10. Deng, H.; Doonan, C. J.; Furukawa, H.; Ferreira, R. B.; Towne, J.; Knobler, C. B.; Wang, B.; Yaghi, O. M., Multiple Functional Groups of Varying Ratios in Metal-Organic Frameworks. *Sci.*, **2010**, *327*, 846-850.

11. Guillerm, V.; Kim, D.; Eubank, J. F.; Luebke, R.; Liu, X.; Adil, K.; Lah, M. S.; Eddaoudi, M., A Supermolecular Building Approach for the Design and Construction of Metal–Organic Frameworks. *Chem. Soc. Rev.*, **2014**, *43*, 6141-6172.

12. Deria, P.; Mondloch, J. E.; Karagiaridi, O.; Bury, W.; Hupp, J. T.; Farha, O. K., Beyond Post-Synthesis Modification: Evolution of Metal–Organic Frameworks Via Building Block Replacement. *Chem. Soc. Rev.*, **2014**, *43*, 5896-5912.

13. Burnett, B. J.; Barron, P. M.; Hu, C.; Choe, W., Stepwise Synthesis of Metal–Organic Frameworks: Replacement of Structural Organic Linkers. *J. Am. Chem. Soc.*, **2011**, *133*, 9984-9987.

14. Kim, M.; Cahill, J. F.; Su, Y.; Prather, K. A.; Cohen, S. M., Postsynthetic Ligand Exchange As A Route to Functionalization of 'Inert'Metal–Organic Frameworks. *Chem. Sci.*, **2012**, *3*, 126-130.

15. Beyzavi, M. H.; Vermeulen, N. A.; Zhang, K.; So, M.; Kung, C. W.; Hupp, J. T.; Farha, O. K., Liquid‐Phase Epitaxially Grown Metal‐Organic Framework Thin Films for Efficient Tandem Catalysis Through Site‐Isolation of Catalytic Centers. *Chempluschem*, **2016**, *81*, 708-713.

16. Xu, Y.; Vermeulen, N. A.; Liu, Y.; Hupp, J. T.; Farha, O. K., SALE‐Ing A MOF‐Based "Ship of Theseus." Sequential Building‐Block Replacement for Complete Reformulation of A Pillared‐Paddlewheel Metal‐Organic Framework. *Eur. J. Inorg. Chem.*, **2016**, *2016*, 4345-4348.

17. Islamoglu, T.; Goswami, S.; Li, Z.; Howarth, A. J.; Farha, O. K.; Hupp, J. T., Postsynthetic Tuning of Metal–Organic Frameworks for Targeted Applications. *Acc. Chem. Res.*, **2017**, *50*, 805-813.

18. Karagiaridi, O.; Bury, W.; Mondloch, J. E.; Hupp, J. T.; Farha, O. K., Solvent‐Assisted Linker Exchange: An Alternative to the De Novo Synthesis of Unattainable Metal‐Organic Frameworks. *Angew. Chem. Int. Ed.*, **2014**, *53*, 4530-4540.

19. González Miera, G.; Bermejo Gómez, A.; Chupas, P. J.; Mart ÍN-Matute, B.; Chapman, K. W.; Platero-Prats, A. E., Topological Transformation of A Metal–Organic Framework Triggered By Ligand Exchange. *Inorg. Chem.*, **2017**, *56*, 4576-4583.

20. Karagiaridi, O.; Bury, W.; Tylianakis, E.; Sarjeant, A. A.; Hupp, J. T.; Farha, O. K., Opening Metal–Organic Frameworks Vol. 2: Inserting Longer Pillars Into Pillared-Paddlewheel Structures Through Solvent-Assisted Linker Exchange. *Chem. Mater.*, **2013**, *25*, 3499-3503.

21. Bureekaew, S.; Amirjalayer, S.; Schmid, R., Orbital Directing Effects in Copper and Zinc Based Paddle-Wheel Metal Organic Frameworks: the Origin of Flexibility. *J. Mater. Chem.*, **2012**, *22*, 10249-10254.

22. Yuan, S.; Chen, Y.-P.; Qin, J.-S.; Lu, W.; Zou, L.; Zhang, Q.; Wang, X.; Sun, X.; Zhou, H.-C., Linker Installation: Engineering Pore Environment With Precisely Placed Functionalities in Zirconium Mofs. *J. Am. Chem. Soc.*, **2016**, *138*, 8912-8919.

23. Li, J.; Yuan, S.; Qin, J.-S.; Pang, J.; Zhang, P.; Zhang, Y.; Huang, Y.; Drake, H. F.; Liu, W. R.; Zhou, H.-C., Stepwise Assembly of Turn-On Fluorescence Sensors in Multicomponent Metal–Organic Frameworks for in Vitro Cyanide Detection. *Angew. Chem. Int. Ed.*, *N/A*.

24. Kirchon, A.; Feng, L.; Drake, H. F.; Joseph, E. A.; Zhou, H.-C., From Fundamentals to Applications: A Toolbox for Robust and Multifunctional MOF Materials. *Chem. Soc. Rev.*, **2018**, *47*, 8611-8638.

25. Yamada, T.; Kitagawa, H., Protection and Deprotection Approach for the Introduction of Functional Groups Into Metal− Organic Frameworks. *J. Am. Chem. Soc.*, **2009**, *131*, 6312-6313.

26. Deshpande, R. K.; Waterhouse, G. I.; Jameson, G. B.; Telfer, S. G., Photolabile Protecting Groups in Metal–Organic Frameworks: Preventing Interpenetration and Masking Functional Groups. *Chem. Commun.*, **2012**, *48*, 1574-1576.

27. Gupta, A. S.; Deshpande, R. K.; Liu, L.; Waterhouse, G. I.; Telfer, S. G., Porosity in Metal–Organic Frameworks Following Thermolytic Postsynthetic Deprotection: Gas Sorption, Dye Uptake and Covalent Derivatisation. *Crystengcomm*, **2012**, *14*, 5701-5704.

28. Yuan, S.; Zou, L.; Qin, J.-S.; Li, J.; Huang, L.; Feng, L.; Wang, X.; Bosch, M.; Alsalme, A.; Cagin, T.; Zhou, H.-C., Construction of Hierarchically Porous Metal–Organic Frameworks Through Linker Labilization. *Nat. Commun.*, **2017**, *8*, 15356.

29. Garibay, S. J.; Wang, Z.; Cohen, S. M., Evaluation of Heterogeneous Metal− Organic Framework Organocatalysts Prepared By Postsynthetic Modification. *Inorg. Chem.*, **2010**, *49*, 8086-8091.

30. Tanabe, K. K.; Cohen, S. M., Postsynthetic Modification of Metal–Organic Frameworks—A Progress Report. *Chem. Soc. Rev.*, **2011**, *40*, 498-519.

31. Cohen, S. M., Postsynthetic Methods for the Functionalization of Metal–Organic Frameworks. *Chem. Rev.*, **2012**, *112*, 970-1000.

32. Cohen, S. M., the Postsynthetic Renaissance in Porous Solids. *J. Am. Chem. Soc.*, **2017**, *139*, 2855-2863.

33. Bunck, D. N.; Dichtel, W. R., Mixed Linker Strategies for Organic Framework Functionalization. *Chemistry–A European Journal*, **2013**, *19*, 818-827.

34. Qin, J.-S.; Yuan, S.; Wang, Q.; Alsalme, A.; Zhou, H.-C., Mixed-Linker Strategy for the Construction of Multifunctional Metal–Organic Frameworks. *J. Mater. Chem. A*, **2017**, *5*, 4280-4291.

35. Wu, C. D.; Zhao, M., Incorporation of Molecular Catalysts in Metal–Organic Frameworks for Highly Efficient Heterogeneous Catalysis. *Adv. Mater.*, **2017**, *29*, 1605446.

36. Rogge, S. M.; Bavykina, A.; Hajek, J.; Garcia, H.; Olivos-Suarez, A. I.; SepÚLveda-Escribano, A.; Vimont, A.; Clet, G.; Bazin, P.; Kapteijn, F., Metal–Organic and Covalent Organic Frameworks As Single-Site Catalysts. *Chem. Soc. Rev.*, **2017**, *46*, 3134-3184.

37. Chui, S. S.-Y.; Lo, S. M.-F.; Charmant, J. P.; Orpen, A. G.; Williams, I. D., A Chemically Functionalizable Nanoporous Material [Cu3 (TMA) 2 (H2O) 3] N. *Sci.*, **1999**, *283*, 1148-1150.

38. Li, H.; Eddaoudi, M.; O'Keeffe, M.; Yaghi, O. M., Design and Synthesis of An Exceptionally Stable and Highly Porous Metal-Organic Framework. *Nature*, **1999**, *402*, 276-279.

39. Wang, C.; Liu, X.; Demir, N. K.; Chen, J. P.; Li, K., Applications of Water Stable Metal–Organic Frameworks. *Chem. Soc. Rev.*, **2016**, *45*, 5107-5134.

40. Devic, T.; Serre, C., High Valence 3p and Transition Metal Based Mofs. *Chem. Soc. Rev.*, **2014**, *43*, 6097-6115.

41. Bai, Y.; Dou, Y.; Xie, L.-H.; Rutledge, W.; Li, J.-R.; Zhou, H.-C., Zr-Based Metal–Organic Frameworks: Design, Synthesis, Structure, and Applications. *Chem. Soc. Rev.*, **2016**, *45*, 2327-2367.

42. Canivet, J.; Fateeva, A.; Guo, Y.; Coasne, B.; Farrusseng, D., Water Adsorption in Mofs: Fundamentals and Applications. *Chem. Soc. Rev.*, **2014**, *43*, 5594-5617.

43. Burtch, N. C.; Jasuja, H.; Walton, K. S., Water Stability and Adsorption in Metal–Organic Frameworks. *Chem. Rev.*, **2014**, *114*, 10575-10612.

44. Howarth, A. J.; Liu, Y.; Li, P.; Li, Z.; Wang, T. C.; Hupp, J. T.; Farha, O. K., Chemical, Thermal and Mechanical Stabilities of Metal–Organic Frameworks. *Nat. Rev. Mater.*, **2016**, *1*, 1-15.

45. Serre, C.; Millange, F.; Thouvenot, C.; NoguÈS, M.; Marsolier, G.; Louër, D.; FÉRey, G., Very Large Breathing Effect in the First Nanoporous Chromium(III)-Based Solids: MIL-53 Or Criii(OH)·{O2C−C6H4−CO2}·{HO2C−C6H4−CO2H}X·H2Oy. *J. Am. Chem. Soc.*, **2002**, *124*, 13519-13526.

46. FÉRey, G.; Serre, C.; Mellot-Draznieks, C.; Millange, F.; SurblÉ, S.; Dutour, J.; Margiolaki, I., A Hybrid Solid With Giant Pores Prepared By A Combination of Targeted Chemistry, Simulation, and Powder Diffraction. *Angew. Chem. Int. Ed.*, **2004**, *43*, 6296-6301.

47. Cavka, J. H.; Jakobsen, S.; Olsbye, U.; Guillou, N.; Lamberti, C.; Bordiga, S.; Lillerud, K. P., A New Zirconium Inorganic Building Brick Forming Metal Organic Frameworks With Exceptional Stability. *J. Am. Chem. Soc.*, **2008**, *130*, 13850-13851.

48. Park, K. S.; Ni, Z.; CôtÉ, A. P.; Choi, J. Y.; Huang, R.; Uribe-Romo, F. J.; Chae, H. K.; O'Keeffe, M.; Yaghi, O. M., Exceptional Chemical and Thermal Stability of Zeolitic Imidazolate Frameworks. *Proc. Natl. Acad. Sci. U.S.A.*, **2006**, *103*, 10186-10191.

49. Demessence, A.; D'Alessandro, D. M.; Foo, M. L.; Long, J. R., Strong CO2 Binding in A Water-Stable, Triazolate-Bridged Metal−Organic Framework Functionalized With Ethylenediamine. *J. Am. Chem. Soc.*, **2009**, *131*, 8784-8786.

50. Choi, H. J.; Dincă, M.; Long, J. R., Broadly Hysteretic H2 Adsorption in the Microporous Metal−Organic Framework Co(1,4-Benzenedipyrazolate). *J. Am. Chem. Soc.*, **2008**, *130*, 7848-7850.

51. Yang, C.; Kaipa, U.; Mather, Q. Z.; Wang, X.; Nesterov, V.; Venero, A. F.; Omary, M. A., Fluorous Metal–Organic Frameworks With Superior Adsorption and Hydrophobic Properties Toward Oil Spill Cleanup and Hydrocarbon Storage. *J. Am. Chem. Soc.*, **2011**, *133*, 18094-18097.

52. Yang, S. J.; Park, C. R., Preparation of Highly Moisture-Resistant Black-Colored Metal Organic Frameworks. *Adv. Mater.*, **2012**, *24*, 4010-4013.

53. Rieter, W. J.; Taylor, K. M. L.; Lin, W., Surface Modification and Functionalization of Nanoscale Metal-Organic Frameworks for Controlled Release and Luminescence Sensing. *J. Am. Chem. Soc.*, **2007**, *129*, 9852-9853.

54. Li, Z.; Zeng, H. C., Armored Mofs: Enforcing Soft Microporous MOF Nanocrystals With Hard Mesoporous Silica. *J. Am. Chem. Soc.*, **2014**, *136*, 5631-5639.

55. Zhang, W.; Hu, Y.; Ge, J.; Jiang, H.-L.; Yu, S.-H., A Facile and General Coating Approach to Moisture/Water-Resistant Metal–Organic Frameworks With Intact Porosity. *J. Am. Chem. Soc.*, **2014**, *136*, 16978-16981.

56. Distefano, G.; Suzuki, H.; Tsujimoto, M.; Isoda, S.; Bracco, S.; Comotti, A.; Sozzani, P.; Uemura, T.; Kitagawa, S., Highly Ordered Alignment of A Vinyl Polymer By Host–Guest Cross-Polymerization. *Nat. Chem.*, **2013**, *5*, 335-341.

57. Mcguire, C. V.; Forgan, R. S., the Surface Chemistry of Metal–Organic Frameworks. *Chem. Commun.*, **2015**, *51*, 5199-5217.

58. Kitao, T.; Zhang, Y.; Kitagawa, S.; Wang, B.; Uemura, T., Hybridization of Mofs and Polymers. *Chem. Soc. Rev.*, **2017**, *46*, 3108-3133.

59. Fu, Y.; Sun, D.; Chen, Y.; Huang, R.; Ding, Z.; Fu, X.; Li, Z., An Amine-Functionalized Titanium Metal–Organic Framework Photocatalyst With Visible-Light-Induced Activity for CO2 Reduction. *Angew. Chem. Int. Ed.*, **2012**, *51*, 3364-3367.

60. Nasalevich, M. A.; Becker, R.; Ramos-Fernandez, E. V.; Castellanos, S.; Veber, S. L.; Fedin, M. V.; Kapteijn, F.; Reek, J. N. H.; Van Der Vlugt, J. I.; Gascon, J., Co@NH2-MIL-125(Ti): Cobaloxime-Derived Metal–Organic Framework-Based Composite for Light-Driven H2 Production. *Energy & Environmental Science*, **2015**, *8*, 364-375.

61. Wang, H.; Lustig, W. P.; Li, J., Sensing and Capture of Toxic and Hazardous Gases and Vapors By Metal–Organic Frameworks. *Chem. Soc. Rev.*, **2018**, *47*, 4729-4756.

62. Li, X.; Wang, X.-W.; Zhang, Y.-H., Blue Photoluminescent 3D Zn(II) Metal-Organic Framework Constructing From Pyridine-2,4,6-Tricarboxylate. *Inorg. Chem. Commun.*, **2008**, *11*, 832-834.

63. Fang, Q.; Zhu, G.; Xue, M.; Sun, J.; Sun, F.; Qiu, S., Structure, Luminescence, and Adsorption Properties of Two Chiral Microporous Metal−Organic Frameworks. *Inorg. Chem.*, **2006**, *45*, 3582-3587.

64. Shustova, N. B.; Mccarthy, B. D.; Dinca, M., Turn-On Fluorescence in Tetraphenylethylene-Based Metal–Organic Frameworks: An Alternative to Aggregation-Induced Emission. *J. Am. Chem. Soc.*, **2011**, *133*, 20126-20129.

65. Shustova, N. B.; Ong, T.-C.; Cozzolino, A. F.; Michaelis, V. K.; Griffin, R. G.; Dincă, M., Phenyl Ring Dynamics in A Tetraphenylethylene-Bridged Metal–Organic Framework: Implications for the Mechanism of Aggregation-Induced Emission. *J. Am. Chem. Soc.*, **2012**, *134*, 15061-15070.

66. Yang, J.; Wang, Z.; Li, Y.; Zhuang, Q.; Gu, J., Real-Time Monitoring of Dissolved Oxygen With Inherent Oxygen-Sensitive Centers in Metal–Organic Frameworks. *Chem. Mater.*, **2016**, *28*, 2652-2658.

67. Sikdar, N.; Dutta, D.; Haldar, R.; Ray, T.; Hazra, A.; Bhattacharyya, A. J.; Maji, T. K., Coordination-Driven Fluorescent J-Aggregates in A Perylenetetracarboxylate-Based MOF: Permanent Porosity and Proton Conductivity. *J. Phys. Chem. C*, **2016**, *120*, 13622-13629.

68. Nickerl, G.; Senkovska, I.; Kaskel, S., Tetrazine Functionalized Zirconium MOF As An Optical Sensor for Oxidizing Gases. *Chem. Commun.*, **2015**, *51*, 2280-2282.

69. Zhou, H.-C.; Long, J. R.; Yaghi, O. M., Introduction to Metal–Organic Frameworks. *Chemical Reviews*, **2012**, *112*, 673-674.

70. Li, B.; Wen, H.-M.; Zhou, W.; Chen, B., Porous Metal–Organic Frameworks for Gas Storage and Separation: What, How, and Why? the *Journal of Physical Chemistry Letters*, **2014**, *5*, 3468-3479.

71. Lian, X.; Fang, Y.; Joseph, E.; Wang, Q.; Li, J.; Banerjee, S.; Lollar, C.; Wang, X.; Zhou, H.-C., Enzyme–MOF (Metal–Organic Framework) Composites. *Chem. Soc. Rev.*, **2017**, *46*, 3386-3401.

72. Pisklak, T. J.; Mac ÍAs, M.; Coutinho, D. H.; Huang, R. S.; Balkus, K. J., Hybrid Materials for Immobilization of MP-11 Catalyst. *Topics in Catalysis*, **2006**, *38*, 269-278.

73. Patra, S.; Hidalgo Crespo, T.; Permyakova, A.; Sicard, C.; Serre, C.; ChaussÉ, A.; Steunou, N.; Legrand, L., Design of Metal Organic Framework–Enzyme Based Bioelectrodes As A Novel and Highly Sensitive Biosensing Platform. *J. Mater. Chem. B*, **2015**, *3*, 8983-8992.

74. Cao, Y.; Wu, Z.; Wang, T.; Xiao, Y.; Huo, Q.; Liu, Y., Immobilization of Bacillus Subtilis Lipase on A Cu-BTC Based Hierarchically Porous Metal–Organic Framework Material: A Biocatalyst for Esterification. *Dalton Transactions*, **2016**, *45*, 6998-7003.

75. Liu, W.-L.; Yang, N.-S.; Chen, Y.-T.; Lirio, S.; Wu, C.-Y.; Lin, C.-H.; Huang, H.-Y., Lipase-Supported Metal–Organic Framework Bioreactor Catalyzes Warfarin Synthesis. *Chemistry – A European Journal*, **2015**, *21*, 115-119.

76. Liu, W.-L.; Lo, S.-H.; Singco, B.; Yang, C.-C.; Huang, H.-Y.; Lin, C.-H., Novel Trypsin–FITC@MOF Bioreactor Efficiently Catalyzes Protein Digestion. *Journal of Materials Chemistry B*, **2013**, *1*, 928-932.

77. Liu, W.-L.; Wu, C.-Y.; Chen, C.-Y.; Singco, B.; Lin, C.-H.; Huang, H.-Y., Fast Multipoint Immobilized MOF Bioreactor. *Chemistry – A European Journal*, **2014**, *20*, 8923-8928.

78. Ma, W.; Jiang, Q.; Yu, P.; Yang, L.; Mao, L., Zeolitic Imidazolate Framework-Based Electrochemical Biosensor for in Vivo Electrochemical Measurements. *Analytical Chemistry*, **2013**, *85*, 7550-7557.

79. Lian, X.; Erazo-Oliveras, A.; Pellois, J.-P.; Zhou, H.-C., High Efficiency and Long-Term Intracellular Activity of An Enzymatic Nanofactory Based on Metal-Organic Frameworks. *Nature Communications*, **2017**, *8*, 2075.

80. Wang, W.; Wang, L.; Huang, Y.; Xie, Z.; Jing, X., Nanoscale Metal–Organic Framework–Hemoglobin Conjugates. *Chemistry – An Asian Journal*, **2016**, *11*, 750-756.

81. Jung, S.; Kim, Y.; Kim, S.-J.; Kwon, T.-H.; Huh, S.; Park, S., Bio-Functionalization of Metal–Organic Frameworks By Covalent Protein Conjugation. *Chemical Communications*, **2011**, *47*, 2904-2906.

82. Shih, Y.-H.; Lo, S.-H.; Yang, N.-S.; Singco, B.; Cheng, Y.-J.; Wu, C.-Y.; Chang, I.-H.; Huang, H.-Y.; Lin, C.-H., Trypsin-Immobilized Metal–Organic Framework As A Biocatalyst in Proteomics Analysis. *Chempluschem*, **2012**, *77*, 982-986.

83. Cao, S.-L.; Yue, D.-M.; Li, X.-H.; Smith, T. J.; Li, N.; Zong, M.-H.; Wu, H.; Ma, Y.-Z.; Lou, W.-Y., Novel Nano-/Micro-Biocatalyst: Soybean Epoxide Hydrolase Immobilized on Uio-66-NH2 MOF for Efficient Biosynthesis of Enantiopure (R)-1, 2-Octanediol in Deep Eutectic Solvents. *ACS Sustainable Chemistry & Engineering*, **2016**, *4*, 3586-3595.

84. Qin, F.-X.; Jia, S.-Y.; Wang, F.-F.; Wu, S.-H.; Song, J.; Liu, Y., Hemin@Metal–Organic Framework With Peroxidase-Like Activity and Its Application to Glucose Detection. *Catalysis Science & Technology*, **2013**, *3*, 2761-2768.

85. Maksimchuk, N. V.; Zalomaeva, O. V.; Skobelev, I. Y.; Kovalenko, K. A.; Fedin, V. P.; Kholdeeva, O. A., Metal–Organic Frameworks of the MIL-101 Family As Heterogeneous Single-Site Catalysts. *Proceedings of the Royal Society A: Mathematical, Physical and Engineering Sciences*, **2012**, *468*, 2017-2034.

86. Horike, S.; Dinca, M.; Tamaki, K.; Long, J. R., Size-Selective Lewis Acid Catalysis in A Microporous Metal-Organic Framework With Exposed Mn2+ Coordination Sites. *J. Am. Chem. Soc.*, **2008**, *130*, 5854-5855.

87. Yuan, S.; Qin, J.-S.; Su, J.; Li, B.; Li, J.; Chen, W.; Drake, H. F.; Zhang, P.; Yuan, D.; Zuo, J.; Zhou, H.-C., Sequential Transformation of Zirconium(IV)-Mofs Into Heterobimetallic Mofs Bearing Magnetic Anisotropic Cobalt(II) Centers. *Angew. Chem. Int. Ed.*, **2018**, *57*, 12578-12583.

88. Schlichte, K.; Kratzke, T.; Kaskel, S., Improved Synthesis, Thermal Stability and Catalytic Properties of the Metal-Organic Framework Compound Cu3 (BTC) 2. *Microporous Mesoporous Mater.*, **2004**, *73*, 81-88.

89. Alaerts, L.; SÉGuin, E.; Poelman, H.; Thibault ‐ Starzyk, F.; Jacobs, P. A.; De Vos, D. E., Probing the Lewis Acidity and Catalytic Activity of the Metal ‐ Organic Framework [Cu3 (Btc) 2](BTC= Benzene ‐ 1, 3, 5 ‐ Tricarboxylate). *Chemistry ‐ A European Journal*, **2006**, *12*, 7353-7363.

90. Li, G.; Zhao, S.; Zhang, Y.; Tang, Z., Metal–Organic Frameworks Encapsulating Active Nanoparticles As Emerging Composites for Catalysis: Recent Progress and Perspectives. *Adv. Mater.*, **2018**, *30*, 1800702.

91. Pang, J.; Yuan, S.; Qin, J.-S.; Lollar, C. T.; Huang, N.; Li, J.; Wang, Q.; Wu, M.; Yuan, D.; Hong, M.; Zhou, H.-C., Tuning the Ionicity of Stable Metal–Organic Frameworks Through Ionic Linker Installation. *J. Am. Chem. Soc.*, **2019**, *141*, 3129-3136.

92. Elumalai, P.; Mamlouk, H.; Yiming, W.; Feng, L.; Yuan, S.; Zhou, H.-C.; Madrahimov, S. T., Recyclable and Reusable Heteroleptic Nickel Catalyst Immobilized on Metal–Organic Framework for Suzuki–Miyaura Coupling. *ACS Appl. Mater. Interfaces*, **2018**, *10*, 41431-41438.

93. Lu, G.; Li, S.; Guo, Z.; Farha, O. K.; Hauser, B. G.; Qi, X.; Wang, Y.; Wang, X.; Han, S.; Liu, X.; Duchene, J. S.; Zhang, H.; Zhang, Q.; Chen, X.; Ma, J.; Loo, S. C. J.; Wei, W. D.; Yang, Y.; Hupp, J. T.; Huo, F., Imparting Functionality to A Metal–Organic Framework Material By Controlled Nanoparticle Encapsulation. *Nat. Chem.*, **2012**, *4*, 310-316.

94. Wang, Q.; Astruc, D., State of the Art and Prospects in Metal–Organic Framework (MOF)-Based and MOF-Derived Nanocatalysis. *Chem. Rev.*, **2020**, *120*, 1438-1511.

95. Huang, Y.; Zhang, Y.; Chen, X.; Wu, D.; Yi, Z.; Cao, R., Bimetallic Alloy Nanocrystals Encapsulated in ZIF-8 for Synergistic Catalysis of Ethylene Oxidative Degradation. *Chem. Commun.*, **2014**, *50*, 10115-10117.

96. Rösler, C.; Esken, D.; Wiktor, C.; Kobayashi, H.; Yamamoto, T.; Matsumura, S.; Kitagawa, H.; Fischer, R. A., Encapsulation of Bimetallic Nanoparticles Into A Metal–Organic Framework: Preparation and Microstructure Characterization of Pd/Au@ZIF-8. *Eur. J. Inorg. Chem.*, **2014**, *2014*, 5514-5521.

97. Chen, L.; Chen, X.; Liu, H.; Li, Y., Encapsulation of Mono- Or Bimetal Nanoparticles Inside Metal–Organic Frameworks Via in Situ Incorporation of Metal Precursors. *Small*, **2015**, *11*, 2642-2648.

98. Zhu, Q.-L.; Li, J.; Xu, Q., Immobilizing Metal Nanoparticles to Metal–Organic Frameworks With Size and Location Control for Optimizing Catalytic Performance. *J. Am. Chem. Soc.*, **2013**, *135*, 10210-10213.

99. Li, J.; Zhu, Q.-L.; Xu, Q., Highly Active Auco Alloy Nanoparticles Encapsulated in the Pores of Metal–Organic Frameworks for Hydrolytic Dehydrogenation of Ammonia Borane. *Chem. Commun.*, **2014**, *50*, 5899-5901.

100. Li, J.; Zhu, Q.-L.; Xu, Q., Non-Noble Bimetallic Cuco Nanoparticles Encapsulated in the Pores of Metal–Organic Frameworks: Synergetic Catalysis in the Hydrolysis of

Ammonia Borane for Hydrogen Generation. *Catalysis Science & Technology*, **2015**, *5*, 525-530.

101. Singh, A. K.; Xu, Q., Metal–Organic Framework Supported Bimetallic Ni Pt Nanoparticles As High‐Performance Catalysts for Hydrogen Generation From Hydrazine in Aqueous Solution. *Chemcatchem*, **2013**, *5*, 3000-3004.

102. Cao, N.; Yang, L.; Dai, H.; Liu, T.; Su, J.; Wu, X.; Luo, W.; Cheng, G., Immobilization of Ultrafine Bimetallic Ni–Pt Nanoparticles Inside the Pores of Metal–Organic Frameworks As Efficient Catalysts for Dehydrogenation of Alkaline Solution of Hydrazine. *Inorg. Chem.*, **2014**, *53*, 10122-10128.

103. Wen, L.; Du, X.; Su, J.; Luo, W.; Cai, P.; Cheng, G., Ni–Pt Nanoparticles Growing on Metal Organic Frameworks (MIL-96) With Enhanced Catalytic Activity for Hydrogen Generation From Hydrazine At Room Temperature. *Dalton Trans.*, **2015**, *44*, 6212-6218.

104. Xia, B.; Cao, N.; Dai, H.; Su, J.; Wu, X.; Luo, W.; Cheng, G., Bimetallic Nickel‐Rhodium Nanoparticles Supported on ZIF‐8 As Highly Efficient Catalysts for Hydrogen Generation From Hydrazine in Alkaline Solution. *Chemcatchem*, **2014**, *6*, 2549-2552.

105. Gu, X.; Lu, Z.-H.; Jiang, H.-L.; Akita, T.; Xu, Q., Synergistic Catalysis of Metal–Organic Framework-Immobilized Au–Pd Nanoparticles in Dehydrogenation of Formic Acid for Chemical Hydrogen Storage. *J. Am. Chem. Soc.*, **2011**, *133*, 11822-11825.

106. Yan, J. M.; Wang, Z. L.; Gu, L.; Li, S. J.; Wang, H. L.; Zheng, W. T.; Jiang, Q., Aupd–Mnox/MOF–Graphene: An Efficient Catalyst for Hydrogen Production From Formic Acid At Room Temperature. *Advanced Energy Materials*, **2015**, *5*, 1500107.

107. Dai, H.; Xia, B.; Wen, L.; Du, C.; Su, J.; Luo, W.; Cheng, G., Synergistic Catalysis of Agpd@ ZIF-8 on Dehydrogenation of Formic Acid. *APPL CATAL B-ENVIRON*, **2015**, *165*, 57-62.

108. Tedsree, K.; Chan, C. W. A.; Jones, S.; Cuan, Q.; Li, W.-K.; Gong, X.-Q.; Tsang, S. C. E., 13C NMR Guides Rational Design of Nanocatalysts Via Chemisorption Evaluation in Liquid Phase. *Sci.*, **2011**, *332*, 224-228.

109. Lim, D. W.; Yoon, J. W.; Ryu, K. Y.; Suh, M. P., Magnesium Nanocrystals Embedded in A Metal‐Organic Framework: Hybrid Hydrogen Storage With Synergistic Effect on Physi‐ And Chemisorption. *Angew. Chem. Int. Ed.*, **2012**, *51*, 9814-9817.

110. Li, Z.; Yu, R.; Huang, J.; Shi, Y.; Zhang, D.; Zhong, X.; Wang, D.; Wu, Y.; Li, Y., Platinum–Nickel Frame Within Metal-Organic Framework Fabricated in Situ for Hydrogen Enrichment and Molecular Sieving. *Nat. Commun.*, **2015**, *6*, 1-8.

111. Liu, Y.; Liu, Z.; Huang, D.; Cheng, M.; Zeng, G.; Lai, C.; Zhang, C.; Zhou, C.; Wang, W.; Jiang, D.; Wang, H.; Shao, B., Metal Or Metal-Containing Nanoparticle@MOF Nanocomposites As A Promising Type of Photocatalyst. *Coord. Chem. Rev.*, **2019**, *388*, 63-78.

112. Jiang, H.-L.; Akita, T.; Ishida, T.; Haruta, M.; Xu, Q., Synergistic Catalysis of Au@Ag Core−Shell Nanoparticles Stabilized on Metal−Organic Framework. *J. Am. Chem. Soc.*, **2011**, *133*, 1304-1306.

113. Luo, C.; Fu, F.; Yang, X.; Wei, J.; Wang, C.; Zhu, J.; Huang, D.; Astruc, D.; Zhao, P., Highly Efficient and Selective Co@ZIF-8 Nanocatalyst for Hydrogen Release From Sodium Borohydride Hydrolysis. *Chemcatchem*, **2019**, *11*, 1643-1649.

114. Fu, F.; Wang, C.; Wang, Q.; Martinez-Villacorta, A. M.; Escobar, A.; Chong, H.; Wang, X.; Moya, S.; Salmon, L.; Fouquet, E.; Ruiz, J.; Astruc, D., Highly Selective and Sharp Volcano-Type Synergistic Ni2Pt@ZIF-8-Catalyzed Hydrogen Evolution From Ammonia Borane Hydrolysis. *J. Am. Chem. Soc.*, **2018**, *140*, 10034-10042.

115. Chen, M.; Xiong, R.; Cui, X.; Wang, Q.; Liu, X., Sio2-Encompassed Co@N-Doped Porous Carbon Assemblies As Recyclable Catalysts for Efficient Hydrolysis of Ammonia Borane. *Langmuir*, **2019**, *35*, 671-677.

116. Zacho, S. L.; Mielby, J.; Kegnæs, S., Hydrolytic Dehydrogenation of Ammonia Borane Over ZIF-67 Derived Co Nanoparticle Catalysts. *Catalysis Science & Technology*, **2018**, *8*, 4741-4746.

117. Fang, Y.; Xiao, Z.; Li, J.; Lollar, C.; Liu, L.; Lian, X.; Yuan, S.; Banerjee, S.; Zhang, P.; Zhou, H.-C., Formation of A Highly Reactive Cobalt Nanocluster Crystal Within A Highly Negatively Charged Porous Coordination Cage. *Angew. Chem. Int. Ed.*, **2018**, *57*, 5283-5287.

118. Aijaz, A.; Karkamkar, A.; Choi, Y. J.; Tsumori, N.; Rönnebro, E.; Autrey, T.; Shioyama, H.; Xu, Q., Immobilizing Highly Catalytically Active Pt Nanoparticles Inside the Pores of Metal–Organic Framework: A Double Solvents Approach. *J. Am. Chem. Soc.*, **2012**, *134*, 13926-13929.

119. Lee, J.; Farha, O. K.; Roberts, J.; Scheidt, K. A.; Nguyen, S. T.; Hupp, J. T., Metal–Organic Framework Materials As Catalysts. *Chem. Soc. Rev.*, **2009**, *38*, 1450-1459.

120. Sumida, K.; Rogow, D. L.; Mason, J. A.; Mcdonald, T. M.; Bloch, E. D.; Herm, Z. R.; Bae, T.-H.; Long, J. R., Carbon Dioxide Capture in Metal–Organic Frameworks. *Chem. Rev.*, **2012**, *112*, 724-781.

121. Trickett, C. A.; Helal, A.; Al-Maythalony, B. A.; Yamani, Z. H.; Cordova, K. E.; Yaghi, O. M., the Chemistry of Metal–Organic Frameworks for CO2 Capture, Regeneration and Conversion. *Nat. Rev. Mater.*, **2017**, *2*, 17045.

122. So, M. C.; Wiederrecht, G. P.; Mondloch, J. E.; Hupp, J. T.; Farha, O. K., Metal–Organic Framework Materials for Light-Harvesting and Energy Transfer. *Chem. Commun.*, **2015**, *51*, 3501-3510.

123. Horcajada, P.; Gref, R.; Baati, T.; Allan, P. K.; Maurin, G.; Couvreur, P.; FÉRey, G.; Morris, R. E.; Serre, C., Metal–Organic Frameworks in Biomedicine. *Chem. Rev.*, **2012**, *112*, 1232-1268.

124. Karmakar, A.; Kumar, N.; Samanta, P.; Desai, A. V.; Ghosh, S. K., A Post-Synthetically Modified MOF for Selective and Sensitive Aqueous-Phase Detection of Highly Toxic Cyanide Ions. *Chem. Eur. J.*, **2016**, *22*, 864-868.

125. Michel, B. W.; Lippert, A. R.; Chang, C. J., A Reaction-Based Fluorescent Probe for Selective Imaging of Carbon Monoxide in Living Cells Using A Palladium-Mediated Carbonylation. *J. Am. Chem. Soc.*, **2012**, *134*, 15668-15671.

126. Cotruvo, J. J. A.; Aron, A. T.; Ramos-Torres, K. M.; Chang, C. J., Synthetic Fluorescent Probes for Studying Copper in Biological Systems. *Chem. Soc. Rev.*, **2015**, *44*, 4400-4414.

127. Moriya, F.; Hashimoto, Y., Potential for Error When Assessing Blood Cyanide Concentrations in Fire Victims. *J. Forensic Sci.*, **2001**, *46*, 1421-1425.

128. Lee, K.-S.; Kim, H.-J.; Kim, G.-H.; Shin, I.; Hong, J.-I., Fluorescent Chemodosimeter for Selective Detection of Cyanide in Water. *Org. Lett.*, **2008**, *10*, 49-51.

129. Badugu, R.; Lakowicz, J. R.; Geddes, C. D., Enhanced Fluorescence Cyanide Detection At Physiologically Lethal Levels: Reduced ICT-Based Signal Transduction. *J. Am. Chem. Soc.*, **2005**, *127*, 3635-3641.

130. Jamkratoke, M.; Ruangpornvisuti, V.; Tumcharern, G.; Tuntulani, T.; Tomapatanaget, B., A-D-A Sensors Based on Naphthoimidazoledione and Boronic Acid As Turn-On Cyanide Probes in Water. *J. Org. Chem.*, **2009**, *74*, 3919-3922.

131. Cho, D.-G.; Kim, J. H.; Sessler, J. L., the Benzil−Cyanide Reaction and Its Application to the Development of A Selective Cyanide Anion Indicator. *J. Am. Chem. Soc.*, **2008**, *130*, 12163-12167.

132. Jung, H. S.; Han, J. H.; Kim, Z. H.; Kang, C.; Kim, J. S., Coumarin-Cu(II) Ensemble-Based Cyanide Sensing Chemodosimeter. *Org. Lett.*, **2011**, *13*, 5056-5059.

133. Wang, F.; Wang, L.; Chen, X.; Yoon, J., Recent Progress in the Development of Fluorometric and Colorimetric Chemosensors for Detection of Cyanide Ions. *Chem. Soc. Rev.*, **2014**, *43*, 4312-4324.

134. Liu, L.; Konstas, K.; Hill, M. R.; Telfer, S. G., Programmed Pore Architectures in Modular Quaternary Metal–Organic Frameworks. *J. Am. Chem. Soc.*, **2013**, *135*, 17731-17734.

135. Tu, B.; Pang, Q.; Xu, H.; Li, X.; Wang, Y.; Ma, Z.; Weng, L.; Li, Q., Reversible Redox Activity in Multicomponent Metal–Organic Frameworks Constructed From Trinuclear Copper Pyrazolate Building Blocks. *J. Am. Chem. Soc.*, **2017**, *139*, 7998-8007.

136. Yuan, S.; Qin, J.-S.; Li, J.; Huang, L.; Feng, L.; Fang, Y.; Lollar, C.; Pang, J.; Zhang, L.; Sun, D.; Alsalme, A.; Cagin, T.; Zhou, H.-C., Retrosynthesis of Multi-Component Metal−Organic Frameworks. *Nat. Commun.*, **2018**, *9*, 808.

137. Burrows, A. D., Mixed-Component Metal–Organic Frameworks (MC-Mofs): Enhancing Functionality Through Solid Solution Formation and Surface Modifications. *Crystengcomm*, **2011**, *13*, 3623-3642.

138. Chen, C.-X.; Wei, Z.; Jiang, J.-J.; Fan, Y.-Z.; Zheng, S.-P.; Cao, C.-C.; Li, Y.-H.; Fenske, D.; Su, C.-Y., Precise Modulation of the Breathing Behavior and Pore Surface in Zr-Mofs By Reversible Post-Synthetic Variable-Spacer Installation to Fine-Tune the Expansion Magnitude and Sorption Properties. *Angew. Chem. Int. Ed.*, **2016**, *55*, 9932-9936.

139. Chen, C.-X.; Wei, Z.-W.; Jiang, J.-J.; Zheng, S.-P.; Wang, H.-P.; Qiu, Q.-F.; Cao, C.-C.; Fenske, D.; Su, C.-Y., Dynamic Spacer Installation for Multirole Metal–Organic Frameworks: A New Direction Toward Multifunctional Mofs Achieving Ultrahigh Methane Storage Working Capacity. *J. Am. Chem. Soc.*, **2017**, *139*, 6034-6037.

140. Zhang, X.; Frey, B. L.; Chen, Y.-S.; Zhang, J., Topology-Guided Stepwise Insertion of Three Secondary Linkers in Zirconium Metal–Organic Frameworks. *J. Am. Chem. Soc.*, **2018**, *140*, 7710-7715.

141. Dolgopolova, E. A.; Ejegbavwo, O. A.; Martin, C. R.; Smith, M. D.; Setyawan, W.; Karakalos, S. G.; Henager, C. H.; Zur Loye, H.-C.; Shustova, N. B., Multifaceted Modularity: A Key for Stepwise Building of Hierarchical Complexity in Actinide Metal–Organic Frameworks. *J. Am. Chem. Soc.*, **2017**, *139*, 16852-16861.

142. Lee, C. Y.; Farha, O. K.; Hong, B. J.; Sarjeant, A. A.; Nguyen, S. T.; Hupp, J. T., Light-Harvesting Metal–Organic Frameworks (Mofs): Efficient Strut-To-Strut Energy Transfer in Bodipy and Porphyrin-Based Mofs. *J. Am. Chem. Soc.*, **2011**, *133*, 15858-15861.

143. Zhang, Q.; Zhang, C.; Cao, L.; Wang, Z.; An, B.; Lin, Z.; Huang, R.; Zhang, Z.; Wang, C.; Lin, W., Förster Energy Transport in Metal–Organic Frameworks Is Beyond Step-By-Step Hopping. *J. Am. Chem. Soc.*, **2016**, *138*, 5308-5315.

144. Wang, Z.; Liu, Y.; Wang, Z.; Cao, L.; Zhao, Y.; Wang, C.; Lin, W., Through-Space Förster-Type Energy Transfer in Isostructural Zirconium and Hafnium-Based Metal–Organic Layers. *Chem. Commun.*, **2017**, *53*, 9356-9359.

145. Xu, M.; Feng, L.; Yan, L.-N.; Meng, S.-S.; Yuan, S.; He, M.-J.; Liang, H.; Chen, X.-Y.; Wei, H.-Y.; Gu, Z.-Y.; Zhou, H.-C., Discovery of Precise Ph-Controlled Biomimetic Catalysts: Defective Zirconium Metal–Organic Frameworks As Alkaline Phosphatase Mimics. *Nanoscale*, **2019**, *11*, 11270-11278.

146. Sun, M.; Wang, S.; Yang, Q.; Fei, X.; Li, Y.; Li, Y., A New Colorimetric Fluorescent Sensor for Ratiometric Detection of Cyanide in Solution, Test Strips, and in Cells. *RSC Adv.*, **2014**, *4*, 8295-8299.

147. Peng, M.-J.; Guo, Y.; Yang, X.-F.; Suzenet, F.; Li, J.; Li, C.-W.; Duan, Y.-W., Coumarin–Hemicyanine Conjugates As Novel Reaction-Based Sensors for Cyanide Detection: Convenient Synthesis and ICT Mechanism. *RSC Adv.*, **2014**, *4*, 19077-19085.

148. Goswami, S.; Paul, S.; Manna, A., Carbazole Based Hemicyanine Dye for Both "Naked Eye" and 'NIR' Fluorescence Detection of CN− in Aqueous Solution: From Molecules to Low Cost Devices (TLC Plate Sticks). *Dalton Trans.*, **2013**, *42*, 10682-10686.

149. Xiong, K.; Huo, F.; Yin, C.; Yang, Y.; Chao, J.; Zhang, Y.; Xu, M., A Off–On Green Fluorescent Chemosensor for Cyanide Based on A Hybrid Coumarin–Hemicyanine Dye and Its Bioimaging. *Sensor Actuat B-Chem*, **2015**, *220*, 822-828.

150. Yuan, S.; Lu, W.; Chen, Y.-P.; Zhang, Q.; Liu, T.-F.; Feng, D.; Wang, X.; Qin, J.; Zhou, H.-C., Sequential Linker Installation: Precise Placement of Functional Groups in Multivariate Metal–Organic Frameworks. *J. Am. Chem. Soc.*, **2015**, *137*, 3177-3180.

151. Edelhoch, H.; Brand, L.; Wilchek, M., Fluorescence Studies With Tryptophyl Peptides*. *Biochemistry*, **1967**, *6*, 547-559.

152. Karmakar, A.; Joarder, B.; Mallick, A.; Samanta, P.; Desai, A. V.; Basu, S.; Ghosh, S. K., Aqueous Phase Sensing of Cyanide Ions Using A Hydrolytically Stable Metal–Organic Framework. *Chem. Commun.*, **2017**, *53*, 1253-1256.

153. Xu, W.; Liang, W.; Wu, W.; Fan, C.; Rao, M.; Su, D.; Zhong, Z.; Yang, C., Supramolecular Assembly-Improved Triplet–Triplet Annihilation Upconversion in Aqueous Solution. *Chem. Eur. J.*, **2018**, *24*, 16677-16685.

154. Burrows, A. D.; Frost, C. G.; Mahon, M. F.; Richardson, C., Post-Synthetic Modification of Tagged Metal–Organic Frameworks. *Angew. Chem. Int. Ed.*, **2008**, *47*, 8482-8486.

155. Sheldrick, G., A Short History of SHELX. *Acta Crystallographica Section A*, **2008**, *64*, 112-122.

156. Spek, A., Single-Crystal Structure Validation With the Program PLATON. *J. Appl. Crystallogr.*, **2003**, *36*, 7-13.

157. Wuttke, S.; Dietl, C.; Hinterholzinger, F. M.; Hintz, H.; Langhals, H.; Bein, T., Turn-On Fluorescence Triggered By Selective Internal Dye Replacement in Mofs. *Chem. Commun.*, **2014**, *50*, 3599-3601.

158. Dietl, C.; Hintz, H.; RÜHle, B.; Schmedt Auf Der GÜNne, J.; Langhals, H.; Wuttke, S., Switch-On Fluorescence of A Perylene-Dye-Functionalized Metal–Organic Framework Through Postsynthetic Modification. *Chem. Eur. J.*, **2015**, *21*, 10714-10720.

159. Kaiser, T. E.; Wang, H.; Stepanenko, V.; WÜRthner, F., Supramolecular Construction of Fluorescent J-Aggregates Based on Hydrogen-Bonded Perylene Dyes. *Angew. Chem. Int. Ed.*, **2007**, *46*, 5541-5544.

160. Markiewicz, J. T.; Wudl, F., Perylene, Oligorylenes, and Aza-Analogs. *ACS Appl. Mater. Interfaces*, **2015**, *7*, 28063-28085.

161. Son, M.; Park, K. H.; Shao, C.; WÜRthner, F.; Kim, D., Spectroscopic Demonstration of Exciton Dynamics and Excimer Formation in A Sterically Controlled Perylene Bisimide Dimer Aggregate. *J. Phys. Chem. Lett.*, **2014**, *5*, 3601-3607.

162. Furube, A.; Murai, M.; Tamaki, Y.; Watanabe, S.; Katoh, R., Effect of Aggregation on the Excited-State Electronic Structure of Perylene Studied By Transient Absorption Spectroscopy. *J. Phys. Chem. A*, **2006**, *110*, 6465-6471.

163. WÜRthner, F.; Stolte, M., Naphthalene and Perylene Diimides for Organic Transistors. *Chem. Commun.*, **2011**, *47*, 5109-5115.

164. Zhang, Q.; Cirpan, A.; Russell, T. P.; Emrick, T., Donor−Acceptor Poly(Thiophene-Block-Perylene Diimide) Copolymers: Synthesis and Solar Cell Fabrication. *Macromolecules*, **2009**, *42*, 1079-1082.

165. Niko, Y.; Kawauchi, S.; Otsu, S.; Tokumaru, K.; Konishi, G.-I., Fluorescence Enhancement of Pyrene Chromophores Induced By Alkyl Groups Through Σ–Π Conjugation: Systematic Synthesis of Primary, Secondary, and Tertiary Alkylated Pyrenes At the 1, 3, 6, and 8 Positions and Their Photophysical Properties. *J. Org. Chem.*, **2013**, *78*, 3196-3207.

166. Liu, Y.; Wang, K.-R.; Guo, D.-S.; Jiang, B.-P., Supramolecular Assembly of Perylene Bisimide With Β-Cyclodextrin Grafts As A Solid-State Fluorescence Sensor for Vapor Detection. *Adv. Funct. Mater.*, **2009**, *19*, 2230-2235.

167. Chang, X.; Zhou, Z.; Shang, C.; Wang, G.; Wang, Z.; Qi, Y.; Li, Z.-Y.; Wang, H.; Cao, L.; Li, X.; Fang, Y.; Stang, P. J., Coordination-Driven Self-Assembled Metallacycles Incorporating Pyrene: Fluorescence Mutability, Tunability, and Aromatic Amine Sensing. *J. Am. Chem. Soc.*, **2019**, *141*, 1757-1765.

168. Trickett, C. A.; Helal, A.; Al-Maythalony, B. A.; Yamani, Z. H.; Cordova, K. E.; Yaghi, O. M., the Chemistry of Metal–Organic Frameworks for CO2 Capture, Regeneration and Conversion. *Nat. Rev. Mater.*, **2017**, *2*, 17045.

169. Gonzalez, M. I.; Bloch, E. D.; Mason, J. A.; Teat, S. J.; Long, J. R., Single-Crystal-To-Single-Crystal Metalation of A Metal–Organic Framework: A Route Toward Structurally Well-Defined Catalysts. *Inorg. Chem.*, **2015**, *54*, 2995-3005.

170. Yu, J.; Park, J.; Van Wyk, A.; Rumbles, G.; Deria, P., Excited-State Electronic Properties in Zr-Based Metal–Organic Frameworks As A Function of A Topological Network. *J. Am. Chem. Soc.*, **2018**, *140*, 10488-10496.

171. Sue, A. C.-H.; Mannige, R. V.; Deng, H.; Cao, D.; Wang, C.; GÁNdara, F.; Stoddart, J. F.; Whitelam, S.; Yaghi, O. M., Heterogeneity of Functional Groups in A Metal–Organic Framework Displays Magic Number Ratios. *Proc. Natl. Acad. Sci. U.S.A.*, **2015**, *112*, 5591-5596.

172. Geng, Z.; Liu, Y.; Kong, X.; Li, P.; Li, K.; Liu, Z.; Du, J.; Shu, M.; Si, R.; Zeng, J., Achieving A Record‐High Yield Rate of 120.9 for N2 Electrochemical Reduction Over Ru Single‐Atom Catalysts. *Adv. Mater.*, **2018**, *30*, 1803498.

173. Shold, D. M., Formation of Singlet Oxygen From Aromatic Excimers and Monomers. *Journal of Photochemistry*, **1978**, *8*, 39-48.

174. Sharma, A.; Wolfbeis, O. S., Unusually Efficient Quenching of the Fluoroscence of An Energy Transfer-Based Optical Sensor for Oxygen. *Anal. Chim. Acta*, **1988**, *212*, 261-265.

175. Stoeck, U.; Senkovska, I.; Bon, V.; Krause, S.; Kaskel, S., Assembly of Metal–Organic Polyhedra Into Highly Porous Frameworks for Ethene Delivery. *Chem. Commun.*, **2015**, *51*, 1046-1049.

176. Goesmann, H.; Feldmann, C., Nanoparticulate Functional Materials. *Angew. Chem. Int. Ed.*, **2010**, *49*, 1362-1395.

177. Sun, Y.; Xia, Y., Shape-Controlled Synthesis of Gold and Silver Nanoparticles. *Sci.*, **2002**, *298*, 2176-2179.

178. Sau, T. K.; Rogach, A. L.; Jäckel, F.; Klar, T. A.; Feldmann, J., Properties and Applications of Colloidal Nonspherical Noble Metal Nanoparticles. *Adv. Mater.*, **2010**, *22*, 1805-1825.

179. Burda, C.; Chen, X.; Narayanan, R.; El-Sayed, M. A., Chemistry and Properties of Nanocrystals of Different Shapes. *Chem. Rev.*, **2005**, *105*, 1025-1102.

180. Zhu, Q.-L.; Xu, Q., Immobilization of Ultrafine Metal Nanoparticles to High-Surface-Area Materials and Their Catalytic Applications. *Chem*, **2016**, *1*, 220-245.

181. Liu, J.; Chen, L.; Cui, H.; Zhang, J.; Zhang, L.; Su, C.-Y., Applications of Metal–Organic Frameworks in Heterogeneous Supramolecular Catalysis. *Chem. Soc. Rev.*, **2014**, *43*, 6011-6061.

182. Kaur, P.; Hupp, J. T.; Nguyen, S. T., Porous Organic Polymers in Catalysis: Opportunities and Challenges. *ACS Catal.*, **2011**, *1*, 819-835.

183. Chen, Y.; Chen, Z., COF-1-Modified Magnetic Nanoparticles for Highly Selective and Efficient Solid-Phase Microextraction of Paclitaxel. *Talanta*, **2017**, *165*, 188-193.

184. Pachfule, P.; Panda, M. K.; Kandambeth, S.; Shivaprasad, S.; DÍAz, D. D.; Banerjee, R., Multifunctional and Robust Covalent Organic Framework–Nanoparticle Hybrids. *J. Mater. Chem. A*, **2014**, *2*, 7944-7952.

185. Sun, J.-K.; Zhan, W.-W.; Akita, T.; Xu, Q., Toward Homogenization of Heterogeneous Metal Nanoparticle Catalysts With Enhanced Catalytic Performance: Soluble Porous Organic Cage As A Stabilizer and Homogenizer. *J. Am. Chem. Soc.*, **2015**, *137*, 7063-7066.

186. Sun, J.-K.; Kochovski, Z.; Zhang, W.-Y.; Kirmse, H.; Lu, Y.; Antonietti, M.; Yuan, J., General Synthetic Route Toward Highly Dispersed Metal Clusters Enabled By Poly (Ionic Liquid) S. *J. Am. Chem. Soc.*, **2017**, *139*, 8971-8976.

187. Yu, W.; Xie, H., A Review on Nanofluids: Preparation, Stability Mechanisms, and Applications. *Journal of Nanomaterials*, **2012**, *2012*.

188. Morsy, S. M., Role of Surfactants in Nanotechnology and Their Applications. *Int. J. Curr. Microbiol. App. Sci*, **2014**, *3*, 237-260.

189. Koczkur, K. M.; Mourdikoudis, S.; Polavarapu, L.; Skrabalak, S. E., Polyvinylpyrrolidone (PVP) in Nanoparticle Synthesis. *Dalton Trans.*, **2015**, *44*, 17883-17905.

190. CopÉRet, C.; Chabanas, M.; Petroff Saint - Arroman, R.; Basset, J. M., Homogeneous and Heterogeneous Catalysis: Bridging the Gap Through Surface Organometallic Chemistry. *Angew. Chem. Int. Ed.*, **2003**, *42*, 156-181.

191. Buchwalter, P.; Rosé, J.; Braunstein, P., Multimetallic Catalysis Based on Heterometallic Complexes and Clusters. *Chem. Rev.*, **2015**, *115*, 28-126.

192. Na, K.; Choi, K. M.; Yaghi, O. M.; Somorjai, G. A., Metal Nanocrystals Embedded in Single Nanocrystals of Mofs Give Unusual Selectivity As Heterogeneous Catalysts. *Nano Lett.*, **2014**, *14*, 5979-5983.

193. Hu, P.; Morabito, J. V.; Tsung, C.-K., Core–Shell Catalysts of Metal Nanoparticle Core and Metal–Organic Framework Shell. *ACS Catal.*, **2014**, *4*, 4409-4419.

194. Lu, G.; Li, S.; Guo, Z.; Farha, O. K.; Hauser, B. G.; Qi, X.; Wang, Y.; Wang, X.; Han, S.; Liu, X., Imparting Functionality to A Metal–Organic Framework Material By Controlled Nanoparticle Encapsulation. *Nat. Chem.*, **2012**, *4*, 310-316.

195. Guo, Z.; Xiao, C.; Maligal-Ganesh, R. V.; Zhou, L.; Goh, T. W.; Li, X.; Tesfagaber, D.; Thiel, A.; Huang, W., Pt Nanoclusters Confined Within Metal–Organic Framework Cavities for Chemoselective Cinnamaldehyde Hydrogenation. *ACS Catal.*, **2014**, *4*, 1340-1348.

196. Aijaz, A.; Karkamkar, A.; Choi, Y. J.; Tsumori, N.; RöNnebro, E.; Autrey, T.; Shioyama, H.; Xu, Q., Immobilizing Highly Catalytically Active Pt Nanoparticles Inside the Pores of Metal–Organic Framework: A Double Solvents Approach. *J. Am. Chem. Soc.*, **2012**, *134*, 13926-13929.

197. Wang, S.; Gao, X.; Hang, X.; Zhu, X.; Han, H.; Liao, W.; Chen, W., Ultrafine Pt Nanoclusters Confined in A Calixarene-Based {Ni24} Coordination Cage for High-Efficient Hydrogen Evolution Reaction. *J. Am. Chem. Soc.*, **2016**, *138*, 16236-16239.

198. Fujita, D.; Ueda, Y.; Sato, S.; Yokoyama, H.; Mizuno, N.; Kumasaka, T.; Fujita, M., Self-Assembly of M30L60 Icosidodecahedron. *Chem*, **2016**, *1*, 91-101.

199. Fang, Y.; Murase, T.; Sato, S.; Fujita, M., Noncovalent Tailoring of the Binding Pocket of Self-Assembled Cages By Remote Bulky Ancillary Groups. *J. Am. Chem. Soc.*, **2013**, *135*, 613-615.

200. Mugridge, J. S.; Szigethy, G. Z.; Bergman, R. G.; Raymond, K. N., Encapsulated Guest− Host Dynamics: Guest Rotational Barriers and Tumbling As A Probe of Host Interior Cavity Space. *J. Am. Chem. Soc.*, **2010**, *132*, 16256-16264.

201. Berseth, P. A.; Sokol, J. J.; Shores, M. P.; Heinrich, J. L.; Long, J. R., High-Nuclearity Metal-Cyanide Clusters: Assembly of A Cr8Ni6 (CN) 24 Cage With A Face-Centered Cubic Geometry. *J. Am. Chem. Soc.*, **2000**, *122*, 9655-9662.

202. Suzuki, K.; Takao, K.; Sato, S.; Fujita, M., the Precise Synthesis and Growth of Core ‐ Shell Nanoparticles Within A Self ‐ Assembled Spherical Template. *Angew. Chem. Int. Ed.*, **2011**, *50*, 4858-4861.

203. Ichijo, T.; Sato, S.; Fujita, M., Size-, Mass-, and Density-Controlled Preparation of Tio2 Nanoparticles in A Spherical Coordination Template. *J. Am. Chem. Soc.*, **2013**, *135*, 6786-6789.

204. Kumara, L.; Sakata, O.; Kohara, S.; Yang, A.; Song, C.; Kusada, K.; Kobayashi, H.; Kitagawa, H., Origin of the Catalytic Activity of Face-Centered-Cubic Ruthenium Nanoparticles Determined From An Atomic-Scale Structure. *PCCP*, **2016**, *18*, 30622-30629.

205. Li, W.-Z.; Liu, J.-X.; Gu, J.; Zhou, W.; Yao, S.-Y.; Si, R.; Guo, Y.; Su, H.-Y.; Yan, C.-H.; Li, W.-X., Chemical Insights Into the Design and Development of Face-Centered Cubic Ruthenium Catalysts for Fischer–Tropsch Synthesis. *J. Am. Chem. Soc.*, **2017**, *139*, 2267-2276.

206. Kusada, K.; Kobayashi, H.; Ikeda, R.; Kubota, Y.; Takata, M.; Toh, S.; Yamamoto, T.; Matsumura, S.; Sumi, N.; Sato, K., Solid Solution Alloy Nanoparticles of Immiscible Pd and Ru Elements Neighboring on Rh: Changeover of the Thermodynamic Behavior for Hydrogen Storage and Enhanced CO-Oxidizing Ability. *J. Am. Chem. Soc.*, **2014**, *136*, 1864-1871.

207. Bedford, N.; Dablemont, C.; Viau, G.; Chupas, P.; Petkov, V., 3-D Structure of Nanosized Catalysts By High-Energy X-Ray Diffraction and Reverse Monte Carlo Simulations: Study of Ru. *J. Phys. Chem. C*, **2007**, *111*, 18214-18219.

208. Joo, S. H.; Park, J. Y.; Renzas, J. R.; Butcher, D. R.; Huang, W.; Somorjai, G. A., Size Effect of Ruthenium Nanoparticles in Catalytic Carbon Monoxide Oxidation. *Nano Lett.*, **2010**, *10*, 2709-2713.

209. Kobayashi, M.; Kai, T.; Takano, N.; Shiiki, K., the Possibility of Ferromagnetic BCC Ruthenium. *J. Phys.: Condens. Matter*, **1995**, *7*, 1835.

210. Watanabe, S.; Komine, T.; Kai, T.; Shiiki, K., First-Principle Band Calculation of Ruthenium for Various Phases. *J. Magn. Magn. Mater.*, **2000**, *220*, 277-284.

211. Kusada, K.; Kobayashi, H.; Yamamoto, T.; Matsumura, S.; Sumi, N.; Sato, K.; Nagaoka, K.; Kubota, Y.; Kitagawa, H., Discovery of Face-Centered-Cubic Ruthenium

Nanoparticles: Facile Size-Controlled Synthesis Using the Chemical Reduction Method. *J. Am. Chem. Soc.*, **2013**, *135*, 5493-5496.

212. Abo‐Hamed, E. K.; Pennycook, T.; Vaynzof, Y.; Toprakcioglu, C.; Koutsioubas, A.; Scherman, O. A., Highly Active Metastable Ruthenium Nanoparticles for Hydrogen Production Through the Catalytic Hydrolysis of Ammonia Borane. *Small*, **2014**, *10*, 3145-3152.

213. Sun, Q.-F.; Iwasa, J.; Ogawa, D.; Ishido, Y.; Sato, S.; Ozeki, T.; Sei, Y.; Yamaguchi, K.; Fujita, M., Self-Assembled M24L48 Polyhedra and Their Sharp Structural Switch Upon Subtle Ligand Variation. *Sci.*, **2010**, *328*, 1144-1147.

214. Seidel, S. R.; Stang, P. J., High-Symmetry Coordination Cages Via Self-Assembly. *Acc. Chem. Res.*, **2002**, *35*, 972-983.

215. Bilbeisi, R. A.; Clegg, J. K.; Elgrishi, N.; Hatten, X. D.; Devillard, M.; Breiner, B.; Mal, P.; Nitschke, J. R., Subcomponent Self-Assembly and Guest-Binding Properties of Face-Capped Fe4L48+ Capsules. *J. Am. Chem. Soc.*, **2012**, *134*, 5110-5119.

216. Fujita, D.; Ueda, Y.; Sato, S.; Mizuno, N.; Kumasaka, T.; Fujita, M., Self-Assembly of Tetravalent Goldberg Polyhedra From 144 Small Components. *Nature*, **2016**, *540*, 563-566.

217. Li, J.-R.; Zhou, H.-C., Bridging-Ligand-Substitution Strategy for the Preparation of Metal–Organic Polyhedra. *Nat. Chem.*, **2010**, *2*, 893.

218. Liu, M.; Liao, W.; Hu, C.; Du, S.; Zhang, H., Calixarene‐Based Nanoscale Coordination Cages. *Angew. Chem. Int. Ed.*, **2012**, *51*, 1585-1588.

219. Heine, J.; Schmedt Auf Der GüNne, J. R.; Dehnen, S., Formation of A Strandlike Polycatenane of Icosahedral Cages for Reversible One-Dimensional Encapsulation of Guests. *J. Am. Chem. Soc.*, **2011**, *133*, 10018-10021.

220. Pasquale, S.; Sattin, S.; Escudero-AdÁN, E. C.; MartÍNez-Belmonte, M.; De Mendoza, J., Giant Regular Polyhedra From Calixarene Carboxylates and Uranyl. *Nat. Commun.*, **2012**, *3*, 1-7.

221. MÉVellec, V.; Leger, B.; Mauduit, M.; Roucoux, A., Organic Phase Stabilization of Rhodium Nanoparticle Catalyst By Direct Phase Transfer From Aqueous Solution to Room Temperature Ionic Liquid Based on Surfactant Counter Anion Exchange. *Chem. Commun.*, **2005**, 2838-2839.

222. Yan, X.; Liu, H.; Liew, K. Y., Size Control of Polymer-Stabilized Ruthenium Nanoparticles By Polyol Reduction. *J. Mater. Chem.*, **2001**, *11*, 3387-3391.

223. Over, H.; Kim, Y. D.; Seitsonen, A.; Wendt, S.; Lundgren, E.; Schmid, M.; Varga, P.; Morgante, A.; Ertl, G., Atomic-Scale Structure and Catalytic Reactivity of the Ruo2 (110) Surface. *Sci.*, **2000**, *287*, 1474-1476.

224. Rupprechter, G., Surface Vibrational Spectroscopy From Ultrahigh Vacuum to Atmospheric Pressure: Adsorption and Reactions on Single Crystals and Nanoparticle Model Catalysts Monitored By Sum Frequency Generation Spectroscopy. *PCCP*, **2001**, *3*, 4621-4632.

225. Lim, B.; Jiang, M.; Tao, J.; Camargo, P. H.; Zhu, Y.; Xia, Y., Shape‐Controlled Synthesis of Pd Nanocrystals in Aqueous Solutions. *Adv. Funct. Mater.*, **2009**, *19*, 189-200.

226. Ye, X.-R.; Lin, Y.; Wang, C.; Engelhard, M. H.; Wang, Y.; Wai, C. M., Supercritical Fluid Synthesis and Characterization of Catalytic Metal Nanoparticles on Carbon Nanotubes. *J. Mater. Chem.*, **2004**, *14*, 908-913.

227. Metin, O.; Mazumder, V.; Ozkar, S.; Sun, S., Monodisperse Nickel Nanoparticles and Their Catalysis in Hydrolytic Dehydrogenation of Ammonia Borane. *J. Am. Chem. Soc.*, **2010**, *132*, 1468-1469.

228. Zhan, W.-W.; Zhu, Q.-L.; Xu, Q., Dehydrogenation of Ammonia Borane By Metal Nanoparticle Catalysts. *ACS Catal.*, **2016**, *6*, 6892-6905.

229. Kumar, R.; Lee, Y. O.; Bhalla, V.; Kumar, M.; Kim, J. S., Recent Developments of Thiacalixarene Based Molecular Motifs. *Chem. Soc. Rev.*, **2014**, *43*, 4824-4870.